MICROCOPY RESOLUTION TEST CHART
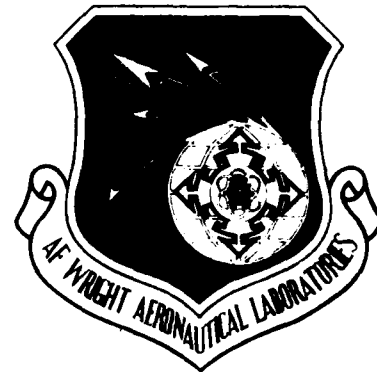NATIONAL BUREAU OF STANDARDS-1963-A

AD-A151 502

AFWAL-TR-84-2074

ELECTRIC DISCHARGE EXCITATION AND
ENERGY SOURCE INTEGRATION

D. F. GROSJEAN

Research Applications Division
Systems Research Laboratories, Inc.
2800 Indian Ripple Road
Dayton, OH 45440-3696

January 1985

Final Report for Period 30 January 1980 - 31 December 1983

Approved for public release; distribution unlimited.

AERO PROPULSION LABORATORY
AIR FORCE WRIGHT AERONAUTICAL LABORATORIES
AIR FORCE SYSTEMS COMMAND
WRIGHT-PATTERSON AIR FORCE BASE, OH 45433

85   03   05   016

PETER BLETZINGER
Plasma Physics
Energy Conversion Branch
Aerospace Power Division

ROBERT L. KERR
Chief, Energy Conversion Branch
Aerospace Power Division
Aero Propulsion Laboratory

FOR THE COMMANDER

JAMES D. REAMS
Chief, Aerospace Power Division
Aero Propulsion Laboratory

REPORT DOCUMENTATION PAGE

1a. REPORT SECURITY CLASSIFICATION		1b. RESTRICTIVE MARKINGS	
Unclassified			

2a. SECURITY CLASSIFICATION AUTHORITY	3. DISTRIBUTION/AVAILABILITY OF REPORT
	Approved for public release; distribution unlimited.
2b. DECLASSIFICATION/DOWNGRADING SCHEDULE	

4. PERFORMING ORGANIZATION REPORT NUMBER(S)	5. MONITORING ORGANIZATION REPORT NUMBER(S)
6569 Final	AFWAL-TR-84-2074

6a. NAME OF PERFORMING ORGANIZATION	6b. OFFICE SYMBOL (If applicable)	7a. NAME OF MONITORING ORGANIZATION
Systems Research Laboratories, Inc., Research Applications Division		Aero Propulsion Laboratory (AFWAL/POOC) Air Force Wright Aeronautical Laboratories (AFSC)

6c. ADDRESS (City, State and ZIP Code)	7b. ADDRESS (City, State and ZIP Code)
2800 Indian Ripple Road Dayton, OH 45440-3696	Wright-Patterson Air Force Base, OH 45433

8a. NAME OF FUNDING/SPONSORING ORGANIZATION	8b. OFFICE SYMBOL (If applicable)	9. PROCUREMENT INSTRUMENT IDENTIFICATION NUMBER
		F33615-79-C-2084

8c. ADDRESS (City, State and ZIP Code)	10. SOURCE OF FUNDING NOS.			
	PROGRAM ELEMENT NO.	PROJECT NO.	TASK NO.	WORK UNIT NO.
	61102F	2301	S2	22

11. TITLE (Include Security Classification) Electric Discharge Excitation and Energy Source Integration

12. PERSONAL AUTHOR(S) Grosjean, D. F.

13a. TYPE OF REPORT	13b. TIME COVERED	14. DATE OF REPORT (Yr., Mo., Day)	15. PAGE COUNT
Final Report	FROM 80-1-30 TO 83-12-31	1985 January 6	170

16. SUPPLEMENTARY NOTATION

approx < Cont

17	COSATI CODES		18. SUBJECT TERMS (Continue on reverse if necessary and identify by block number)
FIELD	GROUP	SUB. GR.	Pulse Power Conditioning, Pulse-Forming Networks, Computer Modeling, Electronegative Gas Discharge, Rare-Gas-Halide Lasers, Dye Lasers, High-Repetition-Rate Lasers .
20	09		

19. ABSTRACT (Continue on reverse if necessary and identify by block number)

Methods of transferring energy from electrical storage to an electro-negative gas discharge at high repetition rates of $\leq$ 1.5 kHz are examined. The electrical-energy range of interest is 1 - 10 J. The XeCl gas-discharge laser system is used as a representative discharge. Computer modeling of the pertinent kinetics of a He/Xe/HCl gas mixture which was performed in conjunction with various configurations of pulse-forming networks is described; gas thyratrons and magnetic switches were used as switching elements. Due to the relatively constant E/N characteristics of this system, a stripline arrangement is shown to provide the most efficient method of energy transfer for pulse lengths $\geq$ 50 nsec. Capacitor discharge methods are applicable to shorter pulse lengths. Construction of a closed-cycle, high-rep-rate XeCl gas-discharge laser is described. When UV preionization is utilized, a rapid buildup of impurities is observed. Operation of an x-ray preionized system at 1.5 kHz is also detailed; no contamination was observed in this configuration. The application of the XeCl laser as a pump source for a high-rep-rate, high-average-power dye laser is also described. A flowing-dye jet was utilized in order to avoid liquid-cell boundary-layer— cont

20. DISTRIBUTION/AVAILABILITY OF ABSTRACT	21. ABSTRACT SECURITY CLASSIFICATION
UNCLASSIFIED/UNLIMITED ☒ SAME AS RPT. ☐ DTIC USERS ☐	Unclassified

22a. NAME OF RESPONSIBLE INDIVIDUAL	22b. TELEPHONE NUMBER (Include Area Code)	22c. OFFICE SYMBOL
Peter Bletzinger, Ph.D.	(513) 255-2923	AFWAL/POOC-3

DD FORM 1473, 83 APR   EDITION OF 1 JAN 73 IS OBSOLETE.

19. Continued.

problems of a fast-flow stream. The optical quality of the jet stream was the limiting factor in achieving the power goals. A method of achieving high efficiency in a rare-gas-halide system is proposed via a magnetic switch and prepulse arrangement in conjunction with a stripline PFN. A high-efficiency pulse-charging source is also described.

> cont keywords include: > 1472

PREFACE

A-1

iii

TABLE OF CONTENTS

LIST OF ILLUSTRATIONS

LIST OF ILLUSTRATIONS (Continued)

LIST OF ILLUSTRATIONS (Continued)

LIST OF ILLUSTRATIONS (Continued)

LIST OF ILLUSTRATIONS (Continued)

LIST OF ILLUSTRATIONS (Concluded)

LIST OF TABLES

Section I

INTRODUCTION

The promise of scaling UV/visible laser output to high pulse energy and average power at efficiencies greater than 1% has led to a high level of current interest and activity in the excimer laser area. Progress in the development of excimer lasers has proceeded rapidly since the first laboratory demonstration in 1972.[1] In addition to the rare-gas dimers, lasing has been achieved in rare-gas oxides, rare-gas halides, halogen dimers, and metal halides. The rapid development of rare-gas-halide lasers is due, in part, to the numerous optical, photoelectric, and photochemical applications of the short-pulse, short-wavelength sources.

Population inversion in excimers can be readily produced since the lower laser level dissociates in a time much less than the upper level lifetime. The resulting broad bandwidth, however, implies a low stimulated-emission cross section--and, therefore, gain--which means that intensive pumping is required for laser action to be achieved. Initially, high-power e-beams were used to pump excimer lasers. Within the last five years, however, discharge-excited excimer lasers having higher efficiency and higher-repetition-rate capability have been developed. The high excitation power densities, high pressure, and electronegative gas mixtures required for these lasers lead to severe discharge stability problems.

The highly nonlinear, time-varying impedance characteristic of most pulsed gas discharges places severe demands upon the operational characteristics of the power supply/power conditioning used to drive the discharge, resulting in requirements for extremely fast pulse risetime, low source impedance, time-varying source characteristics, and high-average-power capability at high repetition rates. The uniform excitation of gas mixtures containing electronegative gases is made even more difficult by the formation of negative ions which promote the growth of discharge instabilities.

Of all the rare-gas halide lasers, the discharge-pumped XeCl laser has shown the most promise for efficient, high-repetition-rate, long-life operation at

relatively high output energy. This report describes the results of theoretical and experimental investigations of the electrical characteristics of the discharge-excited XeCl laser relevant to the design of optimum power-conditioning systems. Both UV- and x-ray preionized lasers were studied.

A theoretical model of a discharge, power-supply, and power-conditioning system based upon existing models of pulsed-electronegative-gas discharges is described in Section II. Experimental studies of UV- and x-ray preionized, discharge-excited, closed-cycle XeCl lasers are discussed in Section III. The application of the XeCl laser to dye-laser pumping is treated in Section IV. Section V discusses the application of magnetic switching techniques to the XeCl laser. A high-efficiency pulsed-charging source is described in Section VI.

Section II

COMPUTER MODELING

The objective of the modeling effort was to predict the electrical-discharge characteristics of electronegative gas mixtures. The gas kinetics, therefore, were simplified to include only the reactions affecting charged-particle behavior. Assuming a uniform electron and electric-field distribution and no restrictions on cathode emission, discharge current (I) is determined by the discharge area (A) at the electrodes, the electron number density (n), and the electron drift velocity (v). That is,

$$I = neAv \qquad (1)$$

where e is the electronic charge. Electron number density can be determined by considering ionization, attachment, and recombination reactions. Since ionization and attachment of some excited-state species as well as electron-ion recombination of rare-gas dimer ions are expected to occur, selected excitation and ion-neutral reactions must also be included in the model.

The drift velocity and reaction rates are dependent upon the electron-energy distribution function (EEDF) which is, in turn, dependent upon the electric-field strength (E), neutral number density (N), and electron-collision cross sections (σ_i). The proper modeling procedure is first to calculate the EEDF from the Boltzmann equation using inputs of σ_i, E/N, n, and number density of each pertinent species. The resulting ionization, attachment, and recombination-rates--inferred from calculated electron temperature (T_e)--can then be used to calculate the electron density. Using this density and the calculated drift velocity, the instantaneous current can be calculated and used in conjunction with the power-conditioning-circuit parameters to predict the discharge-circuit characteristics.

As the densities of excited-state species increase, their collision cross sections may influence the EEDF. Therefore, the Boltzmann equation should be solved frequently if the model is to predict the time behavior of the

circuit accurately. However, the discharge kinetics involve the simultaneous solution of numerous coupled, stiff differential equations--very time consuming on the computer. The addition of frequent Boltzmann calculations would make the computation time prohibitive. Fortunately, for the types of discharges considered here, the error introduced by a single Boltzmann solution applied for the duration of the discharge is minimal. This will be discussed later.

The procedure followed here, then, is to calculate and tabulate reaction rates as a function of E/N for conditions representative of the discharge gas mix and incorporate these data along with the pertinent nonlinear reaction-rate equations and power-conditioning-circuit parameters into SCEPTRE, a circuit-modeling computer code. It then becomes relatively easy to demonstrate the effects of changes in kinetic rates, circuit parameters, and circuit configurations. Since the discharge characteristics are dependent upon the field applied by the power-conditioning circuit and since the applied field is dependent upon the impedance and rate of change of current of the discharge, the overall circuit characteristics are very sensitive to circuit parameters.

As an example of an electronegative gas discharge, a typical He-buffered XeCl laser mix of He/Xe/HCl in a ratio of 94.8/5/0.2 was chosen. The XeCl discharge is of great interest due to its potential for long-life, closed-cycle, high-repetition-rate operation. The remainder of this discussion will be concentrated on the XeCl laser mixture.

DISCHARGE KINETICS

Figures 1-4 show the collision cross sections used in the calculation of the EEDF. The effects of various cross sections upon the discharge characteristics will be discussed later, but several points should be brought out here.

Although He is present in large quantities, the cross section for formation of the 2^3S metastable (Fig. 1) is relatively small and has a threshold of $\sim$ 19.8 eV. Excitation to this level is limited to periods of high E/N only. Since Penning ionization of Xe by this level is very fast, this channel of
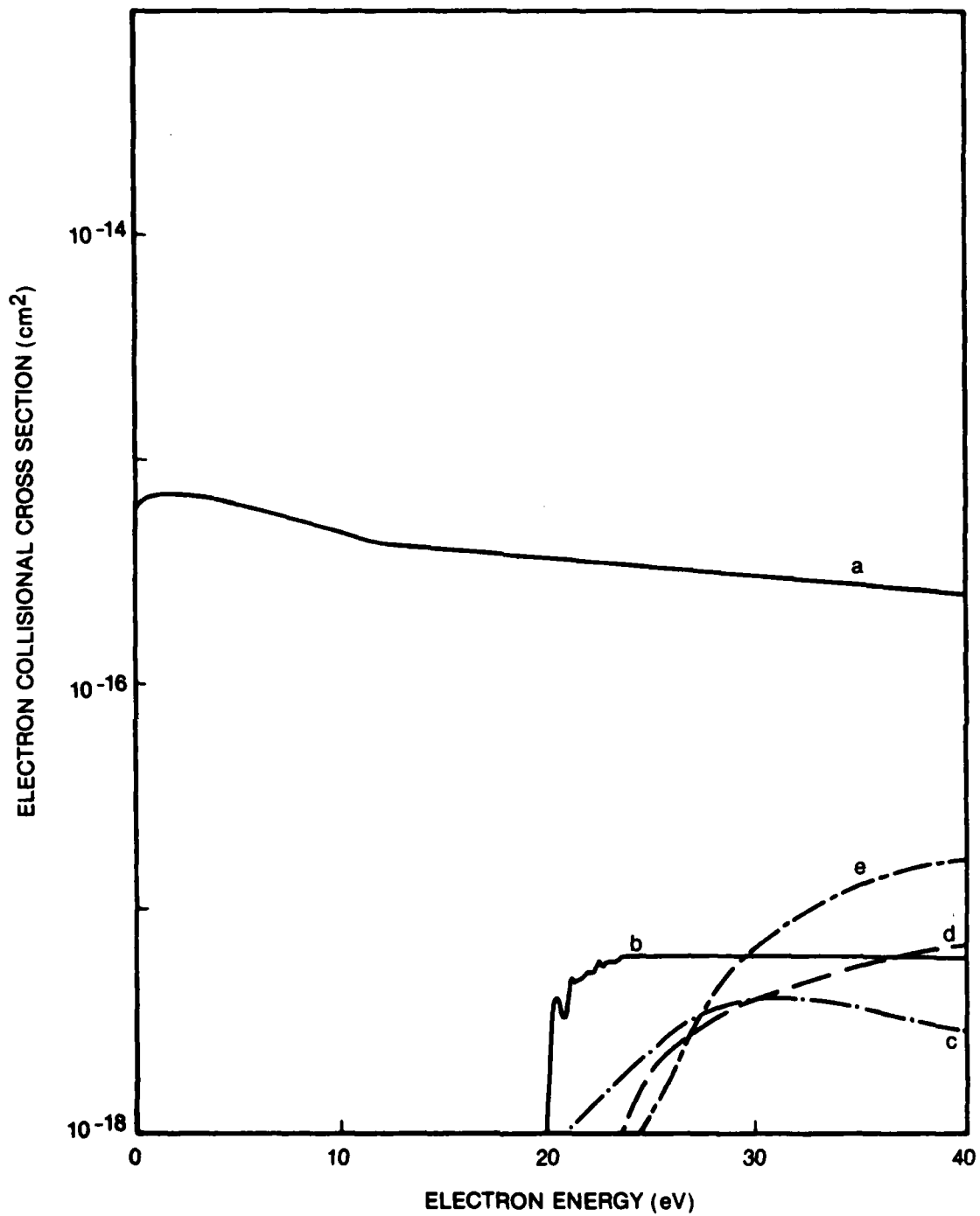
Figure 1. He Electron Collision Cross Sections. (a) Momentum Transfer,[2] (b) He 2^3S Formation,[3] (c) He 2^3p Formation,[4] (d) He s^{1}p Formation,[5] and (e) He Ionization.[6]

5
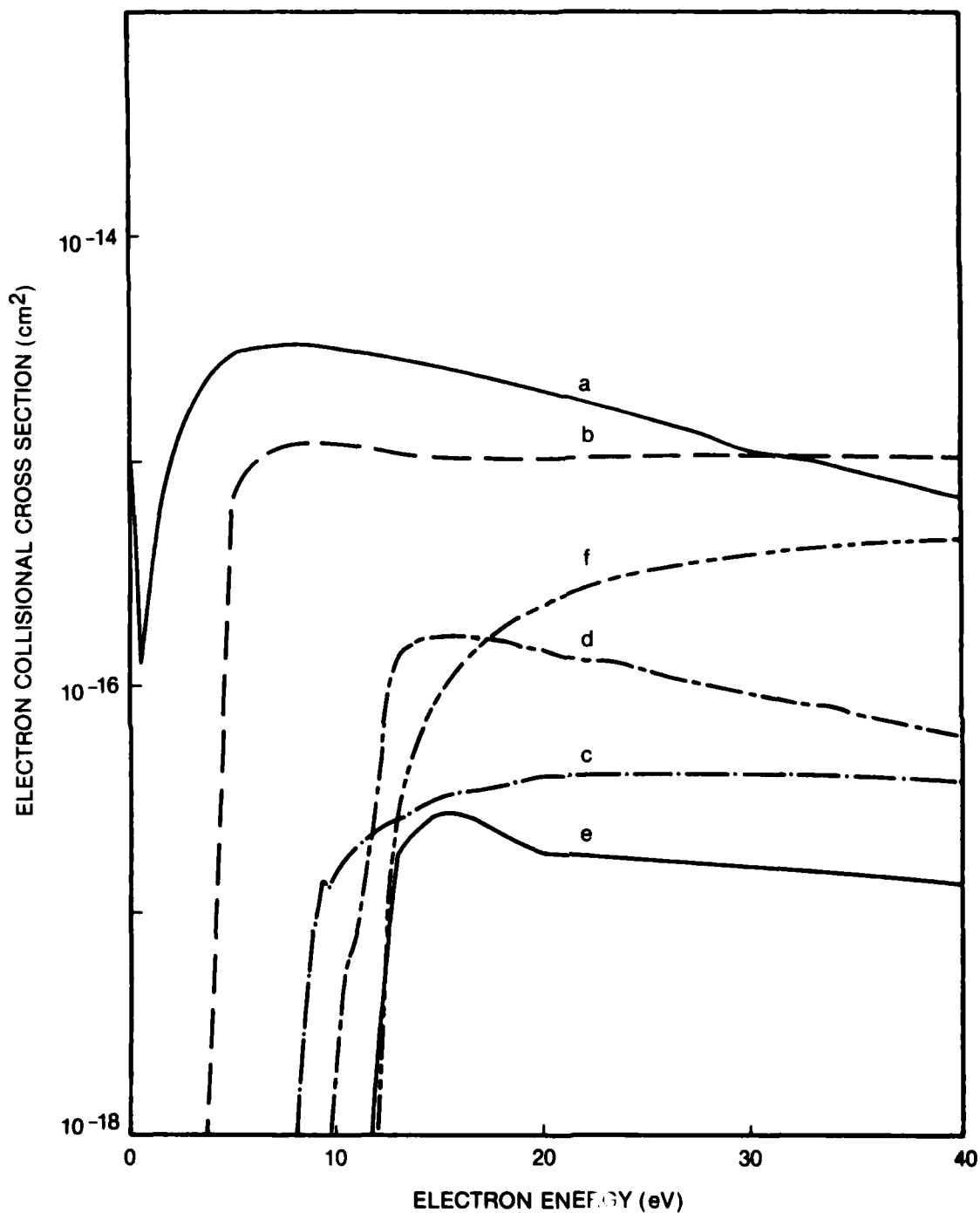
Figure 2. Xe Electron Collision Cross Sections. (a) Momentum Transfer,[7]
(b) Ionization of the 6s Metastable Level,[8] (c) Xe 6s Forma-
tion,[9] (d) Xe 6s', 6p, and 5d Formation,[9] (e) Total Excitation
Cross Section Less b, c, and d,[9] and (f) Ionization Out of the
5p Ground State.[6]

6
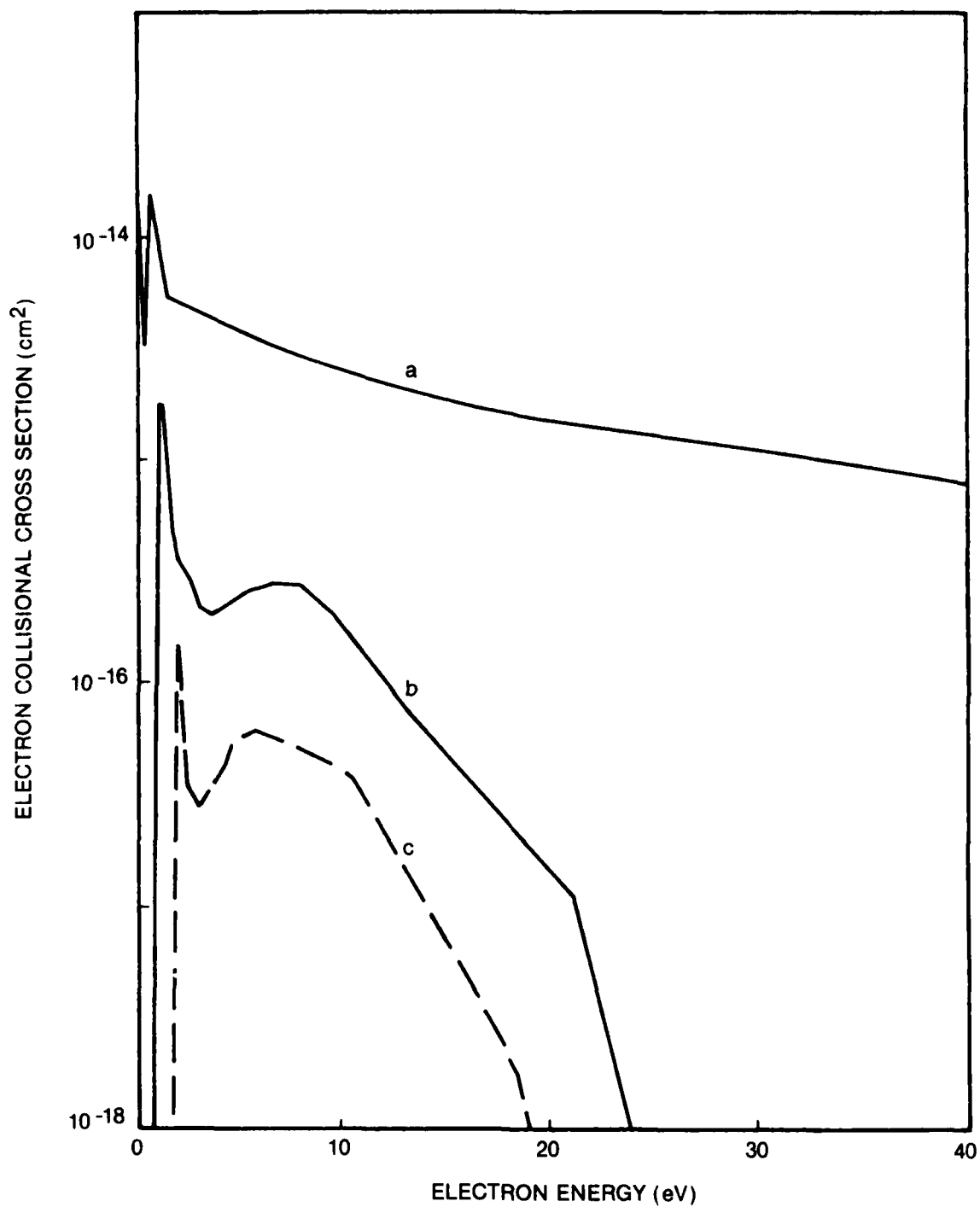
Figure 3. HCl Electron-Collision Cross Sections. (a) Momentum Transfer,[10]
(b) HCl $(v = 0) \rightarrow$ HCl $(v = 1)$,[11] and (c) HCl $(v = 0) \rightarrow$ HCl
$(v = 2)$.[11]

7
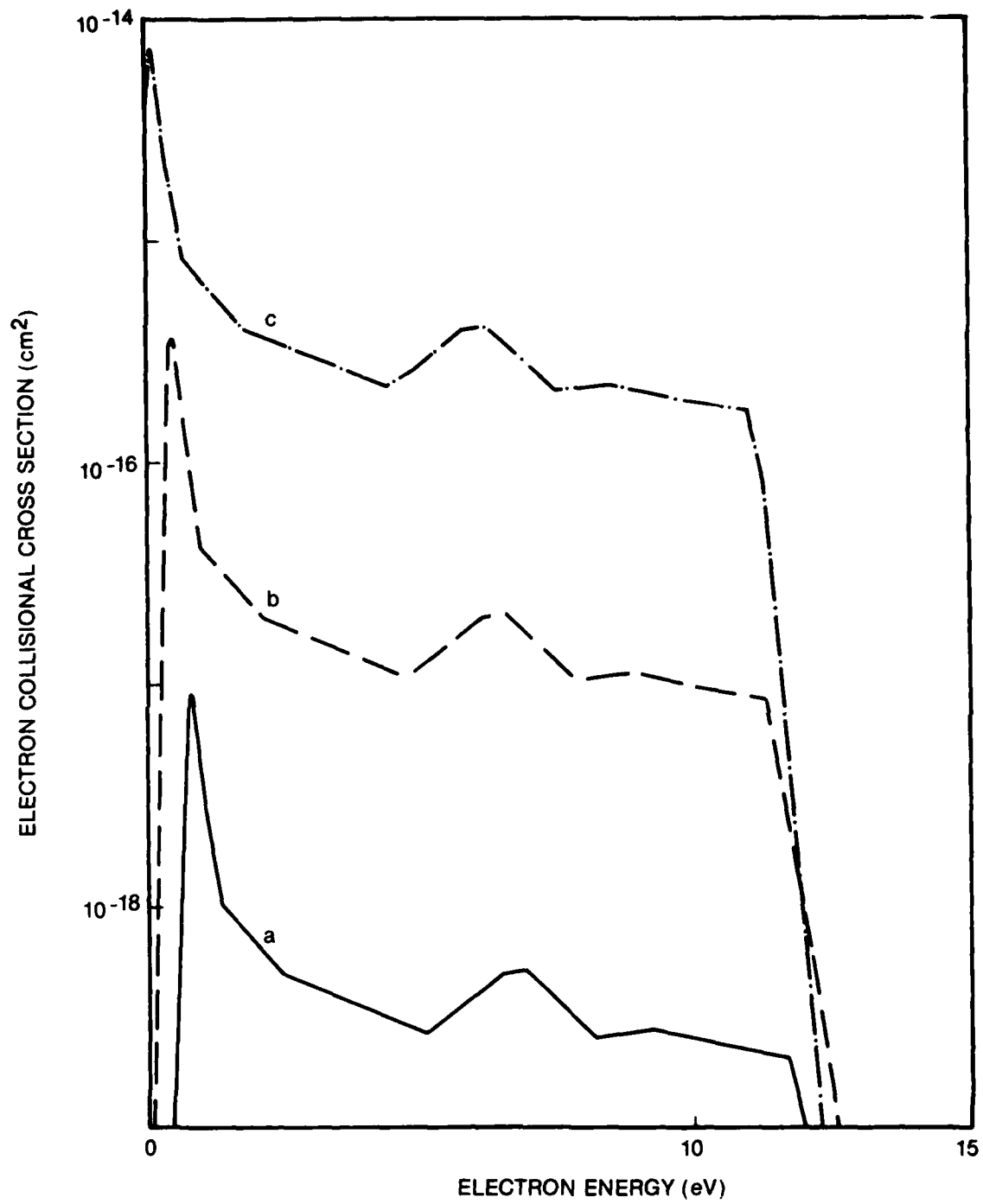
Figure 4. HCl Electron Dissociative-Attachment Cross Sections.
(a) $v = 0$,[12] (b) $v = 1$, [13] and (c) $v = 2$.[14]

ionization will generally be limited to the initial overvoltage period of a discharge pulse.

The cross section for ionization of the Xe (6s) metastable is quite large at low electron energies. This reaction threshold is 3.8 eV, while the threshold for formation of the metastable is 8.0 eV. This means that for moderate values of E/N where a significant number of electrons with energy > 8 eV is present, two-step ionization will occur. Since 6s formation may also occur through cascade from higher-lying states, it is likely that the majority of ionization after the initial overvoltage breakdown will be through the Xe-metastable ionization channel.

The cross-section data for vibrational excitation and dissociative attachment have been plotted on expanded scales (Figs. 3, 4) in order to emphasize the effects at low electron energies. Measured attachment cross sections[13] exist only for HCl (v = 0) and are relatively small. However, the estimated increase in cross sections with vibrational level will result in very high attachment rates if any significant amount of excited HCl is present. Since the excitation cross sections are, themselves, quite high, one would expect a significant amount of two-step attachment, especially at low E/N. It should be pointed out that the sharp drop-offs shown in Fig. 4 are a result of estimating data from a difficult-to-read plot in the literature. It is expected that the fall should be more gradual, beginning at $\sim$ 6 - 10 eV; however, the error introduced by the plotted data is not expected to be significant for the conditions under consideration here.

Figures 5-10 show the result of Boltzmann-code[15] calculations for inputs of ground-state-species populations determined from the initial mixture (94.8/5/0.2 of He/Xe/HCl), excited-state populations = 0, $n = 10^{12}$ cm^{-3}, gas temperature = 300 K, and collision cross sections according to those of Figs. 1-4. The reaction rates of Figs. 5-8 and the electron temperatures of Fig. 9 are used to determine production (ionization) and loss (attachment and recombination) of electron density. Current is then calculated using the electron drift velocity of Fig. 10.

9
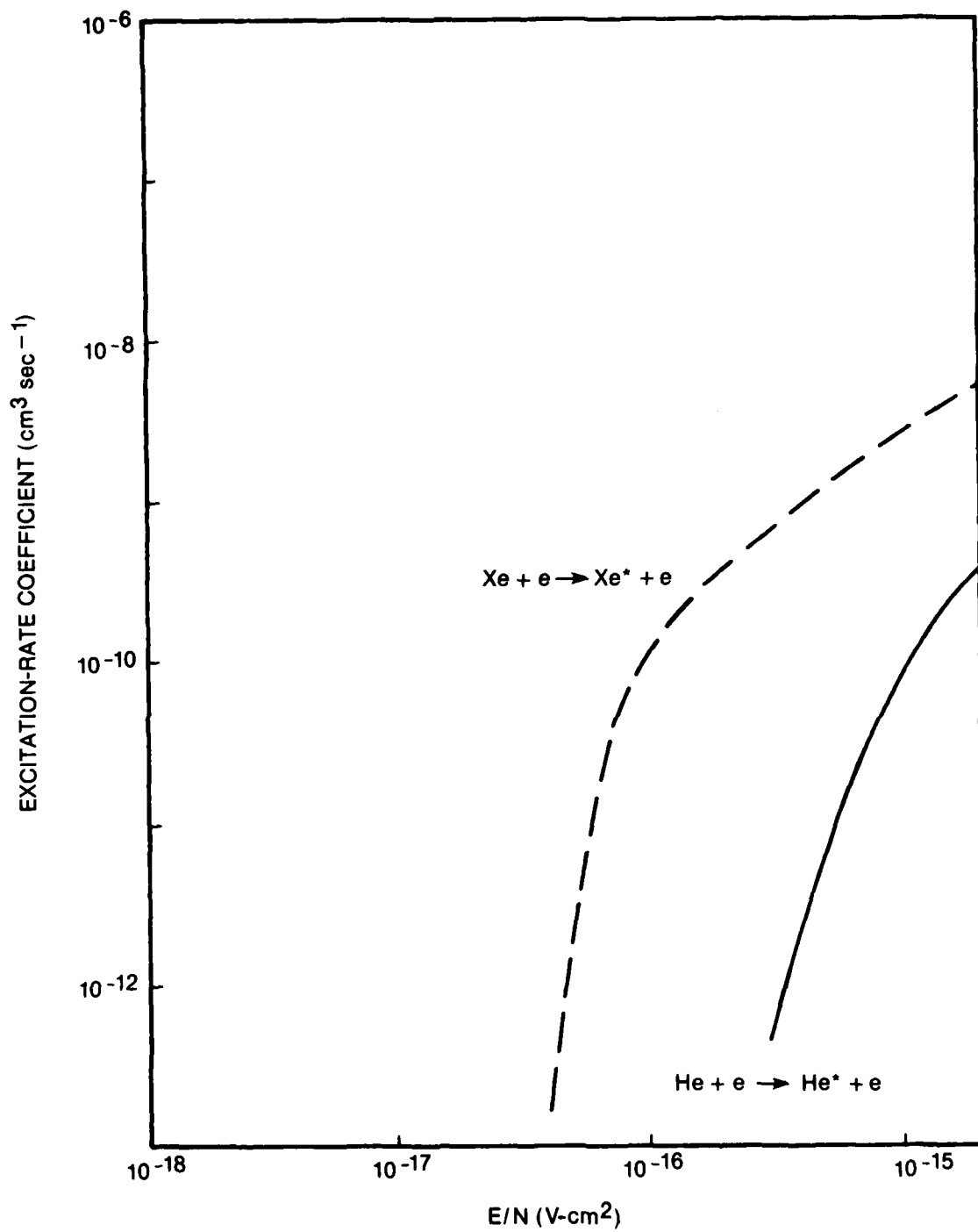
Figure 5. Metastable-Excitation Rates for He/Xe/HCl Mix of 94.8/5/0.2.
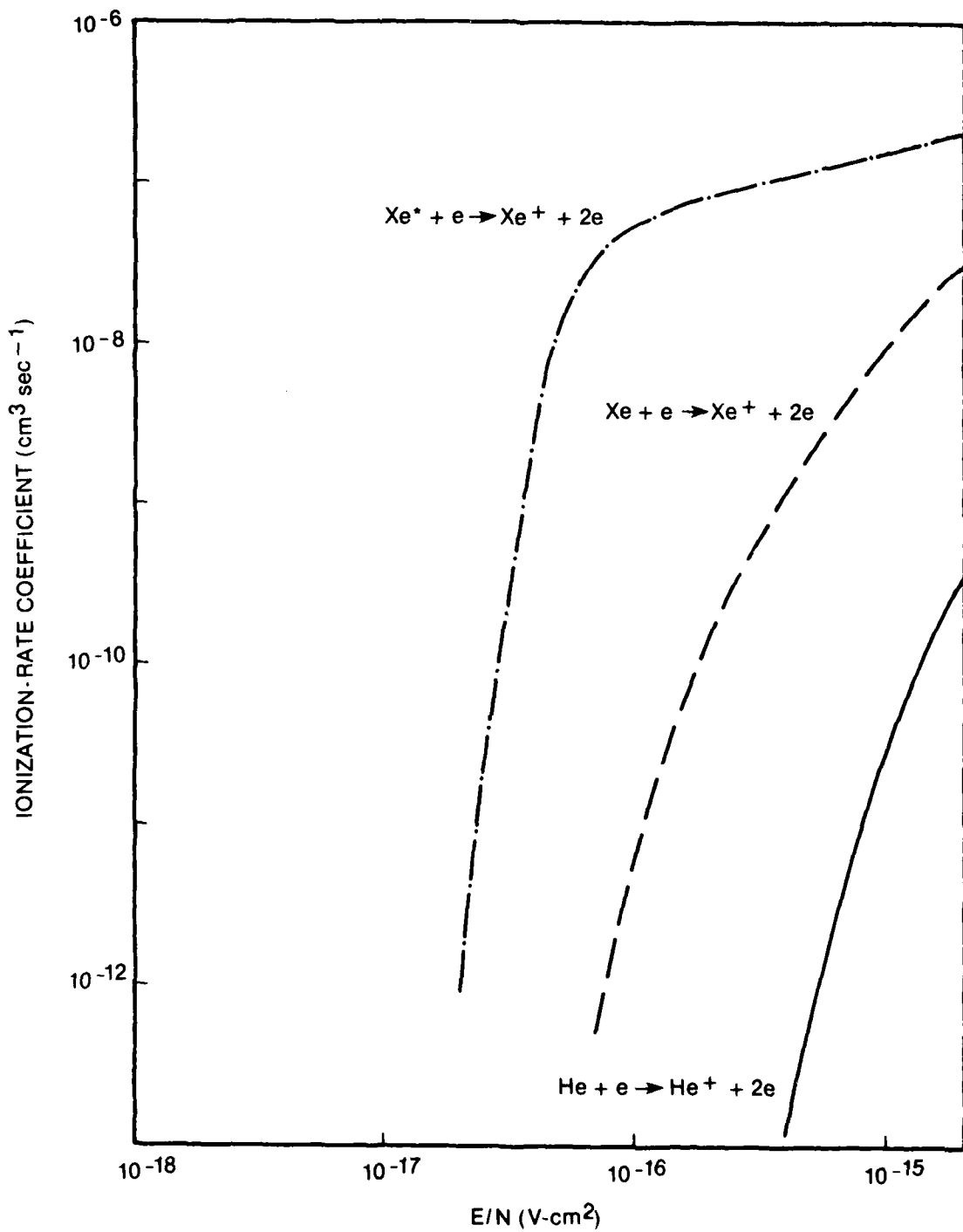
Figure 6.   Ionization Rates for He/Xe/HCl Mix of 94.8/5/0.2.

11
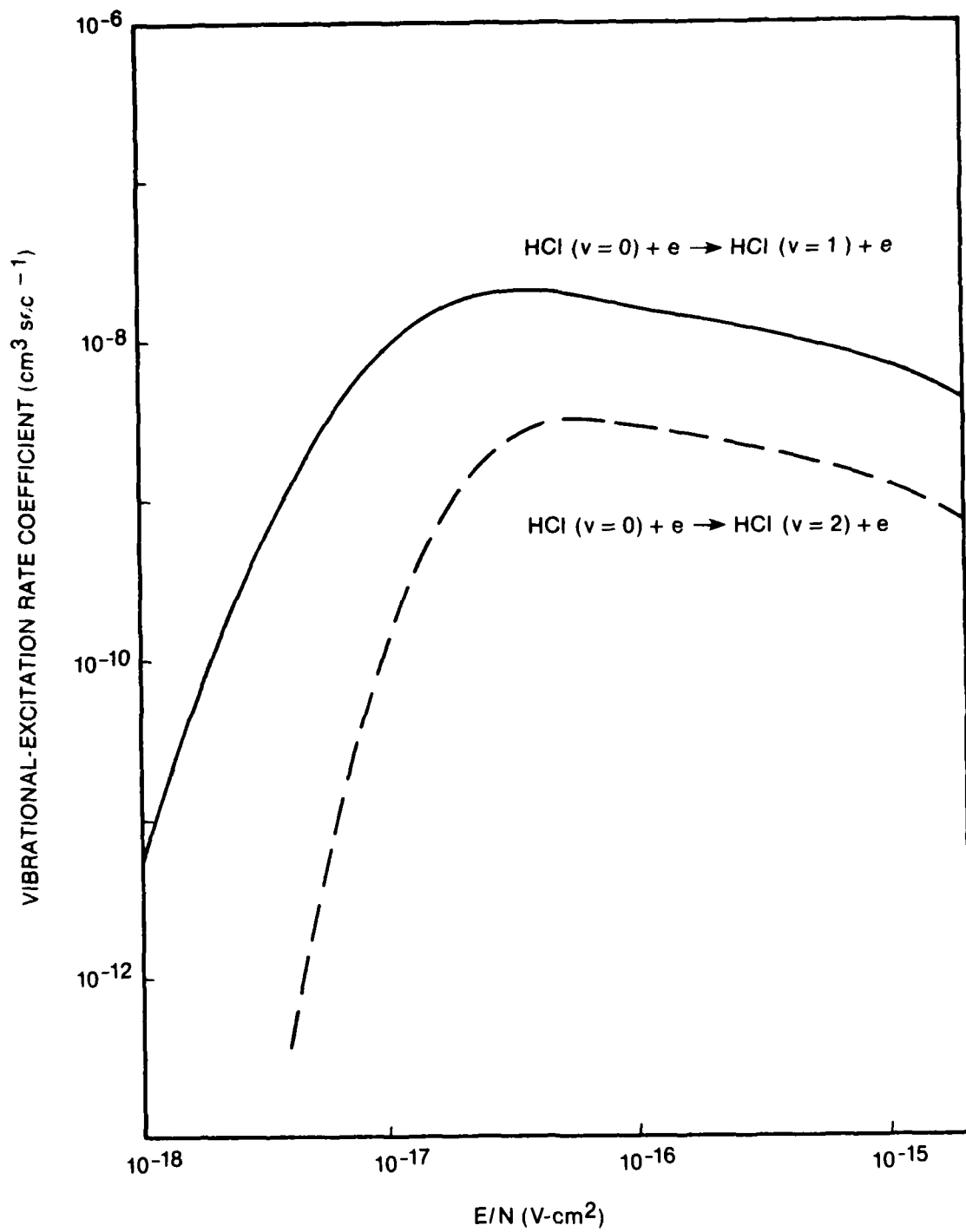
Figure 7. HCl Vibrational-Excitation Rates for He/Xe/HCl Mix of 94.8/5/0.2.
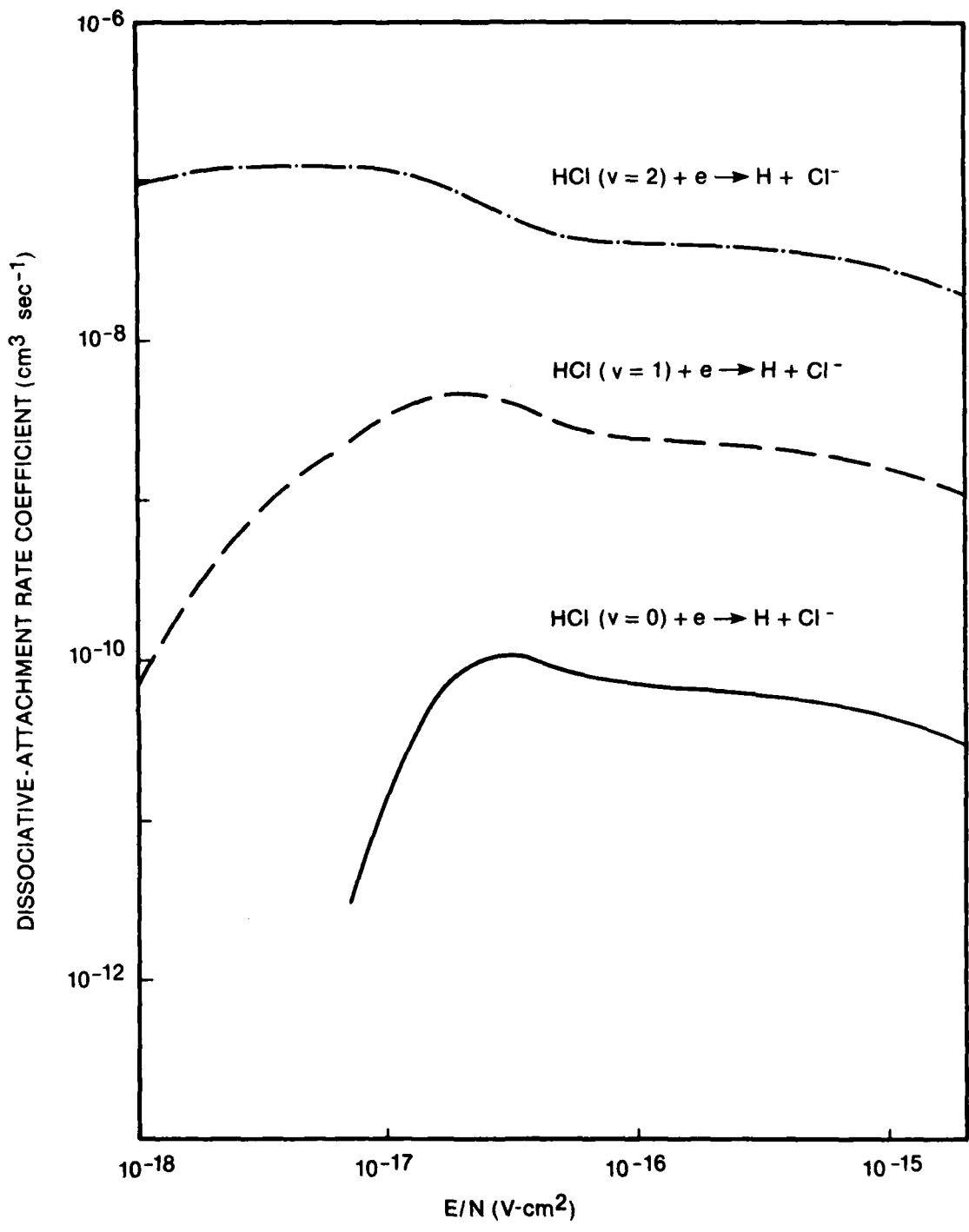
Figure 8.   HCl Dissociative-Attachment Rates for He/Xe/HCl Mix of
            94.8/5/0.2.
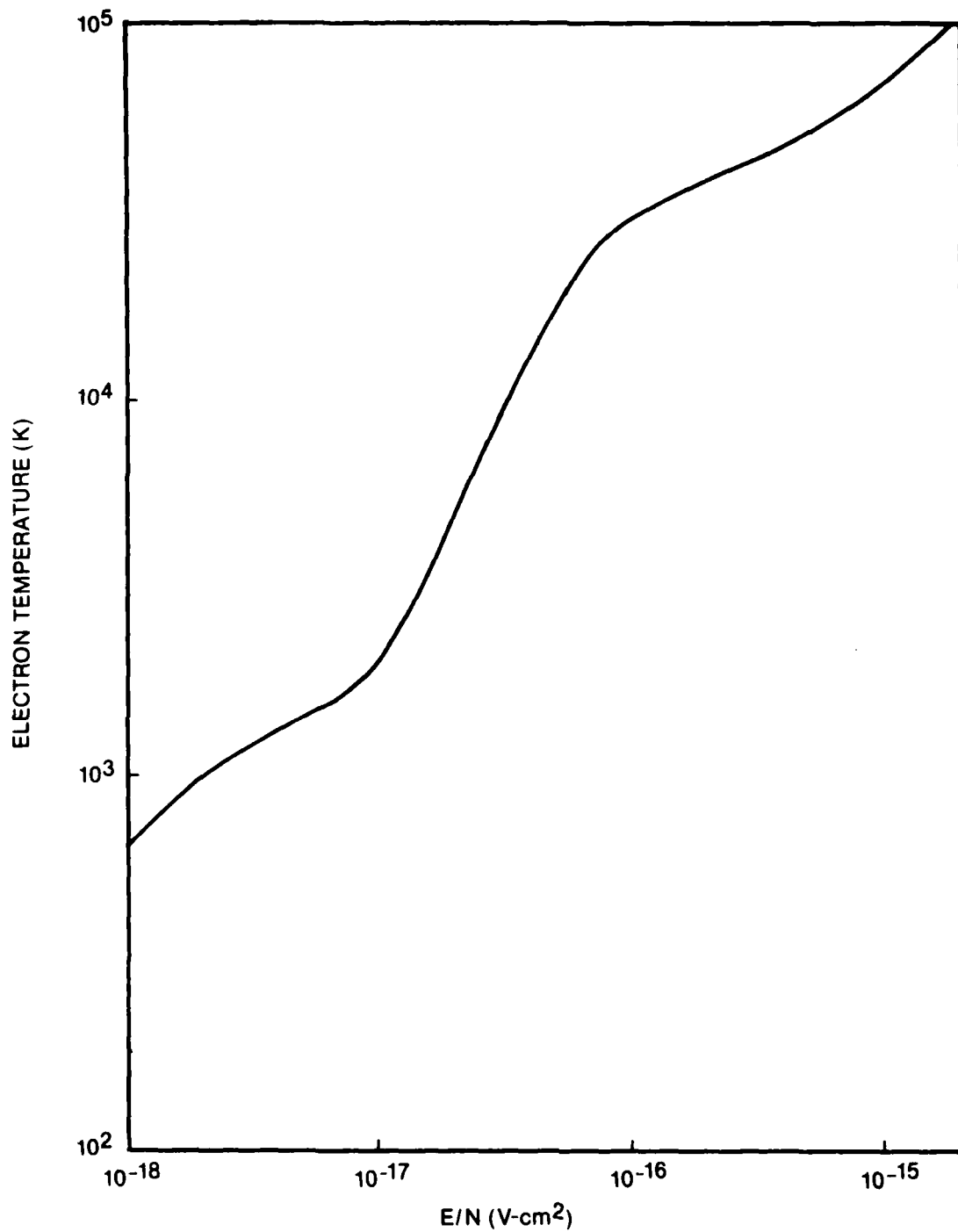
Figure 9. Electron Temperatures for He/Xe/HCl Mix of 94.8/5/02.
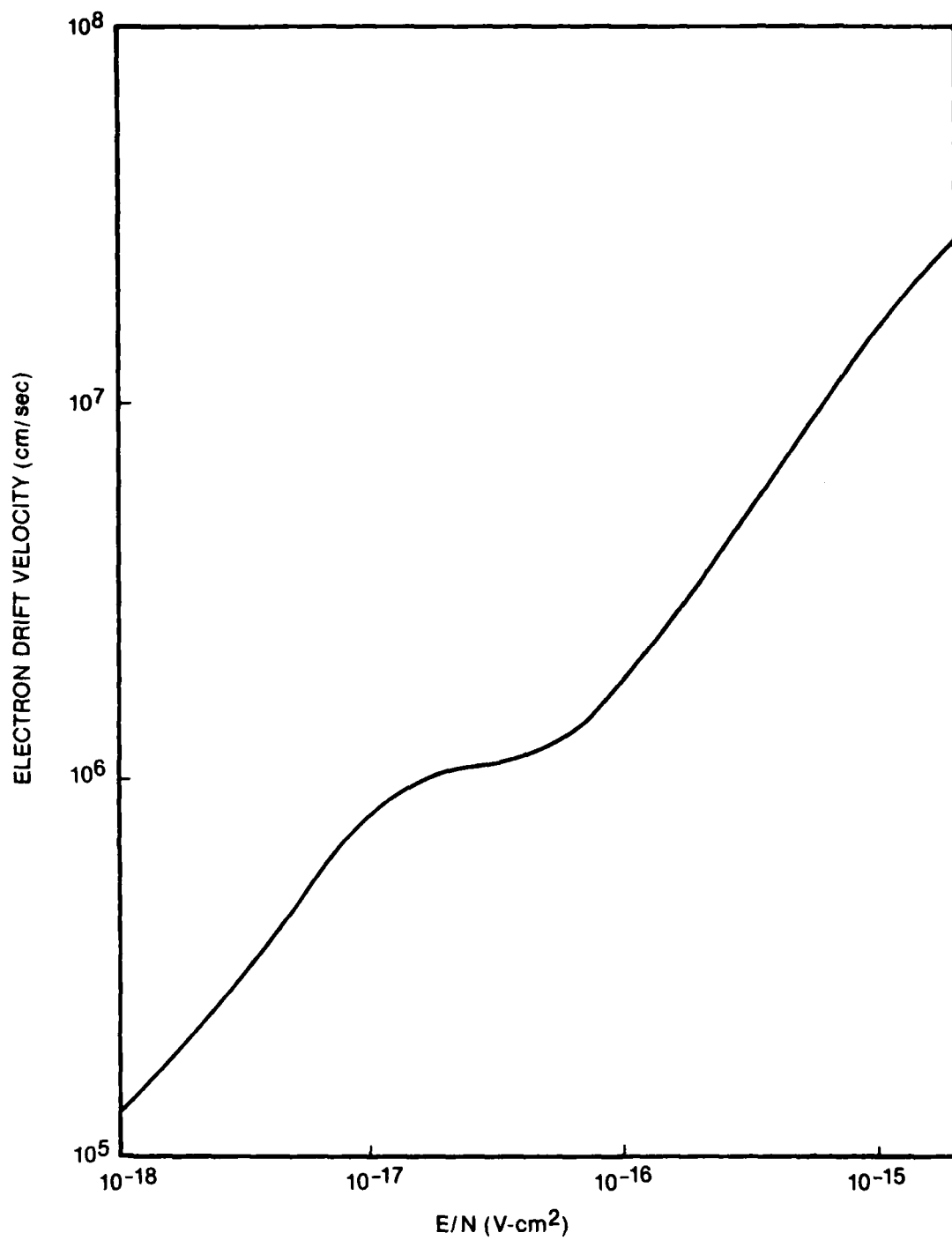
Figure 10. Electron Drift Velocities for He/Xe/HCl Mix of 94.8/5/0.2.

15

The most significant ionization processes are electron-neutral collisions with the ground-state Xe (5p) and the Xe (6s) metastable, that is,

$$Xe + e \rightarrow Xe^+ + 2e \qquad (2)$$

$$Xe^* + e \rightarrow Xe^+ + 2e \qquad (3)$$

where Xe* denotes the metastable. The Xe* population is zero prior to application of the electric field; therefore, the population growth is due primarily to

$$Xe + e \rightarrow Xe^* + e \qquad (4)$$

Also contributing to metastable formation is cascading of higher-lying Xe levels. The cross sections of Fig. 2 show that the collective cross sections of the 6s', 6p, and 5d levels have a threshold of $\sim$ 9.7 eV and exceed the 6s cross sections for energies above $\sim$ 10.5 eV. At high electric fields upper-level population can become significant when compared to direct excitation to the metastable. At a moderate E/N of 10^{-16} V-cm^2 (near where the discharge generally operates), the number of electrons having energies greater than 10 eV is < 20% of those having energies of 8 to 10 eV. Assuming that one-half of the upper-level transitions end up in the 6s metastable state, one could expect as much as a 10% error in predicted metastable population if the upper-level formation is ignored.

A second cascade channel is that entered through electron-ion dissociative recombination of the Xe_2^+ ion. This will be discussed in more detail later. Although this reaction can be very fast, the formation of Xe_2^+ is fairly slow and is competitive with the ion-ion recombination ($Xe^+ + Cl^-$) formation of the upper laser level. The dimer-ion recombination could be significant only near the end of the discharge pulse and, therefore, is not expected to contribute significantly to the population of the Xe* metastable for the majority of the discharge cycle.

In addition to the downward cascading of excited-state populations, electron-collision excitation from the metastable also occurs. Since it is the total

population of the metastable which is of concern in the discharge model, this loss mechanism would somewhat offset the error introduced by omission of the cascade channels. The complexity of tracking the excited-state populations does not seem to be justified, considering what appears to be only a marginal increase in model accuracy. Therefore, the only channel included in the model is direct electron-impact excitation [Reaction (4)], and the only loss channel is electron-impact ionization [Reaction (3)].

Due to the large disparity between the rate coefficients for metastable production and those for metastable losses, a "saturation" condition for Xe* population will exist. That is, the large rate coefficient for ionization (loss) will prevent the metastable population from becoming large. The allowable steady-state population is shown in Fig. 11. Under transient conditions, populations may differ for a short time, depending on the total electron density. However, a very large overvoltage condition must exist in order for the metastable population to exceed the total number of Xe molecules by several percent. As will be shown later, populations in excess of 0.1% are unlikely. For this reason, de-excitation collisions of electrons with the Xe metastable (collisions of the second kind) have been ignored. Detailed energy-balancing calculations have shown that for the E/N range of interest, this loss channel is insignificant when compared to both the ionization-loss channel and the excitation (formation) channel.

Two additional ionization channels which occur in the He-rich mixture are He electron-impact ionization

$$He + e \rightarrow He^+ + 2e \tag{5}$$

and Penning ionization

$$He^* + Xe \rightarrow He + Xe^+ + e \tag{6}$$
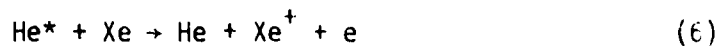
where He* denotes the He 2^3S metastable. The formation channel of He* is

$$He + e \rightarrow He^* + e \tag{7}$$

17
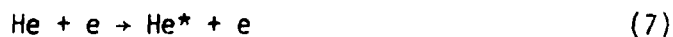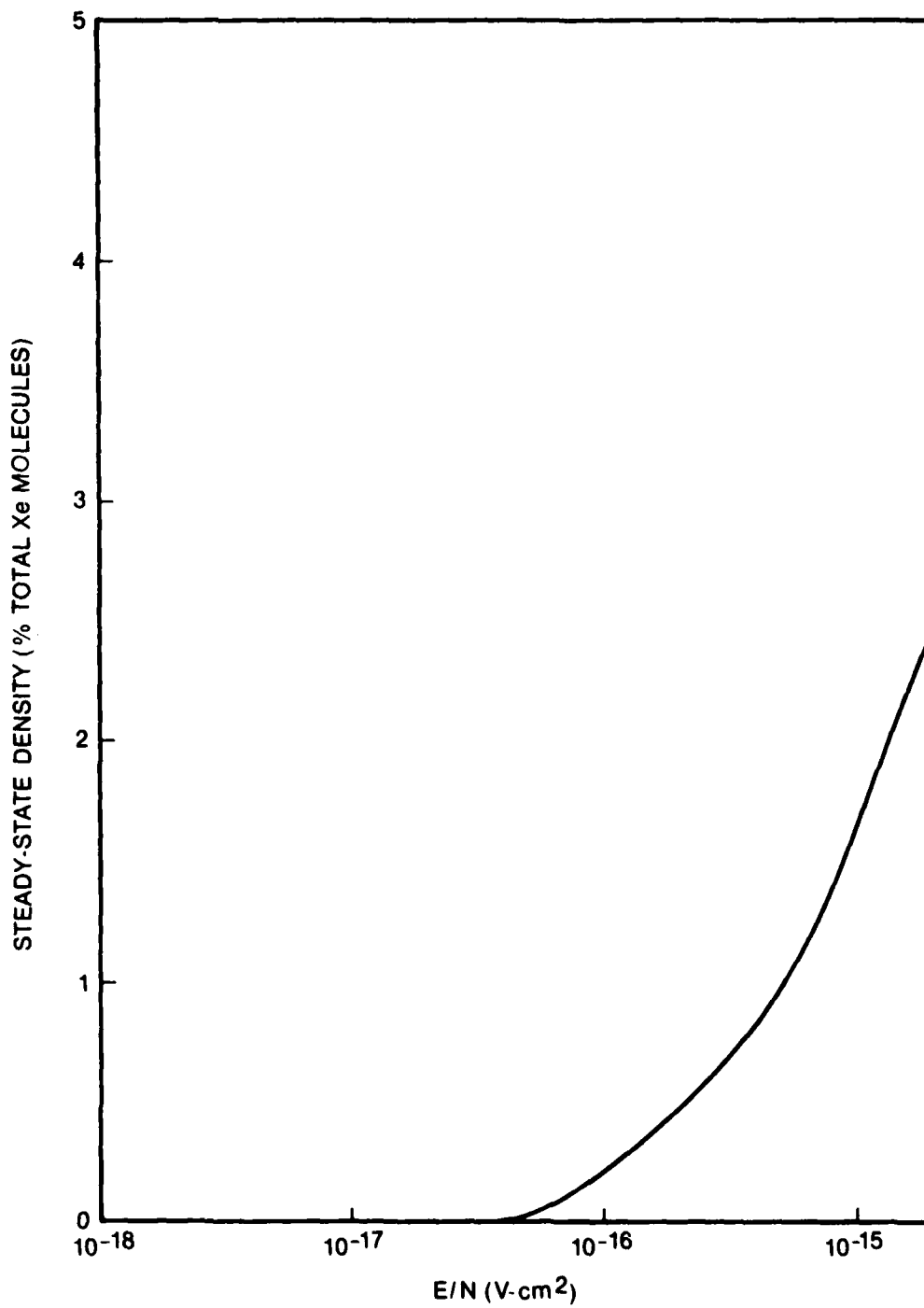
Figure 11.   Steady-State Density of [Xe*] as Percent of Total Xe Molecules.

The threshold for (5) is 24.6 eV, and the cross sections are relatively small. However, since 95% of the discharge is He, the process could be significant at high E/N values and is, therefore, included in the model. Since Reaction (6) is very rapid (near gas-kinetic), the rate for Reaction (7) determines the level of Penning ionization. The threshold for 2^3S metastable formation is $\sim$ 19.8 eV, and the cross sections are relatively small. Therefore, metastables will be created only during the initial overvoltage of the discharge gap and will be lost very quickly after the E/N falls. Again, due to the high density of the He, Penning ionization could be significant, but only up to a time shortly following the electric-field collapse.

The major source of electron loss in the He/Xe/HCl mixture is dissociative attachment; that is,

$$HCl \ (v = 0) + e \rightarrow HCl^- \rightarrow H + Cl^- \qquad (8)$$

$$HCl \ (v = 1) + e \rightarrow HCl^- \rightarrow H + Cl^- \qquad (9)$$

$$HCl \ (v = 2) + e \rightarrow HCl^- \rightarrow H + Cl^- \qquad (10)$$
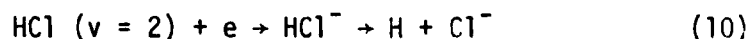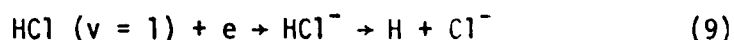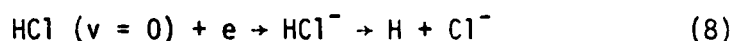
At room temperature the populations of vibrationally excited HCl are essentially zero. Therefore, the excitation channels

$$HCl \ (v = 0) + e \rightarrow HCl \ (v = 1) + e \qquad (11)$$

$$HCl \ (v = 0) + e \rightarrow HCl \ (v = 2) + e \qquad (12)$$
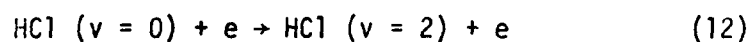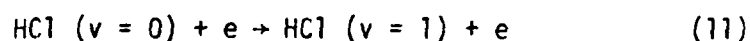
must also be included in the model. The significance of attachment via the vibrationally excited states is demonstrated in the attachment-rate curves of Fig. 8. At E/N = 10^{-16} V-cm^2, attachment for v = 1 is $\sim$ 30 times greater than for v = 0, and the v = 2 rate is $\sim$ 580 times higher than the v = 0 rate coefficient. Also, the vibrational-excitation-rate coefficients (Fig. 7) are fairly rapid, indicating that a very significant amount of attachment can be expected.

19

It is interesting to note that since the total concentration of HCl is relatively small ($\sim 10^{17}$ cm^{-3}) and excitation-rate coefficients are fairly large, the excited-state populations can become sufficiently large relative to the ground-state population that the reverse reaction--electron-collisional de-excitation--will become significant. The rates of this reverse reaction--calculated through detailed energy balancing--are comparable to those of the forward reactions at moderate-to-high values of E/N and are much greater at low E/N. This means that the formation of vibrationally excited HCl will be limited by a balance of all three states. Since the reaction cross sections are functions of electron energy, the relative proportions of excited and ground-state densities will be a function of E/N. Figure 12 shows this functional dependence in a steady-state situation.

Since these values are for steady-state conditions, transient values may differ somewhat, especially if the discharge electric field changes rapidly. For example, consider the case where saturation is attained at E/N = 10^{-16} V-cm^2 and then the field drops to near zero. At this low value of E/N, the excited-state densities will decrease fairly rapidly; but very fast attachment will also occur, due primarily to the presence of the $v = 2$ level where the attachment rate increases by a factor of three as the E/N decreases (see Fig. 8). This means that the effective rate of electron loss is greater with a rapidly falling E/N than with a more gradually decreasing field. Of course, one must also bear in mind that the total concentration of HCl will continually decrease during the discharge cycle due to loss by attachment; Fig. 12 represents to relative populations only.

Another loss process of the vibrationally excited HCl is v - T relaxation. Available data[16] show rates for the $v = 1 \rightarrow 0$ reaction of $< 10^{-16}$ cm^3 sec^{-1}. One could expect the $v = 2 \rightarrow 1$ rates to be on the same order of magnitude. Assuming one-half of the HCl population to be in a vibrationally excited state, at 2 atm. total gas pressure, an electron density of three to four orders of magnitude less than the HCl density would be required for the v - T to become significant with respect to vibrational excitation at E/N above $\sim 10^{-17}$ V-cm^2. The v - T process can be ignored in the discharge model since, generally, $n > 10^{14}$ cm^{-3}.
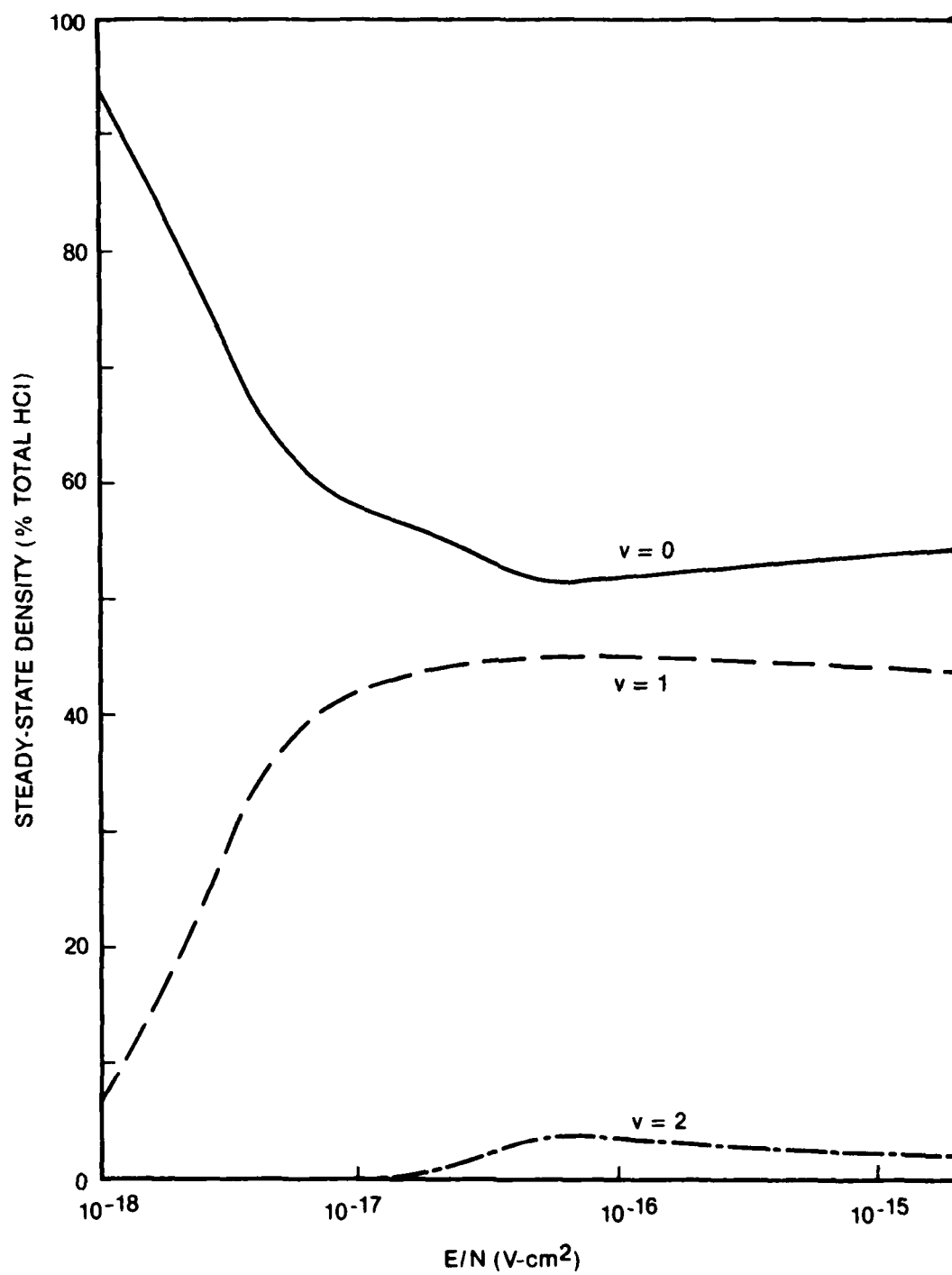
Figure 12. Steady-State Densities of HCl Vibrational Levels.

Recombination reactions leading to electron loss in the He/Xe/HCl discharge are

$$He^+ + e \rightarrow He + h\nu \tag{13}$$

$$Xe^+ + e \rightarrow Xe + h\nu \tag{14}$$

$$Xe_2^+ + e \rightarrow Xe + Xe** \tag{15}$$

where Xe** denotes a range of excited states of Xe. Recombination rates are dependent upon average electron temperature (T_e), with the rate decreasing at $\sim T_e^{-0.5}$ to $\sim T_e^{-0.7}$. The rates[17] for radiative recombination [Reactions (13) and (14)] are small for $T_e > 10^4$ K, as is generally the case for the majority of the duration of a discharge pulse. The dissociative recombination of Xe_2^+ [Reaction (15)], however, is very rapid. In addition to being a function of T_e, this process also varies with pressure, reaching a maximum at ~ 1 atm. for the conditions under consideration here. For all practical purposes this reaction is near gas-kinetic at 1 - 2 atm., with a temperature dependence[18] of $T_e^{-0.72}$. The formation of Xe_2^+, however, is a three-body reaction

$$Xe^+ + Xe + M \rightarrow Xe_2^+ + M \tag{16}$$

where M is a Xe or He chaperon. The rate coefficient for this reaction is relatively low (on the order of 5.9×10^{-33} cm^6 sec^{-1}).[19] For the mixture considered here, the two-body equivalent rate at 2 atm. is 2.8×10^{-13} cm^3 sec^{-1}, which is significant only if the main competing reaction

$$Xe^+ + Cl^- \rightarrow XeCl* \tag{17}$$

is slow. Since the ion-ion recombination reaction--which, incidently, is the main channel for upper-laser-level formation--is near gas kinetic, the Xe^+ ion will be available for significant formation of the dimer ion only while the Cl^- density is low. In general, one can say that due to the large attachment and rapid formation of Cl^- during a discharge, much of the Xe^+ created will be mopped up by ion-ion recombination, preventing the dimer-ion

dissociative-recombination process from contributing significantly to electron loss. Since the rate of Cl⁻ formation will generally increase as the E/N falls, the Xe_2^+ density is not expected to be available in any appreciable amount ($> 10^{14}$ cm^{-3}). An exception would be in the case of a very slowly falling E/N, where HCl dissociative attachment would decrease to near zero.

The validity of using a single set of E/N-dependent reaction rates for the duration of the discharge must now be examined. Modeling experience has shown that in a self-sustained discharge in a typical He/Xe/HCl mixture, nearly one-half of the HCl molecules may be in the first vibrationally excited state (v = 1). Also, approximately 0.1% of the Xe density will be in the Xe (6s) metastable level. These conditions will affect the electron energy distribution since HCl (in the ground state as well as vibrationally excited states) exhibits various large inelastic cross sections at low electron energies. Also, the inelastic ionization cross section of the Xe (6s) is quite large above the threshold value 3.81 eV.

A worst-case condition was chosen by calculating the species populations in a discharge vigorously excited by a practical pulse-forming network. The Xe (6s) population increased to 0.19% of the original Xe (5p ground state), with a corresponding decrease in the 5p population. The HCl (v = 0) population decreased by $\sim$ 45%; the v = 1 level increased from zero to $\sim$ 41% of the original v = 0 population; and the v = 2 level increased to $\sim$ 3.6% of the original v = 0 value. Considering the pre-discharge gas composition of 94.8/5/0.2 (He/Xe/HCl), the major effect on the electron energy distribution was attributed to the HCl population change. The most significant change was caused by the decrease in the v = 0 level, resulting in a decrease in the process HCl (v = 0) + e → HCl (v = 1) + e. The inelastic cross section for this process has a peak value of $\sim$ 7.1 × 10^{-15} cm^2 at 0.14 eV and is $> 10^{-15}$ cm^2 below $\sim$ 0.6 eV. The major effect observed was an increase in electron mean energy for E/N values between $\sim$ 3 × 10^{-18} and $\sim$ 5 × 10^{-17} V-cm^2 and an increase of as much as 100% in the reaction rates for the low-energy processes--HCl vibrational excitation and attachment--in this E/N range. The slight increase in Xe (6s) population has a small influence on the electron-energy distribution function for E/N values above $\sim$ 5 × 10^{-16} V-cm^2 (ionization cross section of the 6s level is above 10^{-15} cm^2 from $\sim$ 6 eV to

above 60 eV). This has the effect of lowering the ionization rate for both the ground state and the metastable level--by less than 15%--for the E/N range of $\sim 5 \times 10^{-17}$ to 10^{-16} cm^2. Above this, no effect is observed.

In summary, some error is introduced into the discharge model over an E/N range of $3 \sim 10^{-18}$ to 5×10^{-17} V-cm^2; the extent of the error is dependent upon the length of time during which this range is maintained. A minor error would be introduced for an E/N range of 5×10^{-17} to 10^{-16} V-cm^2. Experimental data indicate that vigorous excitation is required for optimum laser performance; and modeling has shown that under typical discharge conditions, an E/N of $\geq 7 \times 10^{-17}$ V-cm^2 exists, except during short periods of turn-on and turn-off. Therefore, the error resulting from a change in the chemical composition of the original gas mixture is insignificant.

One other factor must be considered. The electron number density can exceed 10^{15} cm^{-3} at the peak of the discharge current. Electron-electron collisions, therefore, are significant and the electron distribution function tends toward a Maxwellian. To demonstrate this effect the AFWAL/APL Boltzmann code was run with a fractional ionization of 10^{-4} and an electron density of 2×10^{15} cm^{-3}. The chemical changes as discussed above were also included. The results for various values of E/N are compared to the rate data obtained from the Boltzmann-code runs which ignored the electron-electron collisions and chemical changes. The results are shown in Figs. 13-17.

The most significant changes are in the ionization rates of Xe (both 5p and 6s) and the drift velocity. Considering that the 6s density is $\sim 0.2\%$ of the ground-state density at E/N = 10^{-16} V-cm^2 the decrease in the 6s ionization rate counteracts the increase in the ground-state ionization rate, leading to similar total ionization rates for these two conditions. At lower values of E/N, the total ionization rate could deviate markedly; however, since the rates decrease sharply, the overall effect on the discharge conductivity is small. Similarly, the drift velocity for E/N $\simeq 10^{-16}$ V-cm^2 varies by < 10%; this deviation decreases as E/N increases. It is interesting to note that the sharp positive-resistance characteristic of the discharge which is caused by the decreased slope of the v_D-vs-E/N function for
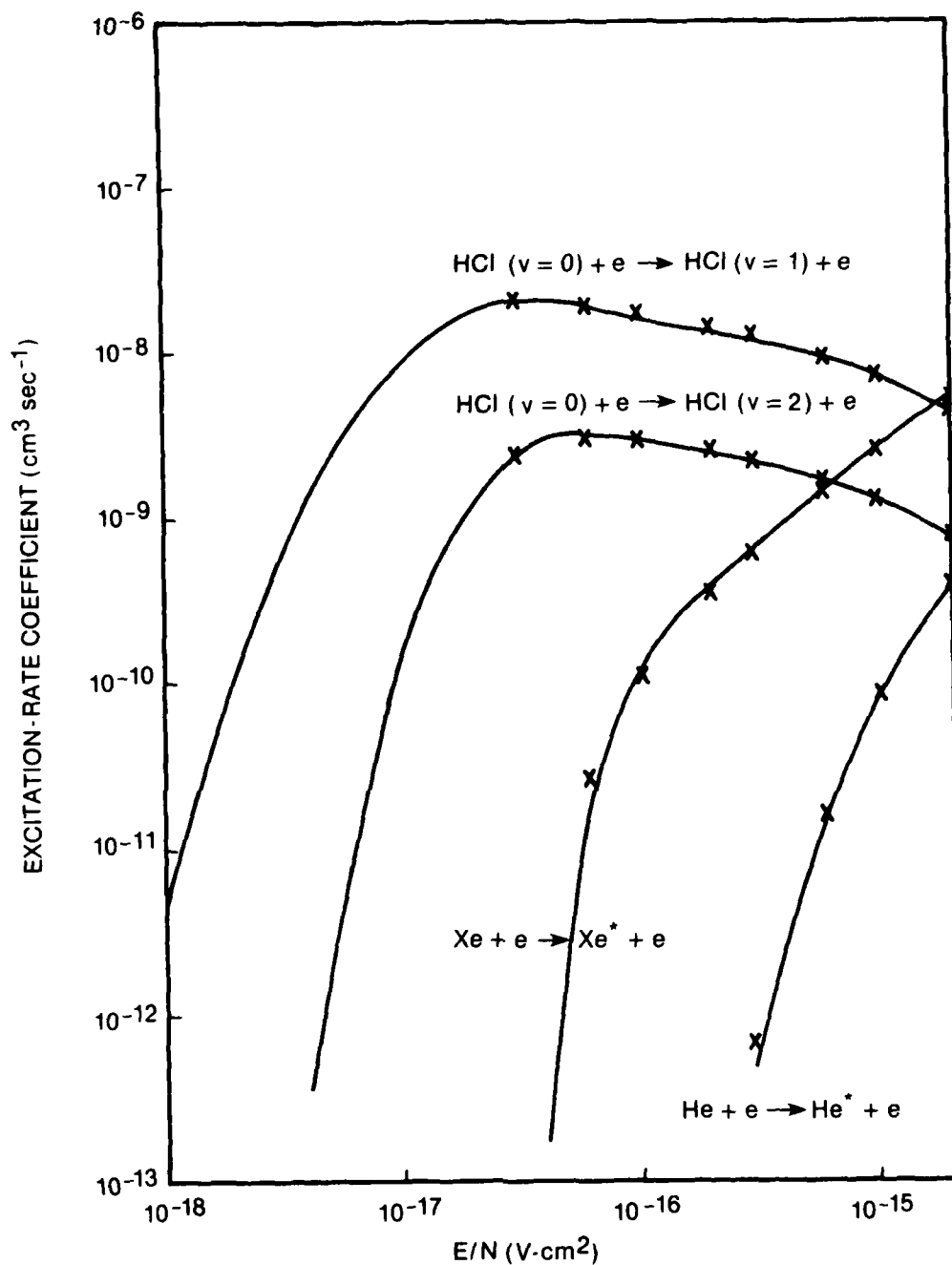
Figure 13. Excitation Rates for He/Xe/HCl Mix of 94.8/5/0.2. Solid line represents $n_e = 10^{12}$ cm^{-3} and all species are in the ground state. x indicates points for which $n_e = 2 \times 10^{15}$ cm^{-3}, fractional ionization of 10^{-4}, and excited-state species are present.

25
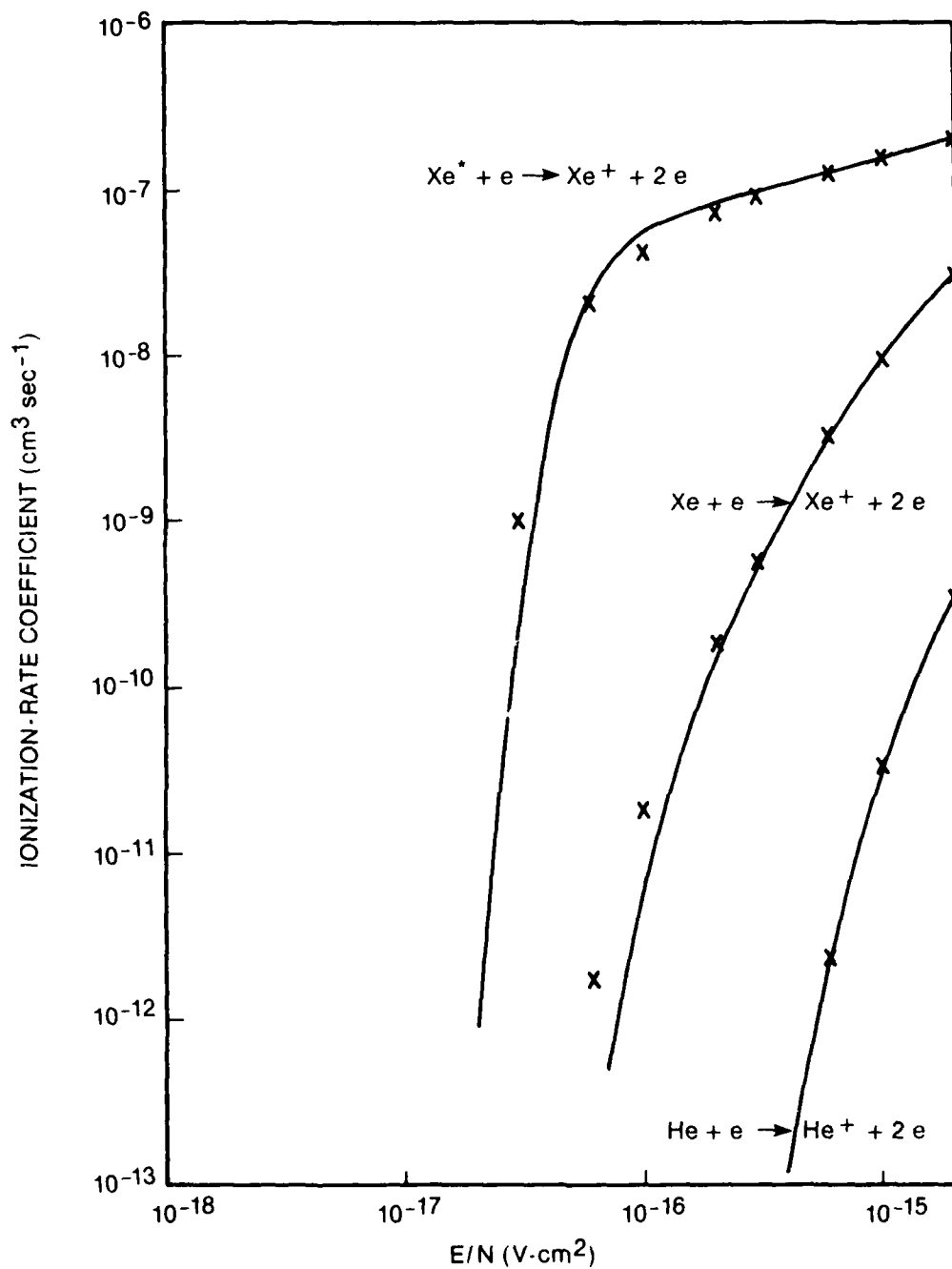
Figure 14. Ionization Rates for He/Xe/HCl Mix of 94.8/5/0.2. Solid line represents $n_e = 10^{12}$ cm^{-3} and all species are in the ground state. x indicates points for which $n_e = 2 \times 10^{15}$ cm^{-3}, fractional ionization of 10^{-4}, and excited-state species are present.
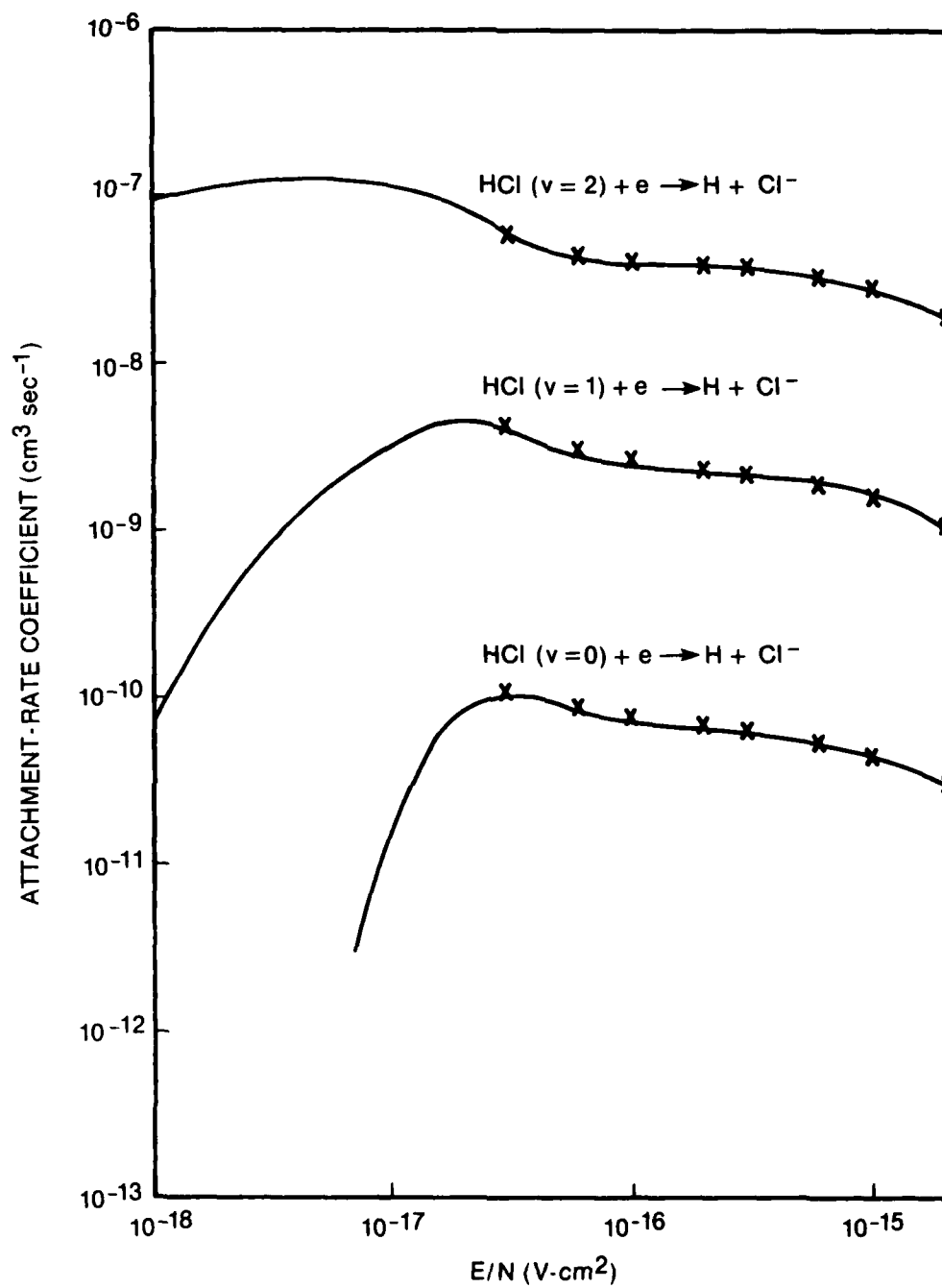
Figure 15. Attachment Rates for He/Xe/HCl Mix of 94.8/5/0.2. Solid line represents $n_e = 10^{12}$ cm^{-3} and all species are in the ground state. x indicates points for which $n_e = 2 \times 10^{15}$ cm^{-3}, fractional ionization of 10^{-4}, and excited-state species are present.
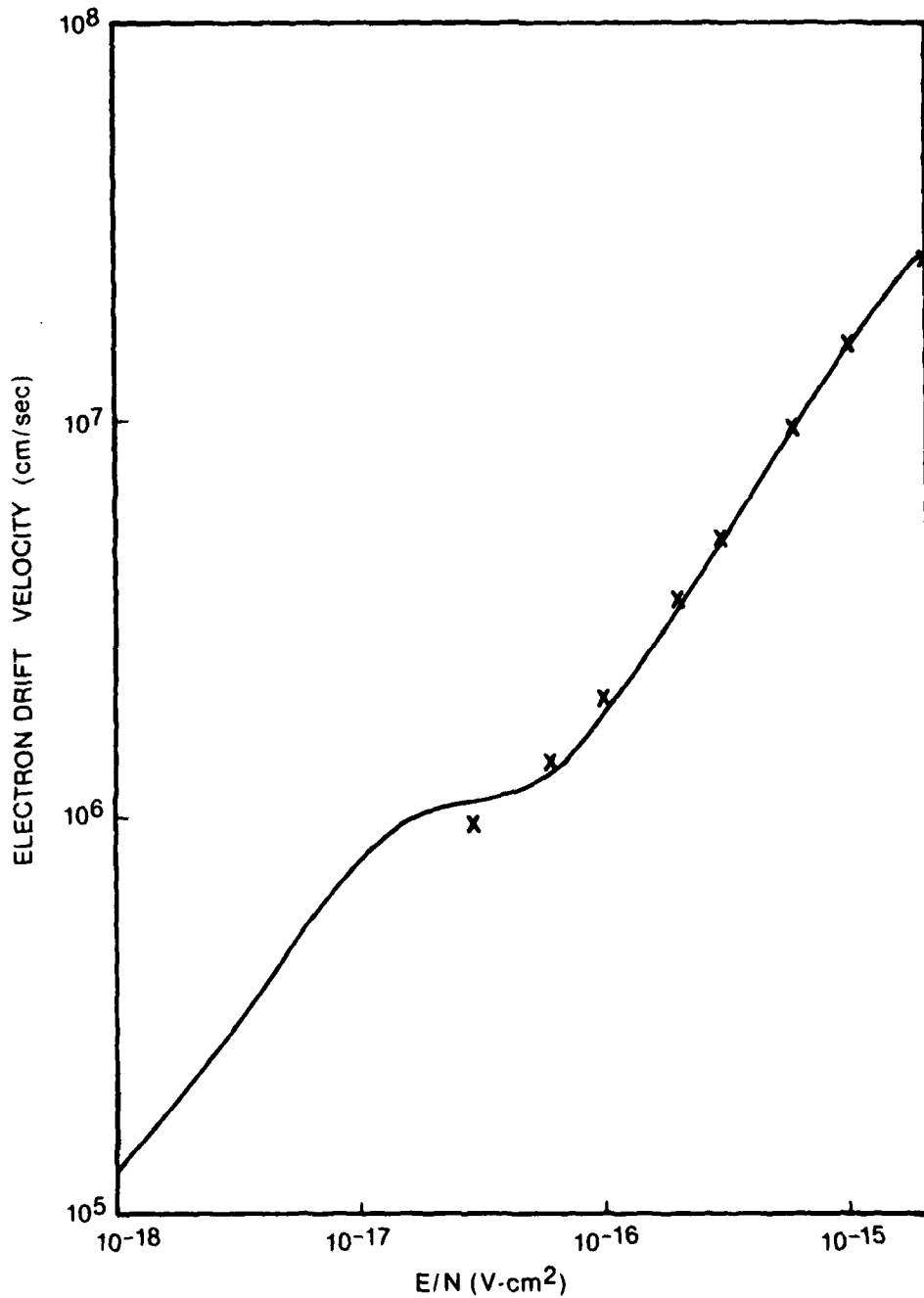
Figure 16. Electron Drift Velocities for He/Xe/HCl Mix of 94.8/5/0.2.
Solid line represents $n_e = 10^{12}$ cm^{-3} and all species are in
the ground state. x indicates points for which $n_e = 2 \times 10^{15}$
cm^{-3}, fractional ionization of 10^{-4}, and excited-state
species are present.
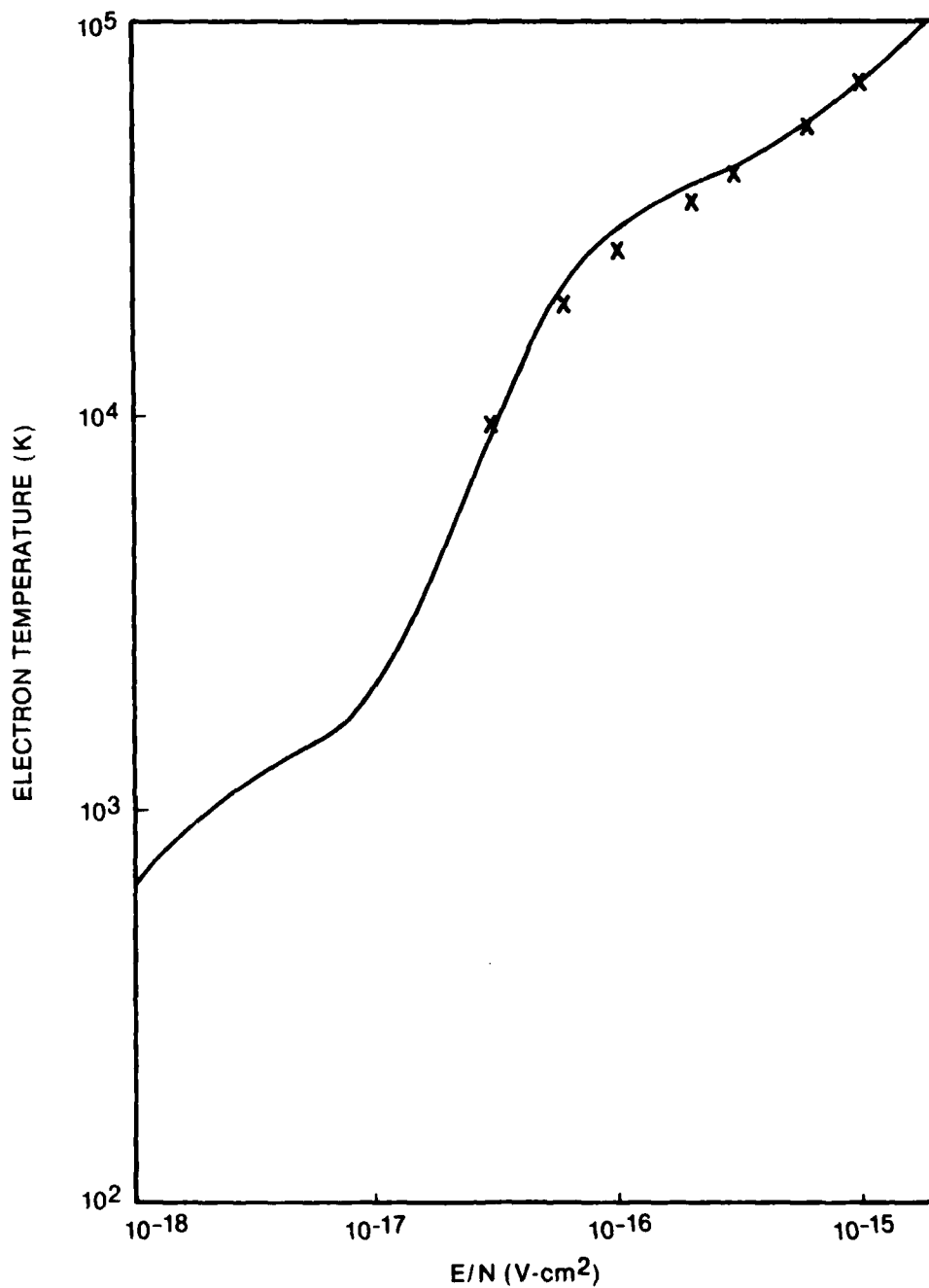
Figure 17. Electron Temperatures for He/Xe/HCl Mix of 94.8/5/0.2. Solid
line represents $n_e = 10^{12}$ cm^{-3} and all species are in the
ground state. x indicates points for which $n_e = 2 \times 10^{15}$ cm^{-3},
fractional ionization of 10^{-4}, and excited-state species are
present.

29

the E/N range ~ 1.5 to 7×10^{-17} seems to disappear at large electron densities.

Therefore, a single set of rates may be used throughout the discharge cycle for the purpose of modeling the electrical characteristics of a typical XeCl laser discharge. The conditions used in the circuit modeling for the remainder of this report are: (1) no electron-electron collisions, (2) $n = 10^{12}$ cm^{-3}, and (3) all gas species in their ground states. Of course, these assumptions apply only to the calculations of reaction rates, drift velocity, and electron temperature. All pertinent populations and reactions are considered in the discharge computations.

The goal of the modeling effort was to predict the circuit interaction between the pulse-forming network (PFN) and the discharge. Since large amounts of energy must be deposited in the discharge in very short periods of time (< 200 nsec.), the PFN is generally passive, and the interaction is severe. Specific circuits will be discussed later, but the reaction-rate data obtained from the Boltzmann analysis incorporating the above simplifications can be used to determine some general characteristics.

As discussed earlier, steady-state rates of the dominant two-step processes of ionization and attachment will exist if a gap E/N can be maintained for a sufficient period of time. The time required will be greatly influenced by n. In the transient case--which exists at discharge initiation, for example--the effective rate coefficients will vary, depending upon the populations of the intermediate steps as determined by the previous kinetic action. Figure 18 demonstrates the mixture-weighted (effective) rate coefficients of the ionization and attachment processes as a function of E/N for various populations of the intermediate levels. A relatively small amount of Xe metastable (Xe*) will dramatically affect the ionization rate. The attachment rate is influenced by the amount of HCl (v = 1)--up to $\sim 45\%$. However, the presence of only a small amount of HCl (v = 2) will greatly influence the electron loss processes.

For the mixture considered here (94.8/5/0.2 He/Xe/HCl), the top line in the group of attachment curves of Fig. 18 represents the maximum effective

30
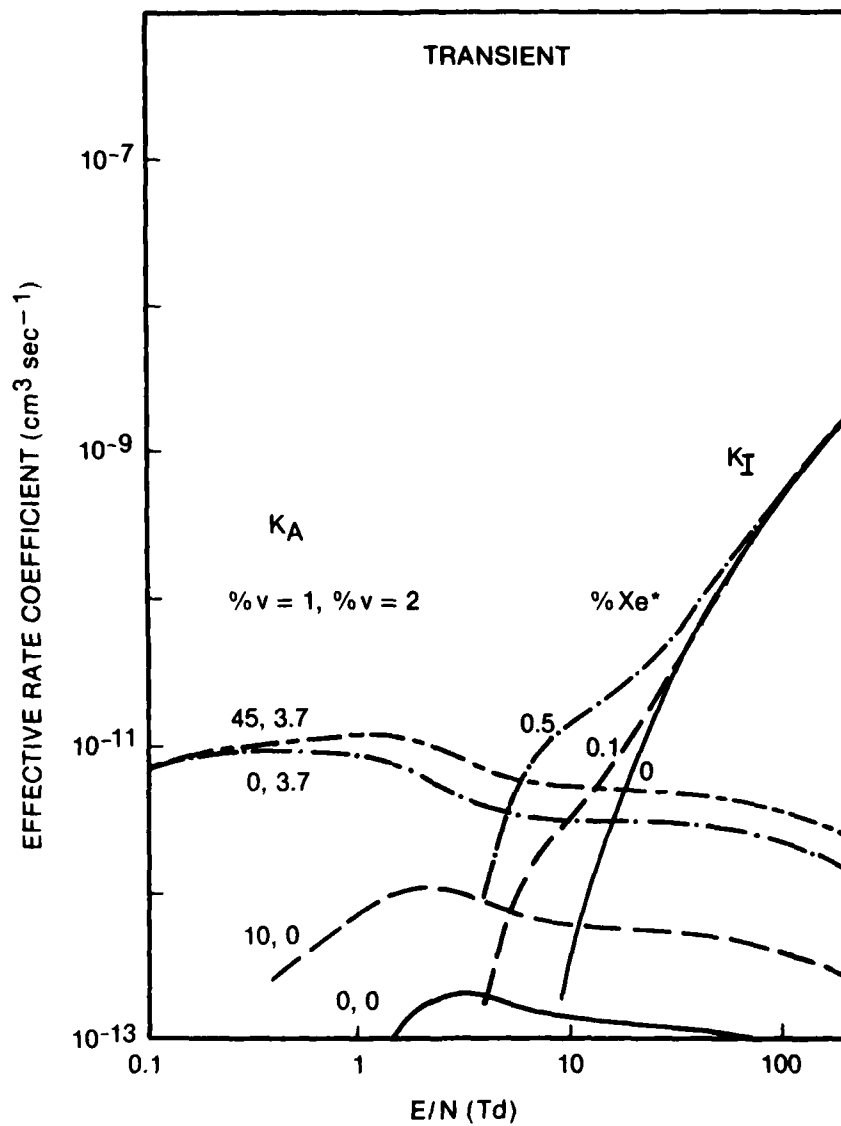
Figure 18. Transient Mixture-Weighted Ionization (K_I) and
Attachment (K_A) Rate Coefficients for Various
Concentrations of Excited States.

31

attachment rates, with energy balancing and production and loss processes being taken into account. Theoretically, concentrations of Xe* could be higher than those shown, but concentrations as high as 0.5% would be difficult to achieve in practice.

An important aspect of the kinetics, to be considered here, is the relative pumping rates of the excited states. Figure 19 shows the excited-state pumping-rate coefficients mixture weighted for the initial concentrations of the ground states. The term "effective" is in quotation marks because, as the HCl becomes vibrationally excited, the ground-state concentration decreases by almost 50%; also, the total rate of HCl excitation will be affected by collisions of the second kind. The attachment curves, therefore, represent maximum transient values. The ground state of Xe, however, remains relatively constant throughout the discharge period. Considering this and the fact that the $v = 2$ species is the dominant attacher, two-step ionization proceeds at a more rapid rate than two-step attachment for E/N values above $\sim 7 - 8$ Td.

By a balancing of production and loss processes, the mixture-weighted attachment and ionization-rate coefficients in the steady state can be found; these are shown in Fig. 20. Since the formation of the Xe metastable is a relatively high-energy process while the loss process has a fairly low energy threshold, the effective ionization-rate coefficient has a strong functional dependence upon E/N. Attachment does not exhibit this strong E/N dependence, except at lower energies, since both production and loss of the HCl excited states are relatively low energy processes.

As long as the gas composition remains constant, the rate coefficients of Fig. 20 will be maintained. If the Xe or HCl concentrations change (e.g., through burn-up) or if other species are formed which affect the electron production or loss processes, a steady state will not be achieved. For example, atomic Cl is a byproduct of the XeCl laser transition. If the concentration of molecular Cl_2 builds up to a significant level, the electron distribution function will change and attachment to Cl_2 and its vibrationally excited states will take place. Other detrimental effects on laser action will also occur, but only the electrical characteristics are considered here.

32
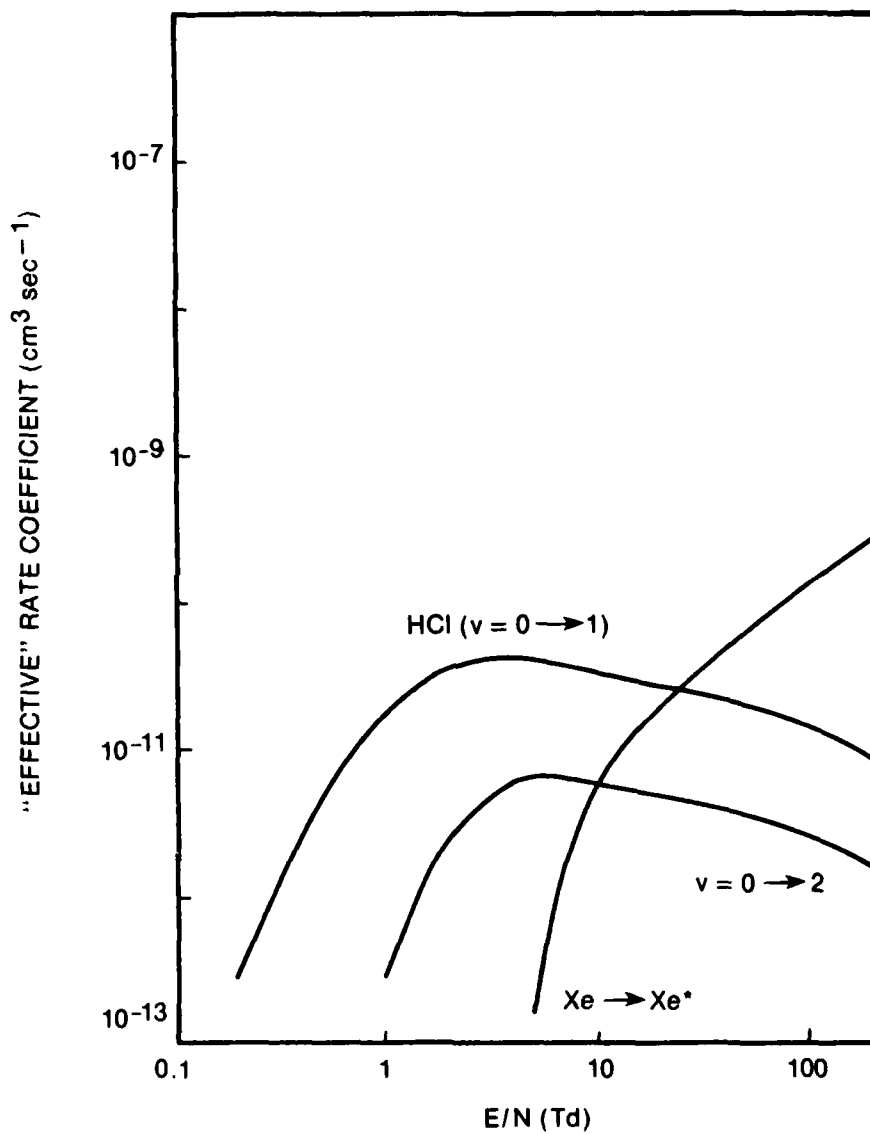
Figure 19. Mixture-Weighted Pumping-Rate Coefficients
for Formation of Excited States Pertinent to
Two-Step Ionization and Attachment Processes.
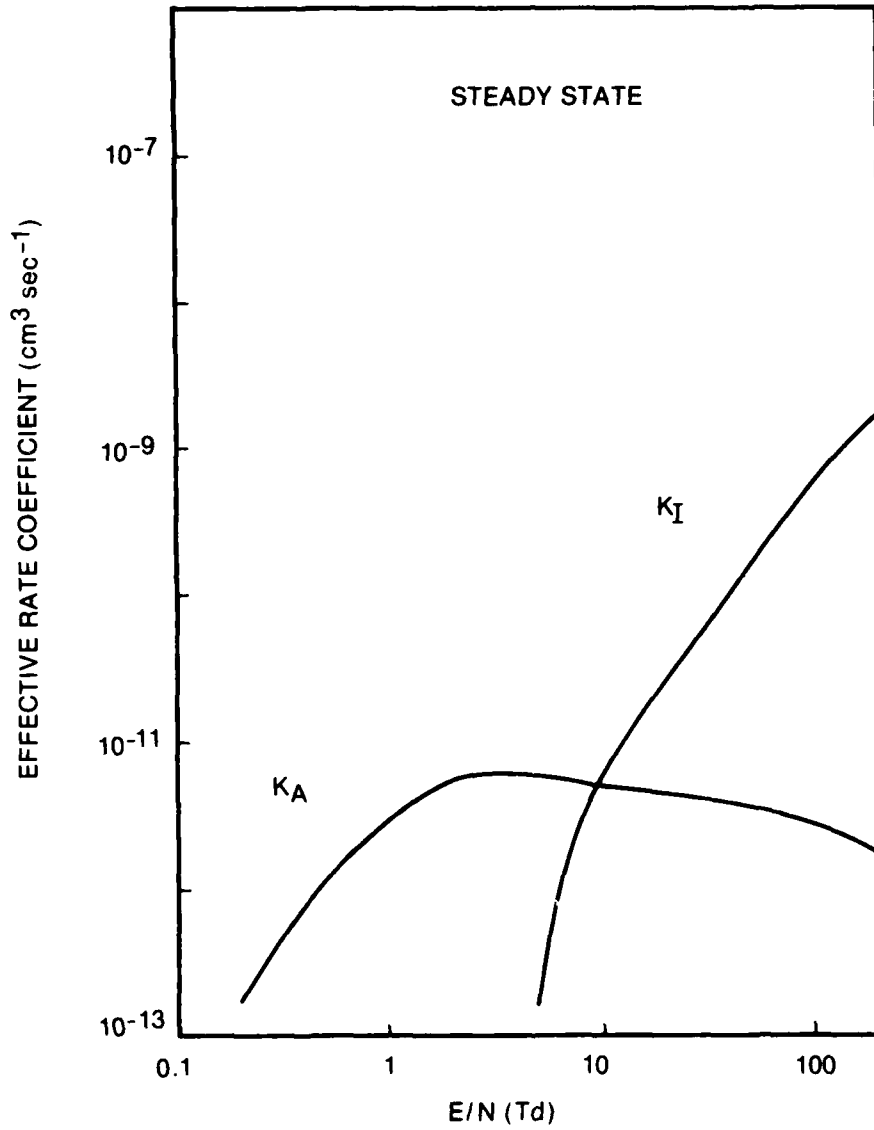
Figure 20. Steady-State Mixture-Weighted Ionization (K_I) and Attachment (K_A) Rate Coefficients.

Fortunately, for the XeCl system, no species is formed in sufficient quantity in the time frame of interest ($\leq$ 150 nsec.) to have significant effect on the electron distribution function or on the electron production or loss processes. The only change observed for typical gas mixtures utilizing HCl as the donor is burn-up of HCl. Therefore, in the glow phase of the discharge (quasi-steady state phase following breakdown), the values of K_A in Fig. 20 will decrease with time. Since the K_I curve is relatively steep where K_A and K_I intersect, the value for E/N at which electron production balances electron loss will be a slowly decreasing function of time. This rate of decrease is primarily dependent upon electron density. Therefore, the burn-up rate will increase with an increase in electrical-power deposition.

As a result, if the PFN allows a discharge--in the typical laser mixes incorporating HCl--to operate in the glow phase for a significant period of time, the assumption of a constant E/N can be cautiously applied. This would greatly simplify circuit modeling since a gap which maintains a constant E/N is equivalent to a voltage-sinking circuit component. The transient phases cannot be simplified beyond the kinetic model discussed here. Later in this section, however, some cases are discussed in which general circuit characteristics can be determined without analyzing the transient phases if they are short compared to the time frame of the glow phase.

Before proceeding to the circuit-analysis section, however, the optimum levels of n and E/N should be established. The main channel for upper-laser-level formation in the XeCl system is ion-ion recombination. Since the radiative lifetime of this level is very short[1] ($\sim$ 10 nsec), cavity gain will occur only when ion densities are sufficiently large such that the formation rate of XeCl* is also large, resulting in stimulated--rather than spontaneous--emission. The effective rate coefficient for Cl^- formation is a weak function of E/N (increasing E/N results in a small decrease in the coefficient); therefore, the actual formation rate of the negative ion is primarily a function of electron density. The Xe^+ formation-rate coefficient is a much stronger function of E/N (coefficient increases with increasing E/N); therefore, both n and E/N affect the positive-ion rate of formation.

It seems reasonable, then, that the discharge be operated at the highest possible values of electron density and E/N.

There is, of course, a limit to the electron density at which losses of Xe^+ or XeCl* become significant; dielectronic recombination and electron collisional quenching of the upper laser level are two of these loss processes. Therefore, for optimum operation of a XeCl laser, the range of n is limited, the lower boundary being determined by a minimum pumping rate of the upper laser level and the maximum being determined by electron-induced losses. The present model does not include XeCl loss parameters, but the literature[20] suggests $n \simeq 1\text{-}3 \times 10^{15}$ cm^{-3} as an optimum range. Variations in gas composition and pressure would influence this range but would not appreciably alter it.

Operation at a high E/N increases not only the formation rate of Xe^+ but also the efficiency of Xe^+ formation. That is, at elevated values of E/N, the fractional power going into the ionization channel is greater; this is primarily due to the two-step Xe ionization process. However, for every Xe^+ formed, an electron is also released. Therefore, an elevated E/N can exist only for a short time period before the maximum n_e is exceeded. For example, for the 2-atm. 94.8/5/0.2 He/Xe/HCl mix used in the present model, a value of E/N which is twice that at which the ionization rate is equal to the attachment rate results in a change of n_e from 1×10^{15} cm^{-3} to 3×10^{15} cm^{-3} in less than 10 nsec. During this time ~ 80 mJ/cm^2 of energy would be deposited. For the present 24 cm^2 active electrode area, $\sim 1.5 - 2$ J of electrical energy could be transferred to the gas if a current rate-of-rise of $\sim 10^{12}$ A sec.$^{-1}$ could be accommodated by the electrical circuit. As will be shown later, this is impractical because of inherent stray inductances. Therefore, for medium- and high-power XeCl laser systems ($\geq$ 1 J electrical input), the majority of energy must be delivered at an E/N value at which the electron density remains relatively constant.

Once a discharge has been established, the kinetics will determine the E/N at which the total current remains relatively constant. Since the ionization-rate coefficient is a much stronger function of E/N than the

attachment-rate coefficient, moderate changes in current are accompanied by only small changes in E/N. For this reason, the discharge gap appears to the external circuit as a relatively constant voltage sink.

In other words, for low-energy/short-pulse configurations where the discharge area is small, E/N may be strongly influenced by the external circuit; and it is possible to deposit energy into the discharge at an E/N above the kinetics-determined glow value. For the moderate- and high-power systems of widespread interest, the majority of the power input will occur at an E/N near this glow value, the circuit having very little influence on the gap voltage.

CIRCUIT MODELING

Circuit Modeling

General Considerations

For the present discussion the discharge timing cycle will be broken down into five phases, as shown in Fig. 21. The high voltage in the overvoltage phase utilizes the low-level "seed" electrons resulting from preionization to effect a rapid electron multiplication of approximately seven orders magnitude. The breakdown phase is marked by the onset of significant current and consequent rapid drop in discharge impedance. Due to the typically large current changes and the circuit stray inductances--including the gap self-inductance--the E/N also decreases rapidly. The glow phase is typified by a quasi-steady-state in which electron gains approximately equal electron losses. As mentioned in the preceding kinetics-modeling discussion, a relatively constant E/N will be maintained during this phase for the mixtures of interest. As the electrical power source becomes depleted and can no longer maintain the glow E/N, electron losses (attachment) become dominant in the turn-off phase. Ideally, the discharge cycle will end here. However, as will be seen later, most circuits are not well matched to the discharge. In this case, the excess energy will usually manifest itself in a reversal. This post-pulse phase will exhibit characteristics similar to those of the previous phases; however, most of these characteristics will not be well defined since the electron number density at the start of the post-pulse phase is fairly large.
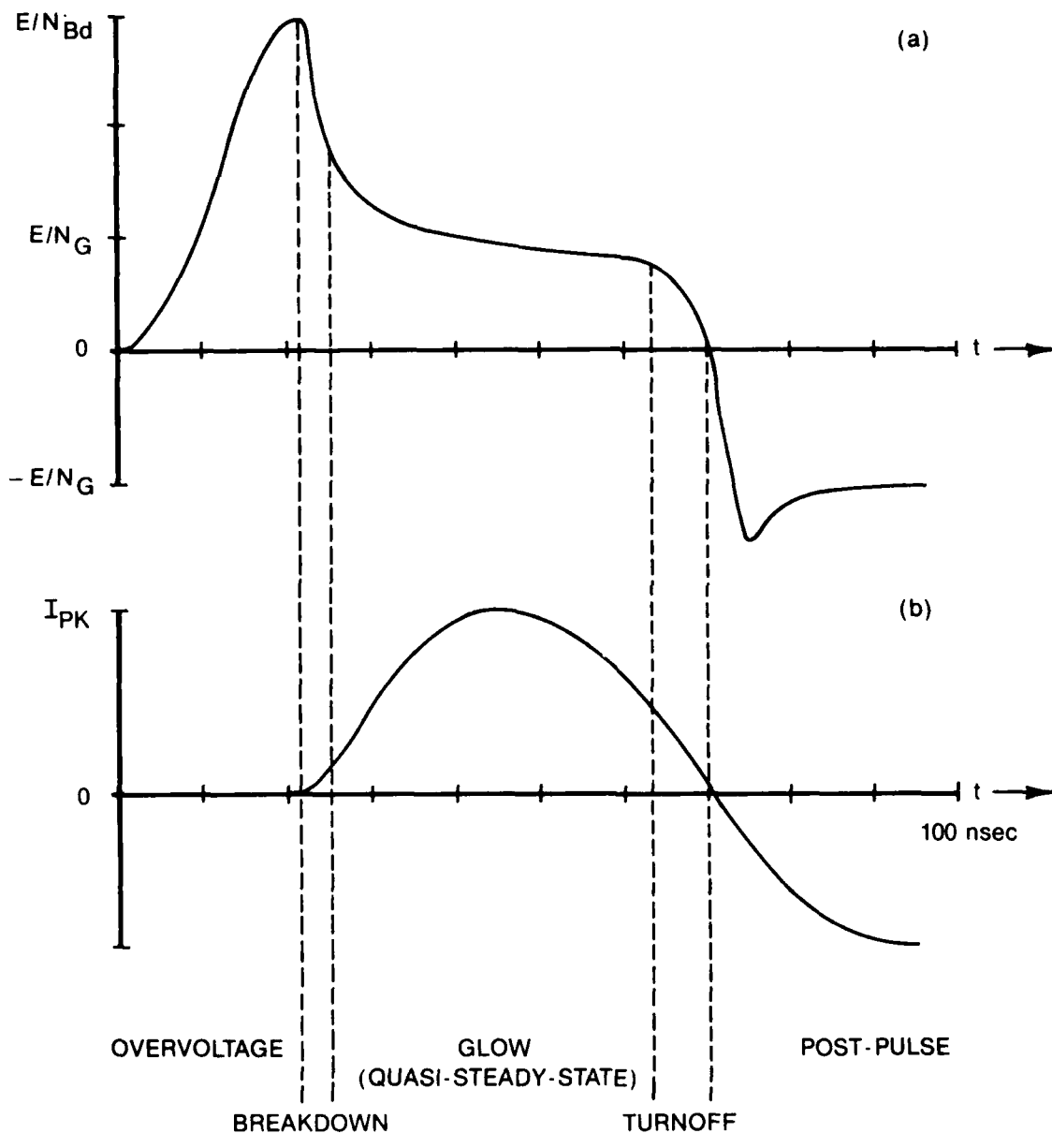
Figure 21. Discharge-Cycle Phases and Typical E/N (a) and Current (b)
Waveforms.

38

Another parameter which must be defined before proceeding is the discharge (or gap) voltage. For this theoretical discussion the AC component of the discharge-gap impedance--i.e., the effect of gap inductance--and the dissipative component will be treated separately. The discharge will be modeled as an inductor in series with an energy-sink component. The effective electric potential seen by the charged particles, then, will be related to the voltage (V) of this dissipative component through neutral-number density (N) and gap spacing (d), i.e., E/N, where E is in volts/cm. Empirically measured gap voltages--such as those discussed in the next section on measurement results--represent the potential of the series combination of inductor and dissipative component. This separation of components is imperative in order to determine the effective E/N as well as to distinguish the energy deposited into the discharge--and removed from the circuit--from the inductively stored--and subsequently returned--energy.

The circuit model and kinetic model are linked through the gap voltage and the total gap current. In the detailed model containing both the kinetics and the circuit models, the SCEPTRE[21] modeling code is utilized. This sophisticated code is designed for ease of analysis of many-component electrical circuits but has the capability to solve additional coupled equations simultaneously with the circuit equations. User-written subroutines, performed at each integration time step, may also be added. The coupled-equation feature is utilized for kinetic calculations; additional subroutines are added to achieve special features such as the simulation of a distributed-element "stripline."

Since capacitor voltage is one of SCEPTRE's state variables,[21] a small capacitor--approximately equal to the pre-discharge gap capacitance--is placed across the gap in the model. Kinetic calculations are then based upon the equivalent E/N of this voltage. The resulting electron density is related to circuit current (I) through Eq. (1). Since the kinetics model is incorporated into the SCEPTRE code as a component model, self-consistent solutions of the complete circuit are obtained.

The instantaneous discharge impedance (dissipative component) is simply the instantaneous value of V/I (V, again, being the theoretical gap voltage with

the inductive component removed). This is significant in that often the current is sinusoidal with time--especially for lumped-element circuits--while the voltage may be fairly constant for a significant portion of the discharge cycle. In addition, the overvoltage phase is marked by high voltage and low current, i.e., a very large impedance. In other words, the discharge impedance for the gas mixtures of interest not only will change abruptly at gap breakdown but also may vary significantly throughout the discharge cycle. The use of a fixed resistor for discharge modeling is, at best, a very crude approximation. Considering the relatively constant voltage glow phase, the resistor model is invalid for the gas mixtures of interest.

Two results of a nonconstant impedance must be emphasized. First, since most of the electrical energy is deposited during the quasi-constant-voltage glow phase, the gap E/N is mixture dependent over a range of values. The rate-coefficient data of Fig. 19 show this range to be generally narrow as evidenced by the steepness of the ionization curve and relative flatness of the attachment curve. Therefore, for a given set of gas constituents, the gap voltage can be adjusted primarily through pressure, gap distance, and gap-area changes--not through variation of mixture concentrations. If gas constituency is changed--e.g., substitution of Ne for He buffer gas--a change in E/N may occur. here again, adjustments in concentrations yield only small changes in E/N and, hence, V. Since electron-drift velocity is a function of E/N, it also is fairly insensitive to moderate changes in concentration.

Secondly, and more importantly, is the effect of electron density upon impedance. The external circuit supplies the gap potential necessary for growth and maintenance of ionization; however, the large, fast changes in n as well as the high levels of n required for fast formation of the upper laser level generally result in large values of I and dI/dt. Circuit impedances, then, cause a drop in gap voltage. In other words, the discharge impedance is dependent upon PFN circuit impedance. Therefore, one cannot merely measure the gap impedance under one set of conditions and then redesign a "matched" PFN because the gap impedance will change.

40

A word of caution is in order here. Often, the term "impedance matching" is used in AC circuit discussions to indicate a situation where optimum energy transfer is made when the impedance of the destination circuit--or load--is equal to the impedance of the source circuit. In the present discussion "power matching" would be a more appropriate term. Or, the term "voltage matching" could be used since most of the energy is transferred to a discharge at nearly constant voltage.

For general discussions of fast discharge circuits, the PFN can be placed in three categories: capacitance dominated (voltage-source), inductance dominated (current source), and distributed element. Theoretically, in the absence of circuit inductance, the capacitor-dominated circuit controls the discharge E/N, with the electron density reaching very high levels if sufficient energy is available in the capacitor(s). In reality, for all but very small area discharges, the rapidly changing circuit current will interact with stray inductances, limiting the E/N after breakdown to values only slightly above the point at which ionization and attachment are equal (see Fig. 20). Current will increase until the capacitor voltage decreases to the level of the gap glow voltage. Current then decreases as the discharge E/N enters the region of net attachment.

A purely inductance-dominated PFN would be essentially a charged inductor, acting as a current source, switched to the discharges. The discharge E/N will lie above the $K_I = K_A$ point (Fig. 20) until the inductor current is established in the discharge. Then the E/N will fall below this point since a negative dI/dt must be maintained. In reality, an adequate opening switch does not exist for realistic values of dI/dt pertaining to all but very small area discharges. Therefore, this type of PFN is impractical at present.

A more realistic approach to the voltage- or current-fed types of PFN's is to consider a capacitor-initiated circuit with realistic stray inductance which limits the current risetime and extends the pulse duration, i.e., a lumped-element LC configuration (to be discussed later in this section).

41

Only the constant-impedance PFN will allow a matching of circuit and discharge for any significant length of time, i.e., for a long constant-voltage glow phase, a constant current can be maintained (see discussion later in this section).

Stray inductance is the parameter having the most dramatic effect on operation of a typical laser discharge of interest to high-rep-rate systems. As mentioned earlier, very small area discharges will minimize the effects of circuit inductance; but, for reasonable laser power levels, areas of $> 10 \, cm^2$ are needed. The system built during this effort has an active discharge area of 24 - 40 cm^2. Since the upper laser level of XeCl* is formed through ion-ion recombination and its radiative lifetime is $\sim$ 10 nsec., it is imperative that a very fast electron growth rate be achieved. To reach n = $10^{15} \, cm^{-3}$ in 30 nsec. in a 24-cm^2 discharge, the current rate-of-change must be $\simeq 2 \times 10^{11}$ amps sec.$^{-1}$. For a series stray inductance of 50 nH, $\sim$ 10 kV would appear across the inductive reactance. In addition, a significant amount of energy may be inductively stored. This energy may be useful later, but the main point here is that a very small amount of stray inductance will significantly affect circuit operation.

High-Repetition-Rate Requirements

One of the major goals of this research program was the attainment of high-repetition-rate operation (> 1 kHz). This could be in bursts of < 1 sec., but the high-rep-rate requirement limited the choice of components. For example, inexpensive BaTi capacitors could not be easily utilized because of their relatively high loss factor. Also, it was necessary to exercise care in the dissipation of the energy remaining in the circuit after the useful energy had been deposited in the discharge. Most of the requirements were met by prudent choices and arrangements of components with the aid of theoretical models incorporating realistically achievable values of stray inductance, capacitance, and resistance.

The major drawback to high-rep-rate operation is the circuit switch. The only switching methods which can accommodate the high currents existing in typical gas-discharge lasers are saturating magnetics and gas discharges.

Suitable magnetic switches have become available only recently. However, the unique features and still relatively unknown high-rep-rate characteristics of these switches cause great difficulty in the general understanding of circuit behavior. This is especially true where variable rep-rate capability is desired since magnetic-saturation characteristics may change dramatically with rep-rate. A separate discussion of the magnetic switch is included at the end of this section.

For all practical purposes a gas-discharge switch was required for the laser system of interest. Spark-gap and rail-gap switches were the most logical choices because of the low-inductance requirement of the circuit. However, these switches are presently limited to low-rep-rate operation. Although "blowing" of a rail gap with a fast flow of gas and utilizing a switch pre-ionizer may result in a high-voltage, high-current, low-inductance switch, this is not proven technology; furthermore, a switch-development program was beyond the scope of the present effort. The only alternative was the somewhat more inductive hydrogen thyratron.

In summary, the main circuit limitation imposed by the high-rep-rate requirement was the presence of an inductive switching component. For the power levels of interest here ($\sim$ 35 kV switched, $\leq$ 5 kA peak current per switch), the minimum stray switch inductance would be $\sim$ 50 nH. Direct parallel operation is not feasible; the common technique of adding inductance for balancing was, obviously, impractical. Parallel circuit operation, where thyratrons are isolated from each other by striplines, is one solution discussed later in this section. The real challenge, then, was to arrive at a circuit configuration which would minimize the effect of the inductive switch on discharge operation.

Computer simulation of the thyratron can be quite complicated. The most accurate model would be based on a low-pressure H_2 discharge. However, severe complications arise from the geometrical arrangement of baffles and grids within the tube structure. In addition, there exists a high degree of fractional ionization as well as rapid, significant chemistry changes[22] of the ions (both positive and negative) and the excited states of H_2 and H. The electron distribution function, drift velocity, and reaction rates may vary dramatically over a relatively short period of time.

43

A simplified model was constructed, based on a double-chamber concept. The grid-cathode and grid-anode areas were treated as separate ionization regions, each having its own "average" voltage-dependent gain and loss rates and drift-velocity function. The two channels were linked by making the ionization rate of the grid-anode space dependent upon the electron number density of the grid-cathode space. Rates and drift velocities were inferred from empirical data.

The simplified model required a sizable amount of computational time and can be considered valid only over the range of empirical data in which fits were made. Similar accuracy over a limited range of parameters can be achieved by modeling the switch as an exponentially decreasing resistance in series with an inductor. This has been found to provide an adequate simulation of the thyratron in a conventional switching configuration. For use in a rectifier mode, however, the thyratron model would generally require the use of the double chamber or a more sophisticated technique.

Unless otherwise noted, the switched-circuit models in this report make use of the inductor-resistor combinations for thyratron simulation. The inductance value is typically 50 nH. Upon triggering, the resistance drops from an "off" value of 10 MΩ to an "on" value of 0.2 Ω, with an exponential time constant of -8×10^8 sec.$^{-1}$. The circuit timing is adjusted in such a way that the delay between trigger application and the onset of current does not introduce significant error. With this method, the voltage drop across the switch is linearly proportional to current; one would expect the voltage of a real thyratron to be a much weaker function of current. However, overall circuit analysis, in general, is not adversely affected.

Lumped-Element Circuits

Lumped-element pulse-forming networks are those discharge circuits which exhibit transient characteristics dominated by capacitive or inductive components. The circuit can be modeled with a limited number of capacitors, inductors, and resistors. In contrast, the distributed-element PFN (to be discussed separately in this section) exhibits the characteristics of an infinite number of capacitor-inductor branches. The lumped-element circuits

44

are generally much easier to construct than the stripline variety and are, consequently, the most commonly used. The most practical lumped-element circuits will be discussed here from the standpoint of depositing energy into an electronegative gas discharge--specifically, a XeCl laser discharge.

The elementary circuit of Fig. 22 is straightforward, but the limitations of power-matching the PFN to the discharge and the characteristics of a practical switch are not so obvious. Since all components are in series, single values may be used for total inductance (L), capacitance (C), and resistance (R) when modeling. The voltage rate-of-rise appearing on the gap is dependent upon the rate-of-closure of the switch. If one assumes instantaneous switch closure, the gap, due to its inherent small capacitance, will "ring-up" to twice the initial voltage (V_0) of C. Obviously, a thyratron switch will take a finite time to close. In fact, it appears that the thryatron impedance will not only be a complex function of time but also be affected by the gap breakdown characteristics. That is, as the hydrogen thyratron ionizes, more of the capacitor voltage will appear on the gap and less across the thyratron. Very little charge will flow initially, resulting in an impeded switch ionization.
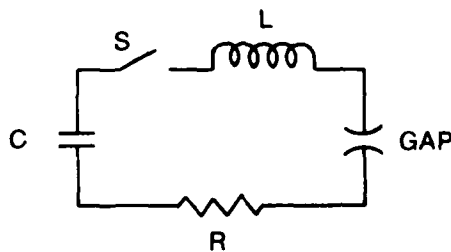
Figure 22. Elementary Lumped-Component Discharge Circuit.

The severity of switch and gap interaction, however, quickly becomes irrelevant when one realizes the greatly limited rate-of-rise of circuit current imposed by the circuit stray inductance. The most obvious way of counteracting the inductive voltage drop(= L dI/dt) is to raise the initial charge on C. However, even if the peak current resulting from this action is

tolerable, the energy transfer between circuit and gap discharge is adversely affected as the capacitor voltage is increased. Also, the energy remaining in the circuit when the discharge current first crosses zero may severely limit the thyratron switch lifetime due to excessive reverse current flow.

For an understanding of energy transfer of a switched capacitor circuit, as well as any LC current in series with a discharge, refer again to the elementary circuit of Fig. 22. Assuming that the capacitor C is charged to a voltage V_0 and that switch closure is relatively fast, a voltage of $\sim V_0$ is initially seen by the gap, resulting in an increase in electron density (assuming an overvolt condition) which leads to an increase in circuit current. This changing current will lower the gap voltage due to the presence of inductor L and the loss of charge on C. However, a net ionization will exist in the gap--and, thus, current growth will continue--until the capacitor voltage and gap voltage are equal. That is, the discharge is voltage-fed until the voltage on C is equal to the kinetics-determined gap potential at which electron-number-density losses are equal to the electron-number-density gains. This voltage was referred to as the glow voltage (V_G) in Fig. 21; the gap will generally maintain approximately this value for a significant portion of the discharge period. When the capacitor voltage (V_C) is equal to V_G, the energy remaining in the circuit is contained in the capacitor (= $0.5 \, C \, V_G^2$) and the inductor (= $0.5 \, LI_{Pk}^2$), where I_{Pk} is the peak circuit current. The difference between this energy and the initial energy on C is the energy deposited into the discharge up to this time. For the remainder of the positive current cycle, the discharge becomes current-fed, i.e., the gap potential is maintained by the inductor and the decreasing circuit current.

In order to prevent a reversal of circuit current, the total energy in the circuit when V_C is equal to V_G must be deposited in the gap during the remaining portion of the PFN positive-cycle oscillation. That is,

$$0.5 \, C \, V_G^2 + 0.5 \, L \, I_{Pk}^2 \leq \int_{t_1}^{t_2} V_{Gap} \, I \, dt \qquad (18)$$

46

where t_1 represents the time at which $V_C = V_G$ and t_2 the time at which $I = 0$. Due to the nonlinear dependencies of V_{Gap} and I, Eq. (18) cannot be evaluated analytically. However, an upper limit on the deposited energy can be set by assuming that V_{Gap} is equal to V_G from t_1 to t_2. Then I is sinusoidal and Eq. (18) becomes

$$I_{Pk} \leq \frac{2V_G}{\omega L} \tag{19}$$

where ω is the circuit angular frequency.

The operation of the circuit prior to t_1 cannot be readily described analytically due to the complexities of the break-down kinetics. However, if one assumes that the gap potential approaches V_G very rapidly, then V_G can be approximated as simply a voltage sink in an LC circuit, where $I_{Pk} = V_0/\omega L$. Equation (19) then becomes

$$V_0 \leq 2V_G \tag{20}$$

That is, inefficient energy transfer and resultant circuit ringing will occur whenever the initial capacitor voltage is greater than twice the kinetics-determined glow voltage.

This result should be modified slightly since the gap potential will be quite high at discharge initiation and will be slightly larger than V_G prior to t_1. This may be especially significant in a very short-pulse circuit. However, circuit modeling with the kinetics code incorporated revealed that ringing can be expected when $V_0 \gtrsim 2.5\ V_G$.

This point confirms the previously mentioned lack of validity of conventional impedance-matching techniques. Changing the values of C or L will merely alter the duration of the energy-transfer cycle and the peak current but will not effect a more efficient power deposition into the discharge. It should be pointed out that a discharge exhibiting decreasing glow voltage--such as NF donor discharges[23]--will require an even lower initial charge on C since less energy will be deposited during the $t_1 - t_2$ period.

47

Only an increasing voltage-with-time characteristic will allow a large initial capacitor voltage.

Assuming that the switch/discharge interaction is not severe, the simple switched-capacitor circuit will yield a fast voltage risetime. The importance of overvoltage rate-of-rise appears to be a function of pre-ionization[24] but for most practical discharge configurations, a risetime of $\sim$ 30 nsec. to full overvoltage is generally attainable with the simple circuit. Somewhat obvious, however, is the limitation of current risetime of this circuit configuration imposed by the series inductance.

The popular, and often successful, variation of the switched-capacitor circuit involves the addition of a low-inductance capacitive leg in parallel with the gap, as shown in Fig. 23. The inductances shown here represent the component stray inductances. The variable resistor R_S represents the switch as presently modeled, as well as the main circuit-arm stray resistance. The purpose of the additional capacitor (C_p) is to provide energy to the discharge gap very rapidly during breakdown.
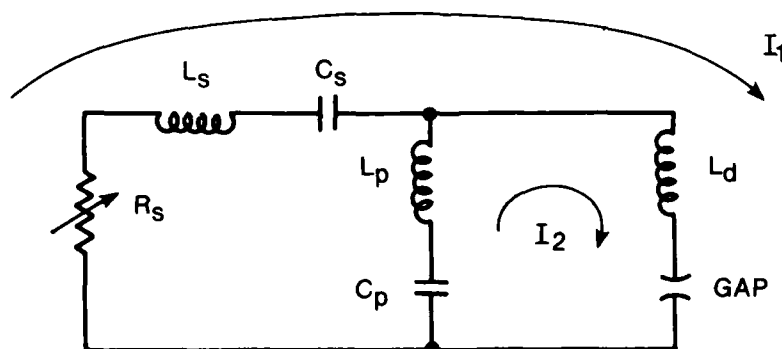
Figure 23. Equivalent Circuit of Capacitive-Transfer Discharge Circuit.

In one mode of operation, C_p need only supply energy in the early stages of a discharge, until the main circuit current can rise to a useful value. The energy stored in C_p, then, need not be large. Therefore, the physical size

may be relatively small, and a low stray inductance could be achieved. The result is a much-reduced rate-of-rise of the gap current followed by the transfer of energy from the main circuit leg. This circuit configuration will be referred to as an "RLC circuit with peaking capacitor."

A second mode of operation of the circuit of Fig. 23 is the complete transfer of energy from C_S to the low-inductance C_p before gap breakdown, resulting in a series capacitor-discharge circuit exhibiting low total inductance. Several difficulties, however, arise in applying this technique. First, 100% of the energy in C_S must have been transferred to C_p before the onset of significant discharge current. This can be achieved only if C_S is equal to C_p. Since L_p is significantly smaller than L_S, the voltage rise appearing on the pre-breakdown gap will be approximately the same as the voltage rise of C_p. A time of 30 nsec. was mentioned earlier as being an optimal maximum risetime for a reasonable gap overvoltage, although it will be shown later that $\leq$ 50 nsec. is acceptable. The transfer of energy to C_p, then, must be accomplished within $\sim$ 50 nsec. which greatly limits the range of usable capacitor values. Obviously, the larger the inductance of the main storage arm, the smaller the maximum value of C_S and C_p. In addition, for this circuit to offer an advantage over a simple switched-capacitor circuit, $(L_p + L_D)$ must be significantly less than L_S. The time required for energy deposition into the discharge, therefore, will be less than the voltage risetime. In other words, this mode is only applicable to short-pulse lasers.

Secondly, the argument presented earlier in discussing energy-transfer efficiency in a series LC circuit is also applicable here. That is, ineffi-cient transfer and resultant circuit ringing will occur when an overvoltage of 2 - 2.5 times the kinetics-determined glow voltage is present on C_p. Although a moderate amount of inefficiency and ringing may be tolerable in an operational laser system, the range of both the voltage and the capacitor values is limited. Therefore, a somewhat limited energy range exists over which the capacitor-transfer mode is applicable.

The first mode of operation--the peaking mode--is more applicable to medium-power XeCl lasers. At the time of gap breakdown, energy is still present in

the main inductive circuit; therefore, the deposition time may be significantly longer than if only the low-inductance arm were feeding the discharge. However, energy during the initial current risetime will be suppled by the fast, low-inductance circuit. Selection of components, however, becomes much more complex since the gap and circuit interact strongly, even before gap breakdown.

Ideal circuit operation would be as follows: Consistent with the earlier discussion on allowable charge on a switched capacitor, initial voltage is $\leq 2.5 \times V_G$. Upon closure of the thyratron switch, C_p begins charging and a rising voltage appears on the gap. With the proper gap parameters, breakdown occurs before the capacitor-energy transfer cycle is complete; therefore, forward current exists in L_S. As the gap potential decreases, both the main circuit and the peaking arm transfer energy to the discharge. The current through L_S increases, although at a much lower rate than the current through L_p. A current peak occurs as the voltage on C_p approaches V_G. This capacitor voltage decreases below V_G, causing a decreasing current. Assuming that the voltage on C_p was $\sim 3\text{-}4 \times V_G$ at breakdown, the voltage on C_p would be expected to reverse. If, however, the energy delivery rate of the main circuit arm is sufficient, the reversal will not be seen by the gap; only a current dip will occur. Some current oscillation due to the peaking arm will continue to be seen, but the remainder of the positive cycle will be primarily controlled by the slower main circuit arm. As the voltage on C_S drops below V_G, gap current decreases. Hopefully, all electrical energy will have been transferred to the gap when the current reaches zero.

This idealized sequence of events cannot generally be achieved in practice because of the complex relationship between circuit and discharge parameters. However, one can optimize for a desired characteristic and minimize the unwanted results by careful design. For example, a fast current rise and long pulse can be achieved at the sacrifice of energy-transfer efficiency. Also, higher peak currents may exist in the gap than in the switch, allowing the gap current to exceed the switch rating without causing damage.

Because the XeCl laser operates best with a very fast buildup of charge and therefore, requires a fast current risetime and because energy can normally be deposited into the discharge over a time period of 100 nsec. or more, the RLC circuit with peaking capacitor will generally operate satisfactorily over a moderate range of energies. Systems operating in the 0.5 - 10 J/pulse range will adequately perform with this type of PFN. For this reason, the laser built under this program utilized this circuit. The circuit is relatively easy to construct, and laser performance is not extremely sensitive to changes in parameters.

Optimization of the circuit, however, is not clear-cut. The circuit is basically a combination of two parallel RLC circuits in parallel with a gap. Even if the gap is treated as a voltage sink in modeling, the solution of the circuit equation is not a simple analytical expression. In addition, the values of current and voltage existing in the circuit components at the time of discharge breakdown are important in determining the operation for the remainder of the cycle. These values are dependent upon the breakdown delay.

Figure 24 demonstrates the variation of initial conditions existing at gap breakdown as functions of gap parameters. For these calculations, preionization was assumed to be a uniform distribution of an electron density of 10^8 cm^{-3}. Ionization rates were approximated by a polynomial fit to the data presented previously. Overvoltage is defined as the difference between the electrical potential of C_p and V_G at the time when electron density has grown by 10^5. As discussed above, this overvoltage aids in determining the current risetime.

The formation of guidelines for use in the design of this PFN, however, can be costly if a comprehensive code such as SCEPTRE is used; many individual computer runs must be made in order to find trends in the various parameters affecting the PFN-discharge interaction. For this reason, two analytical approximations of the circuit have been developed for use with a desk-top calculator where the effects of component value changes can be seen quickly. The detailed model need not be used in the trend search but rather for relatively accurate final values.

51
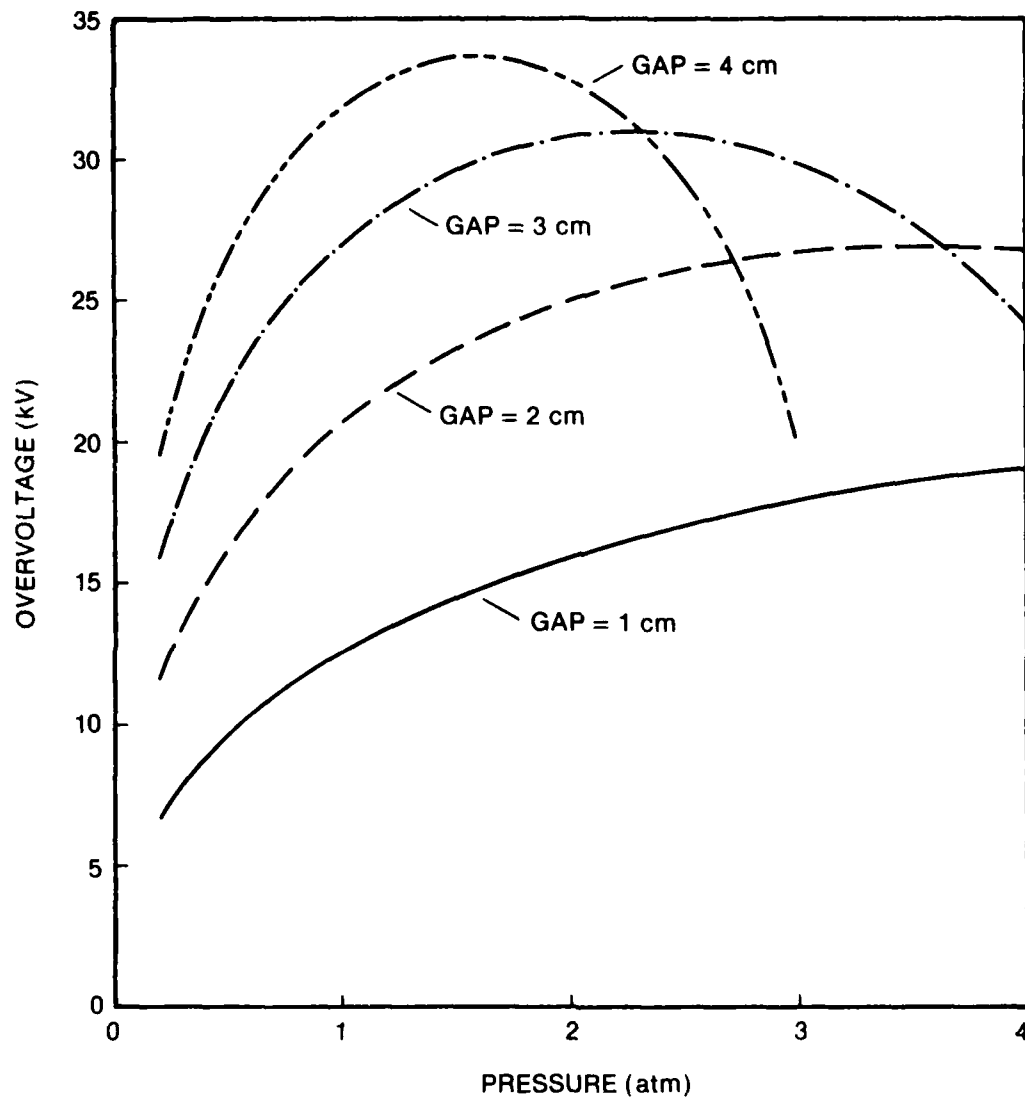
Figure 24. Effect of Gas Pressure and Gap Spacing upon Breakdown
Overvoltage of Capacitor Discharge Circuit with Peaking
Capacitor. Component Values: Switch circuit series
inductance = 150 nH, energy-storage capacitor = 10 nF,
peaking capacitor = 7.5 nF, initial voltage on energy-
storage capacitor = 50 kV.

52

The choice of which model is to be used is made by a tradeoff of accuracy and computation time. The first-approximation model to be discussed here treats the discharge as a voltage source equal to the V_G value determined from a kinetics model or from empirical results. Computation time is short ($\sim$ 10 sec. on an HP 9845), but only general trends can be relied upon. The second approach utilizes an analytical relationship for the gap voltage determined from the ionization/attachment characteristics (again in the steady-state) as well as the electron-drift-velocity characteristics.

Before proceeding with an individual model, the circuit initial conditions must be considered. If one closes a switch on a charged transmission line, the voltage on the gap at the time of breakdown will be approximately the value of the charged line. The switch characteristics need be considered only after significant current flows. However, if energy is being transferred between lumped components, as in the RLC circuit with peaking capacitor, the breakdown characteristics of the gas must be considered in determining the amount of energy in each reactive component at the time when significant current begins to flow through the gap.

Before breakdown, the circuit of Fig. 23 is an elementary series RLC circuit. The voltage seen by the open gap is that which appears across the series combination of C_p and L_p. Analytically, this is expressed as

$$
V_d = V_o \exp\left(-\frac{R}{2L_T} t\right) \left[\frac{C_T}{C_p} \left(\frac{R}{2\omega L_T} \sin \omega t + \cos \omega t - 1\right)\right.
$$
$$
\left. + \frac{L_p}{L_T} \left(\frac{R}{2\omega L_T} \sin \omega t - \cos \omega t\right)\right]
$$

(28)

where V_o is the initial voltage on C_S; R is the total effective series resistance (including the switch); L_T is the series inductance composed of L_S and L_p; C_T is the series capacitance composed of C_S and C_p; and

$$
\omega^2 = \frac{1}{L_T C_T} - \left(\frac{R}{2L_T}\right)^2
$$

(29)

53

For typical component and risetime values, $R/2\omega L \ll 1$ and $\exp\left(-\frac{R}{2L}\,t\right)$ > 0.95; therefore, Eq. (28) can be simplified to

$$V_D = V_o \left[\left(\frac{C_T}{C_P} - \frac{L_P}{L_T}\right) \cos \omega t - \frac{C_T}{C_P}\right] \qquad (30)$$

To estimate the time between switch closure and discharge breakdown, the electron density (n) must be determined as a function of time. Since both recombination and attachment are insignificant during this time period, the electron-continuity equation can be reduced to

$$dn/dt = K_I Nn \qquad (31)$$

where K_I is the mixture-weighted E/N-dependent ionization rate and N is the gas-neutral number density. For the E/N range of interest, $K_I N$ can be approximated by a second-order polynomial in E/N. For a given number density and gap distance, then,

$$K_I N = a_2\, V_D^2 + a_1\, V_D + a_0 \qquad (32)$$

When Eqs. (31) and (32) are combined, the percentage change in electron number density is

$$dn/n = (a_2\, V_D^2 + a_1\, V_D + a_0)\, dt \qquad (33)$$

When Eqs. (28) and (33) are combined and integrated, the result is

$$\ln n/n_o = \left(\frac{a_2 V_o^2 A^2}{2\omega} \cos \omega t - \frac{2a_2 V_o^2 AB}{\omega} + \frac{a_1 V_o A}{\omega}\right) \sin \omega t$$

$$+ \left[a_2 V_o^2 \left(\frac{A^2}{2} + B^2\right) - a_1 V_o B + a_0\right] t \qquad (34)$$

where

54

$$A = \frac{C_T}{C_P} - \frac{L_P}{L_T}$$

$$B = \frac{C_T}{C_P}$$

The values of a_0, a_1, and a_2 can be calculated by means of a polynominal least-squares fit of the ionization-rate coefficients obtained from a Boltzmann analysis. By defining breakdown as $n \approx 10^{13}$ cm^{-3}, the breakdown time--and, hence, the initial circuit conditions--can be quickly computed using a desk-top computer.

Recognizing the fact that after breakdown the current will increase until the ionization and attachment processes occur at the same rate, the circuit performance can be approximated by treating the discharge gap as a voltage source (or voltage sink). The value of this source would correspond to the gap potential at which the electron-source-rate coefficient (K_I) is equal to the electron-loss-rate coefficient (K_A). For all but very fast current rise times, this potential (glow-phase E/N) can be calculated from Boltzmann analyses data. This method is, of course, valid only for positive-discharge current flow and will tend to overstate the peak current since, in reality, the gap voltage decreases only to this quasi-steady-state value when the peak current is reached. Nevertheless, the peak current can be predicted to within $\sim$ 20% of the value predicted by a detailed discharge model, and the discharge-current waveshape as well as the voltage and current waveshapes of the circuit components are reasonably approximated by this simple model. This method is of particular value in estimating the initial circuit conditions which would result in the minimum of the discharge-current oscillations remaining above zero.

The circuit equations describing this simple model are (see Fig. 23):

$$L_S \ddot{I}_1 + L_D (\ddot{I}_1 + \ddot{I}_2) + \frac{1}{C_S} I_1 = 0 \tag{35}$$

55

and

$$L_P \ddot{I}_2 + L_D (\ddot{I}_1 + \ddot{I}_2) + \frac{1}{C_P} I_2 = 0 \tag{36}$$

where the overhead dots denote derivatives with respect to time. Note that all resistances, including R_S, are being ignored. Using Laplace transforms, the simultaneous solutions of Eqs. (35) and (36) for I_1 and I_2 are long algebraic expressions. However, if

$$2C_P C_S L_D^2 \ll [C_S (L_S + L_D) - C_P (L_P + L_D)]^2 \tag{37}$$

then the solutions can be put into a manageable form.

This condition generally holds for reasonable component values consistent with rare-gas-halide discharges; therefore, the currents in the simple model are

$$I_i = \frac{1}{\omega_2^2 - \omega_1^2} [(A_{i3} - A_{i1} \omega_1^2) \cos \omega_1 t + (A_{i2} \omega_1 + \frac{A_{i4}}{\omega_1}) \sin \omega_1 t$$

$$+ (A_{i1} \omega_2^2 - A_{i3}) \cos \omega_2 t + (A_{i2} \omega_2 - \frac{A_{i4}}{\omega_2}) \sin \omega_2 t] \tag{38}$$

where

$$A_{11} = I_0$$

$$A_{12} = \frac{-(L_P + L_D) V_S + L_D V_P - L_P V_D}{(L_P + L_D) L_S + L_D L_P}$$

$$A_{13} = \frac{L_S I_0}{C_P[(L_P + L_D) L_S + L_D L_P]}$$

56

$$A_{14} = -\frac{V_D + V_S}{C_P[(L_P + L_D)\, L_S + L_D L_P]}$$

$$A_{21} = -I_0$$

$$A_{22} = \frac{-\,(L_S + L_D)\, V_P + L_D V_S - L_S V_D}{(L_P + L_D)\, L_S + L_D L_P}$$

$$A_{23} = -\frac{L_P I_0}{C_S[(L_P + L_D)\, L_S + L_D L_P]}$$

$$A_{24} = -\frac{V_D + V_P}{C_S[(L_P + L_D)\, L_S + L_D L_P]}$$

$$\omega_1 = \frac{1}{C_S(L_S + L_D)}$$

$$\omega_2 = \frac{1}{C_P\left(L_P + \dfrac{L_D L_S}{L_D + L_S}\right)}$$

where I_0 is the initial current in the storage-capacitor branch (I_1) at breakdown $(t = 0)$, and V_S and V_P are the voltages of C_S and C_P, respectively, at breakdown.

Although calculation of the circuit characteristics using Eq. (38) may seem tedious, a desk-top programmable calculator can perform the computation in a relatively short period of time. Consequently, this method can be used to show approximate circuit characteristics as component values and initial energy in C_S are varied.

The accuracy of the circuit model could be increased if a better description of gap voltage were used. The equations describing the circuit then would be

$$L_S \ddot{I}_1 + L_D (\ddot{I}_1 + \ddot{I}_2) + \frac{1}{C_S} I_1 + \dot{V}_D = 0 \qquad (39)$$

57

$$L_P \ddot{I}_2 + L_D (\ddot{I}_1 + \ddot{I}_2) + \frac{1}{C_P} I_1 + \dot{V}_D = 0 \qquad (40)$$

A simple expression for the gap voltage can be derived from Eq. (8). Differentiation of this expression results in

$$\dot{I}_D = eA(v \frac{dn}{dt} + n \frac{dt}{dv}) \qquad (41)$$

The change in the electron density can be written as

$$\frac{dn}{dt} = (K_I - K_A) Nn \qquad (42)$$

where $K_I - K_A$ is dependent upon the gap voltage. Assuming a quasi-steady-state condition, $(K_I - K_A)N$ can be tabulated from Boltzmann analyses.

The last term in Eq. (41) presents some difficulty in simplification. When a rare gas exhibiting a Ramsauer minimum is mixed with a molecular species having a large inelastic electron-collision cross section in the vicinity of the Ramsauer minimum, the functional dependence of electron drift velocity upon E/N becomes difficult to describe in an analytical expression. However, for much of the E/N range of interest, a fairly linear relationship holds. That is,

$$\frac{dv}{dt} = \frac{dv}{dV} \frac{dV}{dt} \approx \frac{v}{V} \frac{dV}{dt} \qquad (43)$$

This relationship, then, can serve as a "suitable approximation."

If Eqs. (41) - (43) are combined, the time rate of change of the gap voltage can be described by

$$\dot{V}_D = V_D [\frac{\ddot{I}_1 + \ddot{I}_2}{\dot{I}_1 + \dot{I}_2} - (K_I - K_A)] \qquad (44)$$

Solving Eqs. (39), (40), and (44) numerically and using a "look-up table" for values of $(K_I - K_A)$, the circuit characteristics can be approximated to

58

a higher degree of accuracy than is possible for the simple analytical model. However, computation time is much longer due to the requirement of a very small integration-step size. Nevertheless, the full current/voltage waveshape can be handled with this numerical routine, regardless of the polarity of the discharge current.

Up to now, the circuit analyses have been based upon the single thyratron-switched, capacitive-transfer circuit of Fig. 23. The effect of multiple circuits connected in parallel with the discharge is also of interest since the laboratory system has two parallel circuits. For the case where m identical circuits are connected at the discharge, the equations describing the ith circuit are

$$L_S \ddot{I}_{i1} + mL_D (\ddot{I}_{i1} + \ddot{I}_{i2}) + R_S \ddot{I}_{i1} + \frac{1}{C_S} I_{i1} + \dot{V}_D = 0 \qquad (45)$$

$$L_P \ddot{I}_{i2} + mL_D (\ddot{I}_{i1} + \ddot{I}_{i2}) + R_P \ddot{I}_{i2} + \frac{1}{C_P} I_{i2} + \dot{V}_D = 0 \qquad (46)$$

where R_P is the effective series resistance of the C_P leg. These equations show that for the simple analytical model, only the value of L_D need be adjusted in order to account for the additional circuits. For the more complex model, the "first approximation" to V_D is unaffected. Of course, total discharge current (I_D) would be

$$I_D = \sum_{i=1}^{m} (I_{i1} + I_{i2}) \qquad (47)$$

It is, therefore, relatively simple to account for _identical_ parallel circuits.

The RLC circuit with peaking capacitor was the lumped-element PFN arrangement emphasized in the current study. Another often-used configuration of switched capacitors is the LC inversion circuit shown in Fig. 25. This circuit has two main characteristics: (1) a high overvoltage can be attained through a reversal of potential on C_1 as long as the gap delays break down

59
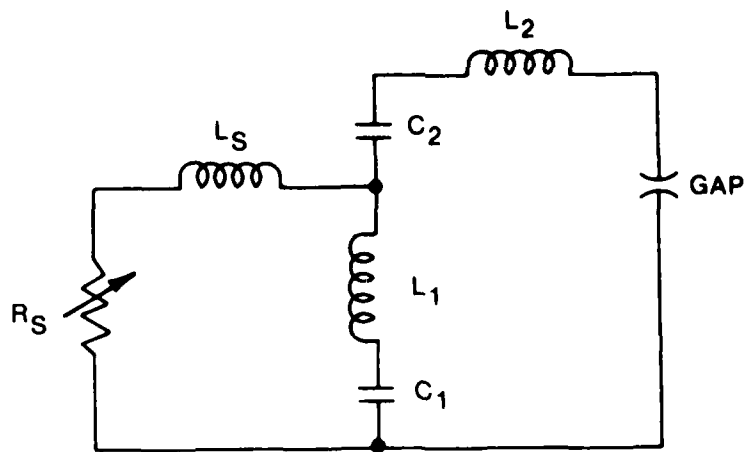
Figure 25. Electrical Schematic of Basic LC Inversion
Circuit.

for a sufficient period of time, and (2) the discharge current bypasses the switch. As discussed previously, for gas mixtures exhibiting a rapidly forming gap glow potential, a high overvoltage results in inefficient energy transfer and in excessive ringing. The first characteristic is, therefore, of no advantage in rare-gas-halide laser operation.

The second characteristic is of great advantage in operation of high-rep-rate systems because of the typically high switch inductance. However, closer inspection of the pulse cycle time reveals a pulse width, and resulting maximum-energy-transfer, limitation. Since, as discussed previously, the voltage rise on a suitably preionized gap must be $\leq$ 50 nsec., the value of C_1 must be sufficiently small to effect this half-cycle time in the switched circuit comprised of C_1, L_1, L_s, and R_s. Upon gap breakdown, discharge current flows through the series circuit of C_1, C_2, L_1, L_2, and the gap. For the most efficient transfer, $C_1 \simeq C_2$; also, by definition, $(L_1 + L_2) \ll L_s$. This means that the cycle time of the discharge circuit is less than the voltage risetime, i.e., the LC inversion arrangement is only applicable to short-time-duration discharge pulses. In addition, the switch arm cannot contribute to discharge current--as in the peaking-capacitor arrangement--since current flows in the opposite direction.

In other words, the LC inversion circuit is not suitable for use with rare-gas-halide lasers except, possibly, in short-pulse low-energy systems. The addition of a peaking capacitor in parallel with the gap will enhance the operation of the circuit and increase the quantity of energy transferred in a cycle. However, operation would still be characterized by a short time duration and by excessive ringing.

Lumped-element pulse-forming networks suffer from two main disadvantages: (1) a sinusoidal current waveform and (2) limited energy-transfer efficiency. For long pulse lengths ($\gtrsim$ 50 nsec.) especially, little useful energy is deposited in the slowly rising and falling edges of the current waveform. In addition, the possibility of arcing, especially in the attachment-dominated trailing edge, is increased as pulse lengths are extended. Also, as explained in the beginning of this discussion, an overvoltage of $\gtrsim$ 2.5 V_G

cannot be efficiently utilized. Much work in designing an RLC-with-peaking-capacitor arrangement resulted in a maximum theoretical efficiency of $\sim$ 65% when an overvoltage of $\sim$ 2 × V_G (3 × V_G total) was used. Due to the large currents which are characteristic of medium- and high-power lasers, no successful technique of removing the excess energy before reversal was found.

The use of a high-voltage prepulse--or "poker" pulse--is one technique previously used with CO_2 laser discharges[25] and recently applied to a rare-gas-halide system.[26] By use of a separate circuit to provide the required initial overvoltage, the main energy-storage capacitor voltage can be decreased to a more optimum level. Figure 26 shows a basic application of this technique. Here, the poker-pulse circuit arm consisting of C_p, L_p, and R_p doubles as a peaking circuit since, theoretically, the value of C_p can be sufficiently small that the current risetime is acceptably short. An additional peaking arm at the gap may also be used if necessary.
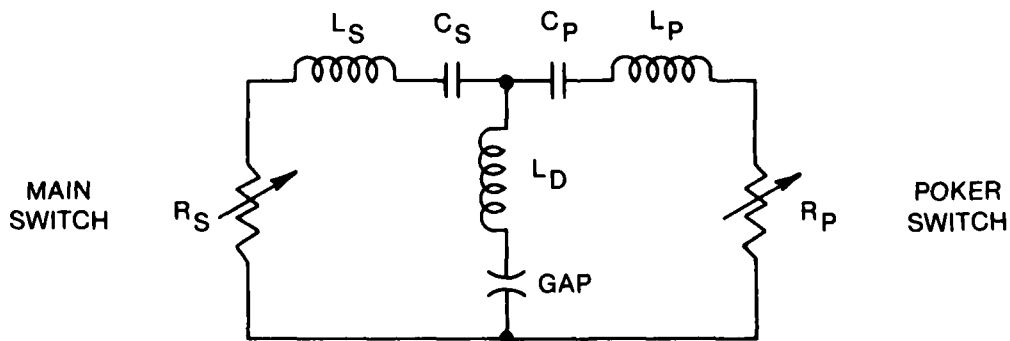
Figure 26. Basic RLC Circuit with Parallel Prepulse ("Poker") Circuit.

For this circuit arrangement to be effective, the main circuit arm must present a high impedance to the poker arm. This can be accomplished with either a high main circuit inductance or a switch, as represented in Fig. 26 by variable resistor R_S. The use of a moderate inductance in place of R_S requires that C_1 be charged rapidly--a difficult design problem--in order to prevent a low-voltage arc in the gap. In addition, the previously discussed

62

disadvantages of slow current-rise and -fall times will be present. The use of a switch poses two problems: (1) the thyratron (required by the high rep-rate) will have a reverse bias during the gap overvoltage phase and (2) since no initial current is flowing in the main circuit, the current rise-time will be excessive as a result of high thyratron switch inductance. The first point does not create an impossible situation, but thyratron timing difficulties make this arrangement somewhat impractical. The detrimental effect of the thyratron inductance, however, is insurmountable, especially considering the inevitable serious ringing of the poker circuit which results from the high overvoltage.

Other methods of applying the poker pulse have been studied, but the limitation of inductive elements in the main supply circuit is always present. The poker technique is more applicable and will be discussed further in conjunction with constant-impedance PFN's.

As the laser output pulse length is extended beyond $\sim$ 50 nsec, the lumped-element PFN becomes less attractive. The peaking-capacitor arrangement required for fast current risetime produces ringing of the laser output. Since the current is decreasing for $\sim$ 50% of the laser-excitation cycle, attachment-induced instabilities become more likely. The oscillating current waveform from the peaking arm will cause a reversal of current before the main-circuit arm current reaches zero. This can generally be expected to induce discharge arcing before the PFN energy has been transferred to the gap. For long pulse lengths, then, the lumped-element PFN is generally not suitable.

Constant-Impedance PFN

Modeling and laboratory experience have shown that the ideal PFN will provide a relatively fast voltage rise ($\leq$ 50 nsec. to reach $\geq 3 \times V_G$) and a very fast current rise ($\leq$ 30 nsec. for creation of an electron density $\geq 5 \times 10^{14}$ cm^{-3}). Also, power may be deposited over a period exceeding 100 nsec.; however, for most of this time period, a relatively constant E/N will exist. After breakdown, the ideal PFN should provide a generally large, but relatively constant, current to the constant voltage gap. That is, a

constant-impedance PFN is much more suitable for efficient operation than a lumped-element arrangement. The constant-current requirement is especially true for operation near the maximum power-deposition level. In this case, one wishes to attain the largest possible electron density for the longest possible time, without entering the realm of significant electron-induced losses.

Figure 27 shows the most basic switched configuration of a transmission-line (constant-impedance) PFN. Initially, the line of impedance Z is charged to V_0 in such a way that the full potential is isolated from the gap by the switch represented by variable resistor R_S. Upon switch closure, voltage appears on the gap at a rate-of-rise determined by the switch closure. As in the case of the simple capacitor-switched circuit, full conduction of a thyratron switch may be affected by the gap-breakdown delay; but, as was true for the capacitor PFN, the stray switch inductance will dominate circuit operation. A thyratron is again required in order to meet the high-repetition-rate requirements.
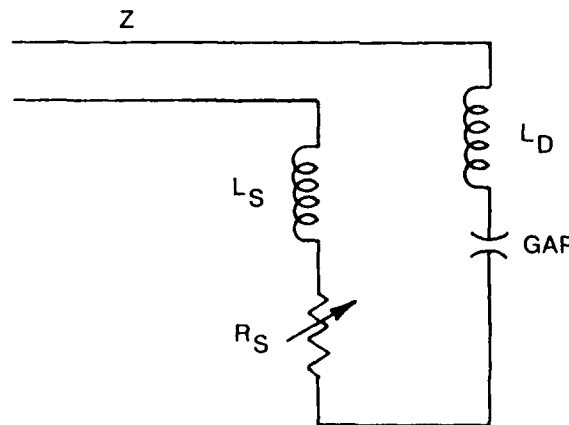
Figure 27. Electrical Schematic of Simple Switched-Transmission-Line PFN.

Assuming that the transmission line two-way transit time is long compared to switch-closure and gap-breakdown times, the line is effectively a resistive voltage source in the circuit. Consistent with previous model simplifications, a best-case estimate of the minimum current risetime can be achieved by treating the gap as a constant voltage source. The circuit then becomes a simple series combination of resistances, inductances, and voltage sources.

64

The small capacitance of the gap can be ignored. The circuit current (I) is then expressed as

$$I = \frac{V_0 - V_G}{R_S + Z} \left[(1 - \exp \left(\frac{R_S + Z}{L_S + L_D} t \right)) \right]$$ (48)

where V_0 is the initial charge on the line and V_G is the kinetics-determined gap glow potential. This simplification also assumes that the line is lossless--a valid approximation for the best-case analysis.

The dominant contribution to the stray circuit inductance is made by the tyratron. A parallel arrangement of thyratron switches is not practical in the simple circuit of Fig. 27 because of the detrimental interaction which is common to parallel operation of any gas-discharge device. Minimum circuit inductance in a practical circuit is, generally, $\sim$ 50 - 150 nH. If a large line impedance is present, a very rapid current risetime can be achieved. However, as will be shown shortly, line impedances of 0.1 - 1.5 Ω are required of medium- and high-power laser systems. For a 100-nH stray inductance, the e-fold risetime given by (48) will be 100 nsec if $R_S + Z = 1 \Omega$. This unacceptably long risetime makes the switched circuit of Fig. 27 inappropriate for high-rep-rate operation.

Before considering other, more appropriate PFN configurations, the simple circuit can be used to determine the required line impedance and charge voltage. If the stray inductance can be made small, the limiting circuit current can be reached very quickly. This current level is determined by the total circuit effective impedance ($= R_S + Z$) and the difference between the line charge potential and the gap glow voltage.

According to transmission-line theory, the maximum power transfer (zero reflection) will occur when the product of the output-line current and line impedance is equal to the output voltage. For a resistive load, this occurs when the load impedance is equal to the line impedance. For a constant-voltage load, however, the line current is determined by the total-circuit effective impedance ($= R_S + Z$) and the difference between the line-charge potential and the gap glow voltage. In this case, the voltage reflected

65

back into the line is the load voltage minus the effective line drop (line current × Z). That is, once the discharge reaches its "glow" phase, efficient transfer of electrical energy occurs only when the line is charged to twice the glow voltage, regardless of the line impedance.

The charge voltage, then, is a function of the discharge kinetics. In an optimal circuit, the impedance of the line is the only circuit variable useful for adjustment of the discharge current. For example, for a line impedance of 1 Ω, if the glow voltage is 10 kV and the line is charged to 20 kV, the discharge current will be 10 kA and no line reflection will occur. The current can be doubled by using one-half the line impedance, again attaining 100% energy transfer during the line discharge time (= twice the line-length time). Currents typical of medium-power lasers exceed 5 kA, and glow voltages are generally < 10 kV. Therefore, required line impedances are generally < 2 Ω. High-power laser systems generally require impedances of 0.1 - 0.5 Ω.

Unfortunately, the efficiency requirement only allows for a factor-of-two *overvoltage at discharge initiation*. If a higher voltage is used, less-efficient transfer will occur and the reflected energy must be removed before subsequent reflection causes this energy to effect discharge instabilities. For example, for a 30-kV charge on a 2-Ω line and a 10-kV glow voltage, 10 kA will flow through the discharge and $\sim$ 11% of the original line energy will be reflected back into the line and appear as a -10 kV reflection at the open end. In other words, the requirements for initiating a discharge are not compatible with the sustaining characteristics of a line-fed system.

As discussed previously, if an inductive switch is used to isolate the gap from the line, some power will be reflected whenever the current is rising or falling, resulting in a decrease in efficiency. The reason for this is that the line sees an inductive voltage source. In addition, the current risetime will decrease, resulting in a lower rate of build-up of the upper laser level and a potential loss of optical energy to spontaneous emission.

66

This situation can be improved by using two matched lines in series, isolated by a switch as shown in Fig. 28. The first line (Z_1) is charged to the desired voltage. Upon switch closure, efficient energy transfer to the second line (Z_2) occurs, except on the leading and trailing edges. The discharge gap sees a somewhat-reduced voltage rate-of-rise; however, assuming a reasonable level of preionization, instabilities are not likely to be a problem if the risetime is less than $\sim$ 30 nsec. The voltage wave at the gap will initially be reflected. As breakdown occurs, a very fast current rate-of-rise will be obtained. In other words, this technique sacrifices voltage risetime for an improved current risetime--a generally acceptable trade-off. The reflections on the leading edge of the wave will show up on the trailing edge, aided by the switch inductance. The result would be a relatively efficient energy transfer if the required initial overvoltage were twice the glow voltage (V_G).
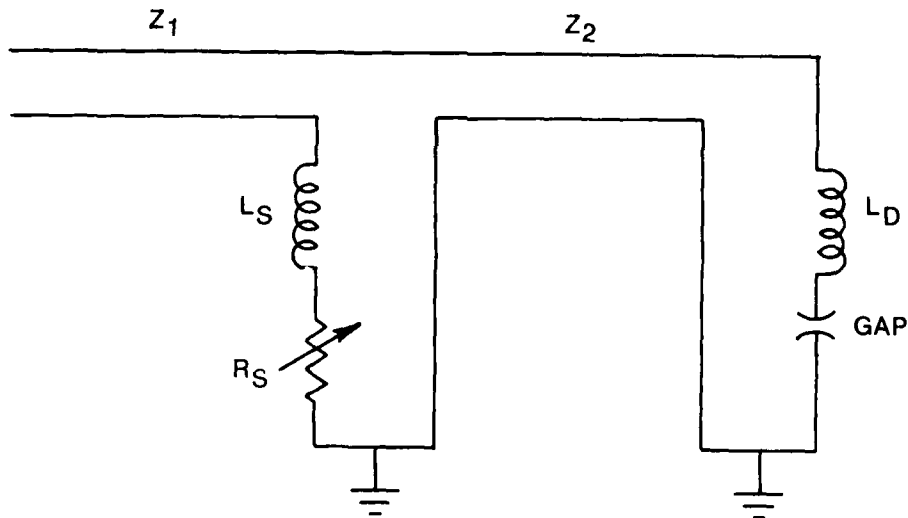
Figure 28. Electrical Schematic of Pulse-Charged Transmission-Line PFN.

Unfortunately, overvoltages of 2-3.5 × V_G (total charge voltage of 3-4.5 × V_G) are reportedly[20a] required for proper discharge initiation. If the switch were to act as a diode, the line could be charged to much greater voltage than 2 V_G. In this case, the negative cable reflection would return to the original charged line and remain there. However, hydrogen thyratrons require deionization times much greater than the 50 - 150 nsec line travel

times utilized in XeCl lasers. Several methods of trapping the excess energy were evaluated without success. The most promising technique was the use of a well-coupled, low-inductance, stacked, pie-wound transformer; but more development is needed before the stringent voltage and current requirements can be met by these devices.

One of the most popular arrangements of constant-impedance line PFN's is the Blumlein, shown in Fig. 29(b). This is a special case of the more general category of Darlington networks[27] shown in Fig. 29(a). The advantage of the N-section Darlington is the achievement of voltage gain of $(N + 1)/2$ along with a very efficient transfer of energy as long as $Z_i = \sum_{j=1}^{i} j\, Z_1$. Another advantage would appear to be that the switch is removed from the output and, for multiple stages, operates at reduced voltages. Unfortunately, it will also operate into a lower impedance load, resulting in higher currents and a decrease of voltage risetime if stray inductance is present.

The Blumlein does offer the advantage of removing the switch from the output, resulting in a much-improved discharge-current risetime, while degrading only the discharge voltage rate-of-rise. Since the lines are effectively series-connected with the gap in Fig. 29(b), the line impedance is one-half of that required for the switched line discussed previously (Fig. 28). For a sufficiently low switch inductance, a voltage risetime within the 50-nsec range can be achieved. However, the energy in the leading edge of the electrical wave arriving at the gap will be reflected back into the switched line until breakdown occurs. Consequently, some inefficiency is inherent in this arrangement. Modeling has shown that better circuit operation can be achieved through mismatching of the two lines, but at the expense of energy-transfer efficiency. An additional loss of efficiency is introduced by the voltage mismatch required for overvolted initiation, as discussed earlier.

The Blumlein was mentioned here because of the success reported by others. In moderate- and high-power-level, high-rep-rate applications, however, the large inductance of the thyratron switch prohibits its use. For example, for a 10-kA discharge exhibiting a 10-kV glow voltage, a line impedance of $1 \, \Omega$ is required for the optimal voltage-matching conditions ($V_0 = 10$ kV).

68

(a)

(b)
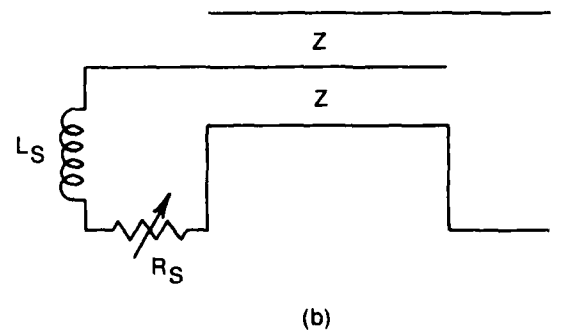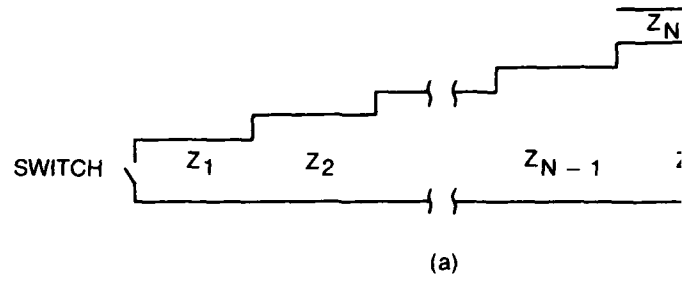
Figure 29. Schematic Diagram of Transmission-Line
Networks. (a) General N-Section Arran
(b) Practical One-Section Blumlein Dis
Configuration.

69

An e-fold voltage risetime of 50 nsec would exist for a switch inductance of 50 nH; 150 nsec is required to reach 95% of full voltage. If a larger overvoltage is used, a faster risetime will result. However, an overvoltage of 5 - 7 × V_G would be required in a circuit providing an acceptable voltage risetime with a switch inductance of 50 nH; energy efficiency and post-discharge ringing would be prohibitive.

A number of alternate circuit configurations were studied with the SCEPTRE computer code, utilizing a lossless transmission-line model. The ballast arrangement of Fig. 30 appeared promising for high overvoltage situations since the uncharged line of impedance Z_2 initially stores some of the energy delived by the charged line of impedance Z_1 and returns this as useful energy after reflection from the shorted end. This method would also require line lengths of only one-half of the desired pulse length. However, analysis of circuit operation showed that 100%-efficient energy transfer to the discharge could only be achieved for a total charge voltage of 2 V_G. This arrangement is a good candidate if high efficiency is not required.
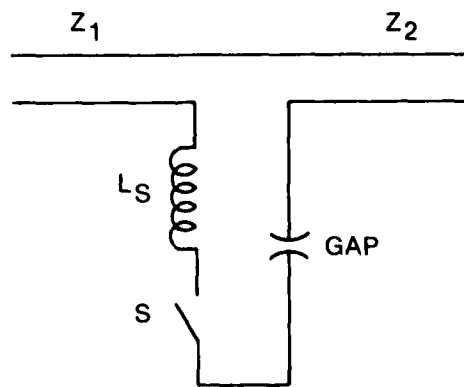
Figure 30. Schematic Diagram of Transmission-Line Ballast PFN.

Various techniques of construction of compact constant-impedance lines are of interest. Parallel arrangement of coaxial cables is a simple method of producing a transmission line, but this is physically very bulky, especially for long pulse lengths. A ribbon-stacked transmission line is more compact but also somewhat bulky and often susceptible to detrimental edge-corona

70

effects. Lumped-element Guillemin networks[28] would appear to be a viable alternate. Figure 31 shows two such networks; the switching means has been eliminated for simplicity in this discussion. The applicability of other Guillemin networks can be ruled out immediately by the realization that the time regime of interest (pulse length ≤ 150 nsec) requires the inclusion of stray inductances.

The type D network of Fig. 31(a) requires that the capacitor stray inductance be very low--on the order of 1 nH for a five-element, 100-nsec, 1-Ω line. A feasible method of achieving the desired component values is to sandwich a parallel arrangement of high-frequency disc capacitors between two parallel plates. The plate inductance would be adjusted to the required values of L_{si} by varying the spacing between plates or the distance between capacitor banks. The extent of fine tuning of the capacitors to the theoretical Guillemin value would be limited by the available components. This arrangement is difficult to model because of the uncertainty in achievable inductance. Conclusions on its usefulness cannot be made at this time.

The type-A network of Fig. 31(b) is the most feasible lumped-element simulation of a constant-impedance line for the high-rep-rate discharge systems of interest. This circuit can be constructed with physically achievable component values. In fact, the stray inductances of the discharge and series thyratron switch can be considered as part of the required main series inductance. Figure 32 shows a typical response of the circuit of Fig. 31(b) where this aspect is incorporated in an overvolted situation. The main drawback of this network is its lack of flexibility and, if a series thyratron is incorporated, its limited range of applicability. Also, the requirement for the initial charge voltage to be 2 V_G for optimum energy transfer is still present.

All arrangements of transmission lines studied showed the requirements of high efficiency and a necessary overvoltage to be mutually exclusive. Therefore, separation of the breakdown function of the circuit from the energy-delivery function through use of a separate prepulse "poker" circuit appears to be a logical solution. Figure 33 shows a simple application of this technique. A high overvoltage is supplied to the gap when switch S_p is

71
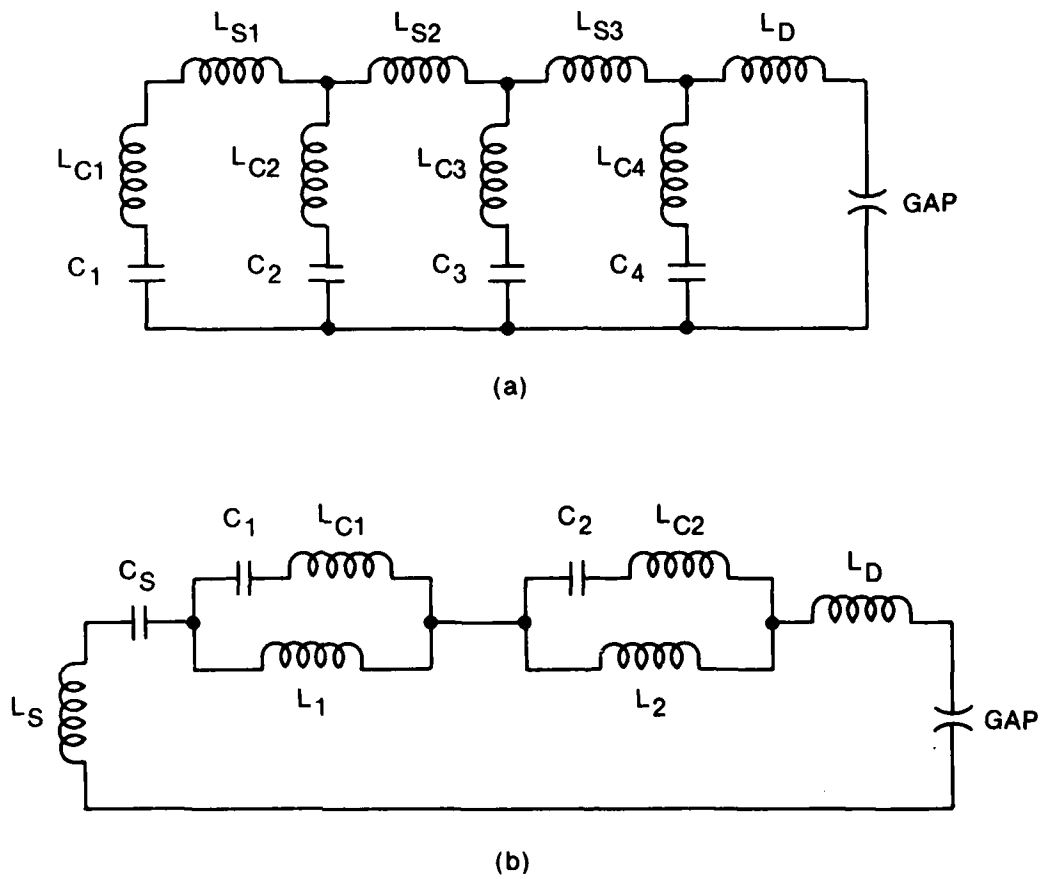
Figure 31. Electrical Schematic of Type-D (a) and Type-A (b) Guillemin Networks.
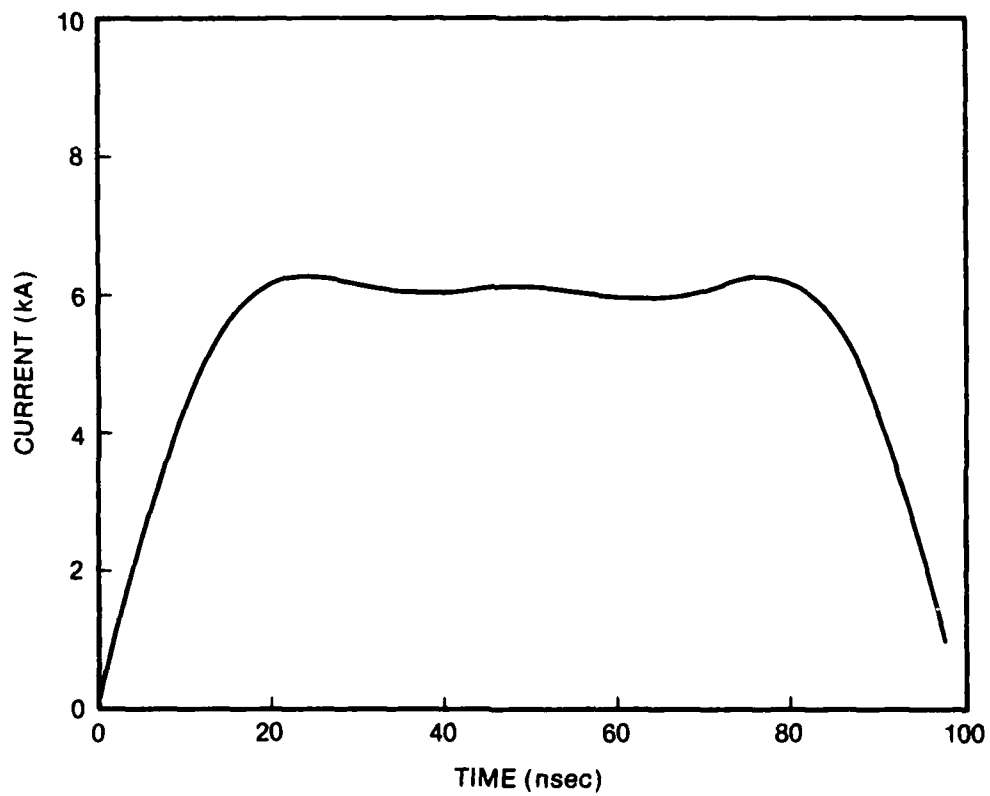
Figure 32.   Current Characteristics of Circuit of Fig. 31(b).

closed. As breakdown occurs, the main series switch S_S is closed, allowing energy to be supplied by the "matched" transmission line. Excessive ringing of the poker arm can be eliminated by resistive damping. A high efficiency is possible for a long-time-duration discharge pulse since the poker pulse need supply only a small portion of the total energy. In short-pulse applications, this advantage disappears.
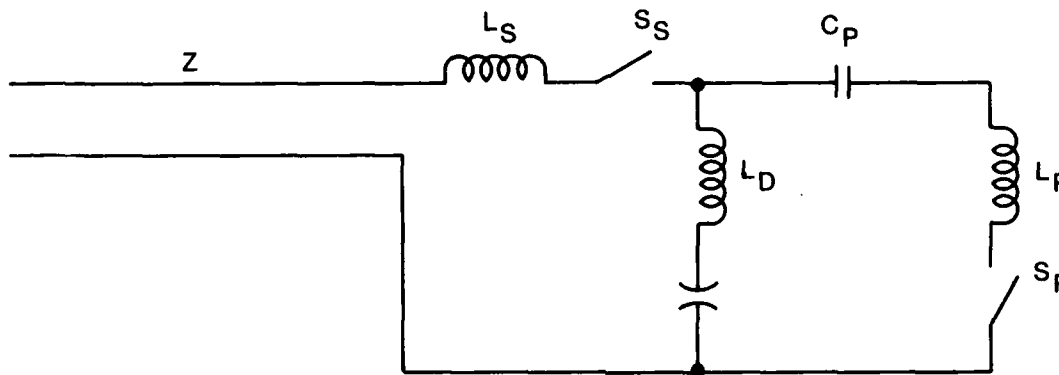
Figure 33. Electrical Schematic of Simple Poker-Pulse Application to Constant-Impedance Line-Type PFN.

As was the case with the lumped-element circuit discussed previously, the high-rep-rate main switch causes problems. At low rep-rates a rail-gap could be used; but, at repetition frequencies approaching 1-kHz, this switch must be either a thyratron or a saturable inductor.

The switch must serve two purposes: (1) as a hold-off device to prevent the discharge gap from seeing the stripline voltage until the line is fully charged, and (2) as an isolating element to prevent the low-energy poker pulse from being absorbed by the low-impedance line. The first function presents the more difficult challenge. Presently, a constant current, tetrode-controlled charging system is utilized as the interface between the power supply and the main storage capacitor. Adaptation of this system for charging the stripline is simple. However, for an energy storage of 5J, charging times would exceed 300 μsec, requiring that the output switch

74

remain open for at least this period of time. This long time period would eliminate saturable magnetics as the switching element. Resonant charging would be more efficient and would require only $\sim$ 500 nsec for the cycle, although $\sim$ 10 μsec would be necessary for switch deionization. Even this time is excessive when considering saturable magnetics in series with the discharge gap.

When the second purpose of the switch--isolation of the poker pulse--is considered, either a thyratron or a magnetic element appears feasible, but a delay between the high-voltage pulse and current flow from the stripline would occur. With the thyratron, this delay is a result of the reverse bias appearing on the switch during the poker pulse. If a saturable inductor were used, the flux built up during the high-voltage pulse would have to be reversed before saturation (and significant forward conduction) occurred. That is, the volt-seconds in each direction would have to be equal. A small delay between the ionizing pulse and the main current flow is not expected to be detrimental to laser operation. This is a function of ionization level and the extent of poker pulse ringing.

The applicability of saturating-magnetics as the isolation element will increase as this technology matures. At the present stage of development, however, the requirements of the circuit of Fig. 33 are too stringent for this type of switch. High-rep-rate operation with low stray inductance is uncertain. This will be discussed further in Section V. The use of a thyratron switch and the effect of its high stray inductance, however, can be analyzed more fully.

Figure 34 shows a somewhat idealized circuit consisting of a 40-nsec-long (one way) primary energy source and a 1-nf, 35-kV poker circuit. Both sections include switches having realistic stray inductances. Idealized diodes are used to isolate the sections from each other. The response of this circuit, then, should show the best condition achievable, considering the stray inductances. The desirable characteristics are as follows: an initial current surge due to the poker being switched on, then a fast current rise to the desired current followed by a relatively flat current value for 80 nsec (two-way line transit time), and finally a fast rate of fall of the current. Using the full discharge model (2 atm. of 94.8/5/0.2

75

He/Xe/HCl in a 1.88 cm × 24 cm^2 gap), the glow voltage is $\sim$ 9 kV; therefore, the transmission line should be charged to 18 kV and $\sim$ 7 kA of current should flow for the 80-nsec main power-deposition period. At this value, 5 J of energy is stored in the line. The poker voltage should be high, but the total energy here should not exceed $\sim$ 10% of the main-line energy. For this "best-case" representation, the 1-nF poker capacitor was charged to 35 kV, corresponding to $\sim$ 0.6 J.
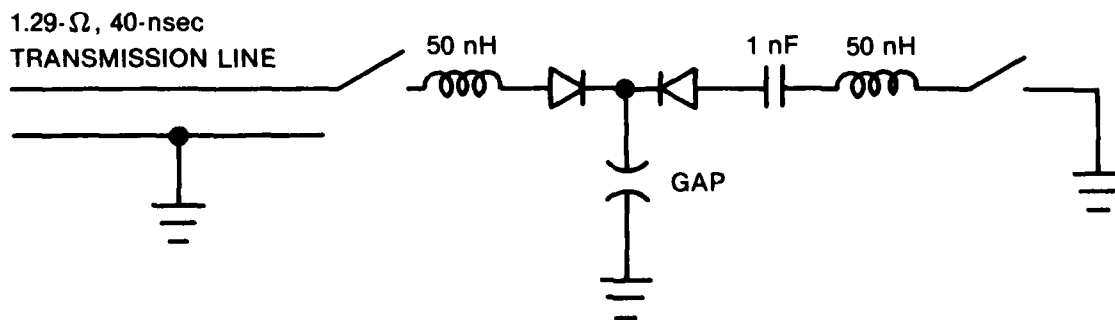
Figure 34. Electrical Schematic of Idealized PFN Utilizing Transmission Line with Poker.

Figure 35 shows the current characteristic of the circuit of Fig. 34. Obviously, the main switch inductance has drastically limited the current risetime, greatly extending the overall pulse length. Although the total power deposited into the gap is acceptable ($\sim$ 5 J), much of the energy is being deposited at low current where the electron density is too low to provide efficient pumping of the upper laser level. In addition, a realistic circuit would not include the isolating diode in the poker arm of the PFN. Without this diode, the poker arm will ring, resulting in large oscillations in discharge current and large, damaging current reversals on the poker switch.

In order for the poker concept to be successfully applied to a high-rep-rate system, some alternative means of injecting the overvoltage pulse must be found. Preliminary modeling has shown the arrangement of Fig. 36 to be the most suitable. The mutually coupled inductors of the poker and main-circuit arms make up a saturable-core transformer. A method of constructing this
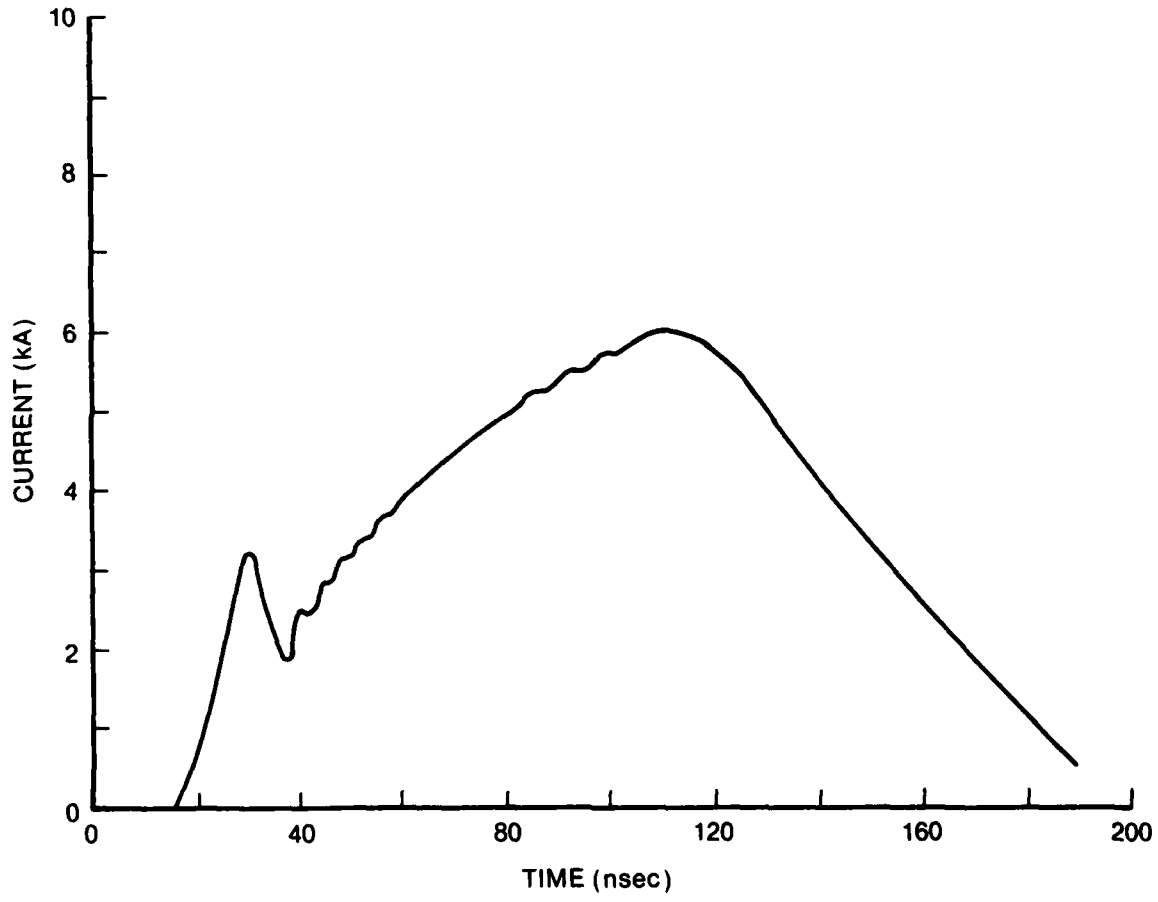
Figure 35. Current Characteristic of Circuit of Fig. 34.

transformer can be found in the later discussion of saturating magnetics. It should be mentioned here, however, that the saturated inductance must be small; the configuration is limited to a single-turn stripline arrangement.

The theory of operation of the circuit of Fig. 36 is as follows. The transformer core is maintained in or near a forward-current saturated condition-- a bias winding would generally be required. The main storage line is charged to a voltage value just below breakdown. Empirical data from the x-ray pre-ionized system which will be discussed later showed that a value of $\sim 1.7\ V_G$ can be attained with a Ne/He/Xe/HCl gas mix of 93.8/5.1/1.0/0.13 and held for ~ 500 µsec. before arcing occurs. Further studies are necessary for determination of an optimum gas mix which would allow a charge of 2 V_G on the line.

As the poker-arm switch (variable resistor R_p) is closed, the transformer core is forced out of saturation, allowing a coupling of energy from the poker capacitor to the main circuit. The current induced in the discharge circuit is such that it produces a voltage across the transformer secondary which adds to the voltage. This results in an increase of the gap potential since the gap has a very high impedance at this time. As the resulting overvoltage effects a gap breakdown, the gap potential falls below the charge level of the line. The transformer core is then forced back into saturation, allowing a low-inductance coupling of the voltage-matched transmission-line energy to the gap.

The design parameters of the saturating magnetics are somewhat relaxed for this application as compared to the more-common pulse-compression schemes. The main requirements here are that core saturation--in the reverse direction--be avoided during the application of the poker pulse and that the transition into forward saturation be rapid. This will be discussed later.

The usual limitation resulting from high thyratron inductance is not present in this circuit, assuming that it is maintained near the minimum value of ~ 50 nH. That is, as long as the total poker-circuit stray-inductance is small compared to the transformer primary, no detrimental effect will be seen. The most difficult parameter to achieve in practice is the coupling

78

efficiency of the transformer. A value of 50% is used in modeling and is considered reasonable. This makes the coupling of the poker energy somewhat inefficient, but the loss represents only a small percentage of total circuit energy.

The major advantage of the circuit of Fig. 36 is its ability to effect a transfer of a large amount of energy while passing only a small portion of this energy through the actual switch. In other words, the thyratron operating parameters can be well below its limits, leading to long-lifetime operation. Ringing in the switch circuit is of sufficiently low energy that damage is not likely. In addition, a small amount of damping resistance should not adversely affect the circuit operation.

Unfortunately, time and equipment constraints prevented further modeling and experimental development of this technique. Preliminary results in air gaps using a standard iron-alloy, cut-race-track core showed promising results. Further development of the transformer and further studies of gap holdoff voltages are required. The limiting repetition rate is the remaining important question. Assuming residual ionization in the gap as a result of the previous pulse, it is expected that the holdoff voltage will decrease as rep-rate increases. The transformer-coupled poker arrangement is a promising, but yet unproven, technique applicable to many classes of gas-discharge lasers.

The switched transmission line of Fig. 28, mentioned previously, was the only constant-impedance line found to be feasible for the present laboratory system, considering time and equipment constraints. This method has limited applicability. For discharge voltage-current characteristics requiring a line impedance of ≥ 1.5 Ω, the voltage risetime of the wave reaching the discharge is acceptable for a switch inductance of 50 nH. That is, the effective L/R risetime will be ~ 17 nsec. Figure 37 shows the results of this situation. Note that the current risetime is very fast.

The results of Fig. 37 are based on a He-rich mixture which exhibits a larger E/N for a given current than would a Ne buffered mixture. A higher efficiency of electrical energy conversion to laser energy, however, is
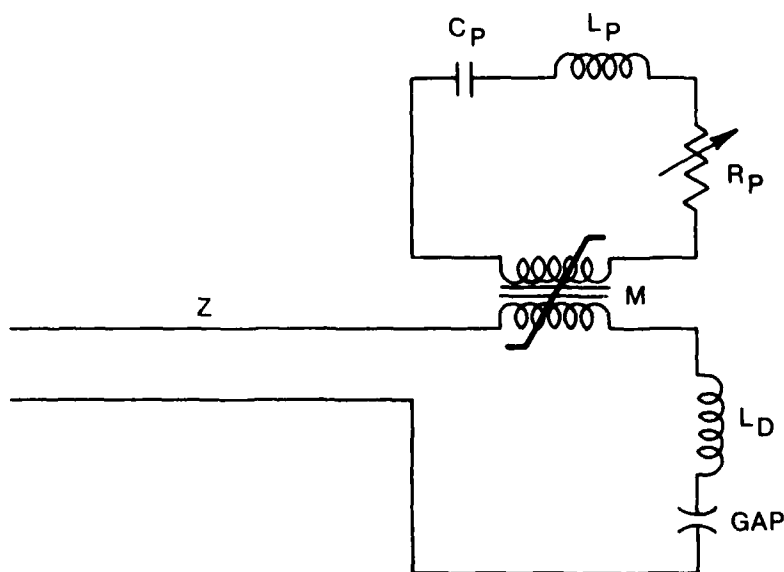
Figure 36. Electrical Schematic of Transformer-Coupled Poker
Pulse.
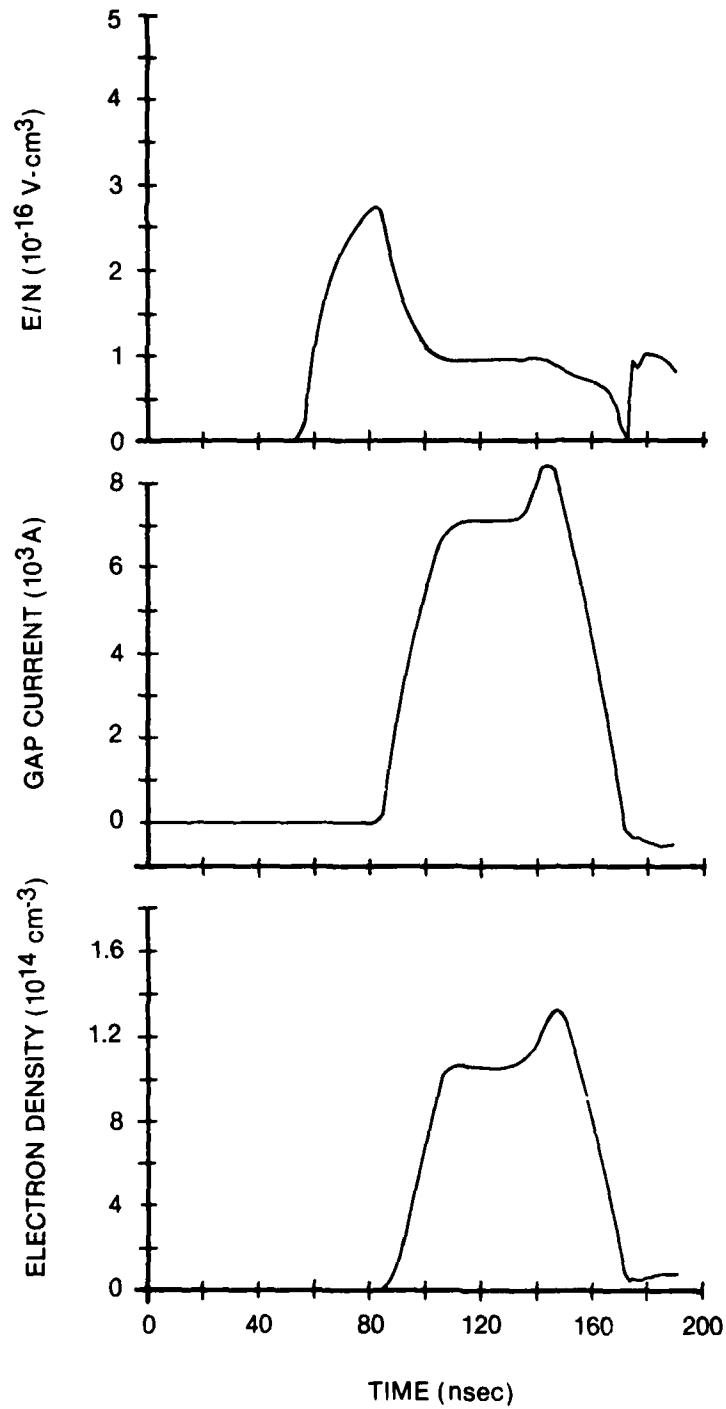
Figure 37. Calculated E/N, Gap Current, and electron Density for
Circuit of Fig. 28. Initial charge voltage = 27 kV.

attained with the Ne-buffered mixtures. Therefore, for the more-efficient mixes, a lower-impedance line is required. However, as the line impedance is lowered, the L/R voltage risetime at the switch will decrease. For example, for a 0.5-Ω system switched with a 50-nH thyratron, the effective L/R time would be 50 nsec. This is unacceptable.

This situation could be rectified by operating at higher pressures and/or gap spacings. The present discharge chamber did not allow for this; therefore, experimental verification is lacking.

END

FILMED

DTIC

III 1.0 ᴇᴇ 2.8 2.5
ᴇᴇ 3.2
III 1.1 ᴇᴇ 3.6 2.2
4.0 2.0
1.8
III 1.25 III 1.4 III 1.6
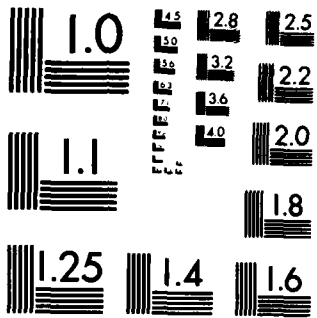
MICROCOPY RESOLUTION TEST CHART
NATIONAL BUREAU OF STANDARDS-1963-A

Section III

CLOSED-CYCLE, HIGH-REPETITION-RATE XeCl LASER

The closed-cycle, high-rep-rate laser constructed during the course of this effort is described in this section. Initially, UV preionization was employed, but a rapid buildup of contaminants caused by the spark sources rendered the results unreliable. An x-ray preionizer installed later essentially eliminated the contamination problems and permitted consistent, reproducible results to be obtained.

CLOSED-CYCLE-LASER APPARATUS

A closed-cycle recirculating-flow loop, previously used as a rare-gas laser,[29,30] was modified to accept a 50-cm discharge length. Figure 38 shows the basic loop without the discharge electronics and associated equipment. The loop mainly consists of commercial-stainless-steel high-vacuum tubular plumbing having a nominal ID of 6 in.; copper gaskets were used at all tubing junctions. Each of the transition channels is 2 ft in length, fabricated from 304-L stainless steel, and shaped so as to provide a somewhat smooth--although compact--transition to and from the $\sim$ 1-in. high by $\sim$ 2-ft wide by 1-ft long center discharge section. The frame of the discharge section is also constructed from 304-L stainless steel; viton O-rings provide the vacuum seal between the transition sections and the discharge section.

A 400-ℓ sec^{-1} turbomolecular pump is used for system evacuation, and all valves and miscellaneous connections are high-vacuum compatible. The basic system is designed to be bakeable to $\sim$ 250°C, except for the rotary feed-through which can be water-cooled during baking. With the discharge-section components (electrodes, insulator, etc., as described below) installed, the maximum temperature is reduced to $\sim$ 150°C. A base pressure of $\sim$ 10^{-7} Torr has been achieved.

Gas filling is accomplished through a gold-seal high-vacuum valve connected to a manifold; only high-purity gases are used. The driving force for the

83

VIEWPORT

BELLOWS

FAN MOTOR

VACUUM ROTARY
FEEDTHROUGH

DISCHARGE REGION

FAN IMPELLER

OPTICAL PORT

OPTICAL PORT

FLOW →

FLOW TRANSITION
REGIONS

TURBOMOLECULAR
VACUUM PUMP

GAS SUPPLIES

HIGH-
VACUUM
VALVES
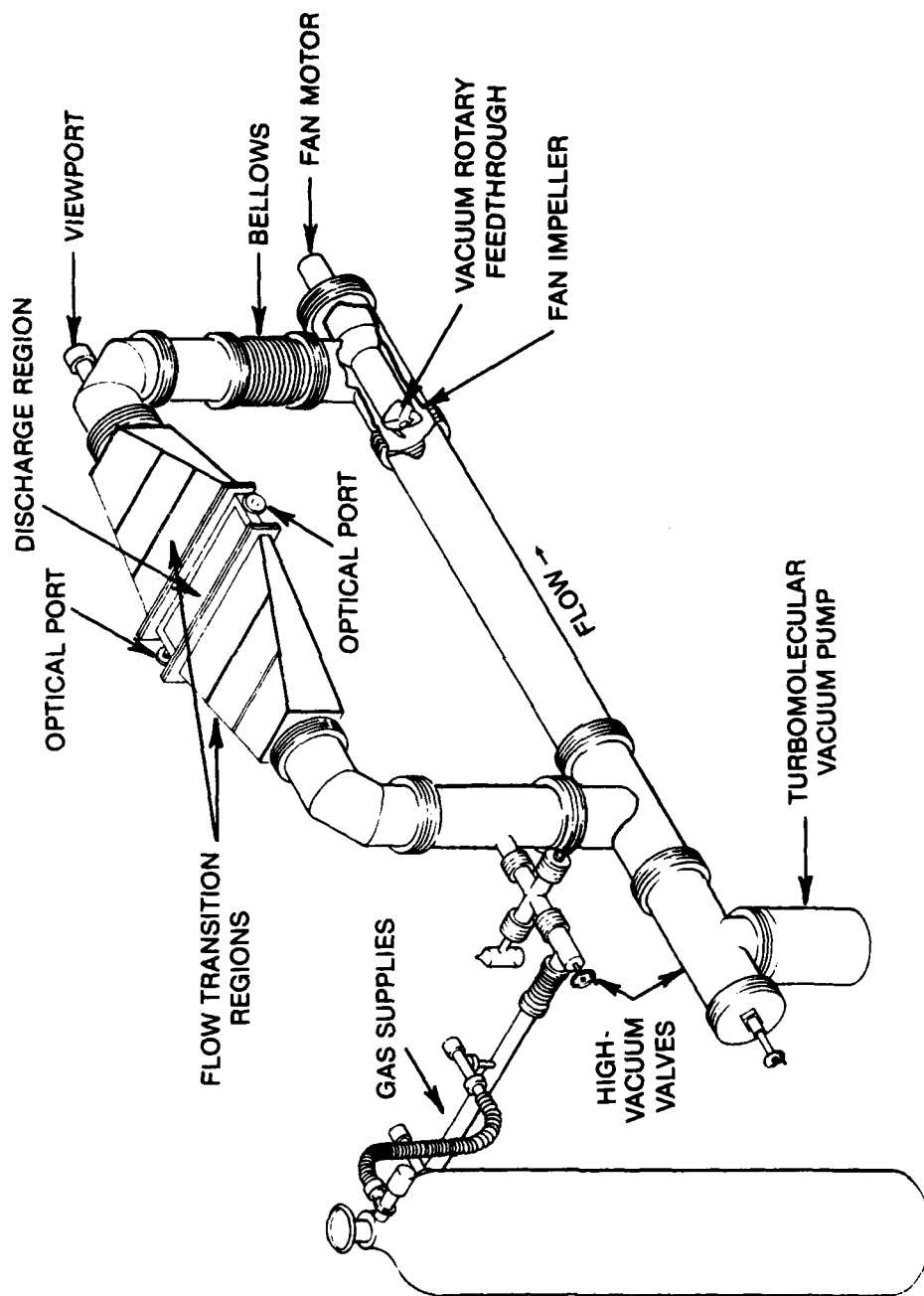
Figure 38. Isometric View of Closed-Cycle XeCl-Laser Flow Loop.

84

gas flow is supplied by an external motor connected to an internal vanaxial fan impeller through a commercial Ferrofluidic[31] feedthrough. Maximum rotary speed is ⋄ 11000 rpm; the typical operaton is at 30 - 70% of this speed.

A cross-sectional view of the discharge section with the electrodes in place is shown in Fig. 39. The UV preionization source depicted was a linear array of flat-head screws but was later changed, as will be discussed below. The anode for the UV preionized discharge is a stainless-steel screen having ⋄ 55% transparency. The anode mounting plate and flow-ramps were fabricated from aluminum and then Ni-plated. The ramps on each side of the anode screen are used to achieve a smooth physical transition and, thereby, minimize flow-generated turbulence. With this arrangement the anode is maintained at ground potential. When x-ray preionization is used, the entire anode assembly is replaced with a Ni-plated aluminum assembly where the anode is continuous, i.e., a screen material is not required. This will be treated in greater detail in the discussion on the e-beam preionized laser.

The pulsed electrode serves as the cathode and is constructed from stainless steel and mounted in a 1-in.-thick machined Kynar[32] plate, with machined flow-ramps attached. The cathode is 50 cm long by 0.5 in. wide at the base. The edges along the length are rounded to produce a 0.5-cm-wide flat surface. Originally, discharge arcing was observed at both ends; these edges were then gradually tapered until arcing ceased. The tapers extend ⋄ 2 cm in from each edge.

Flow-velocity profiles were obtained by replacing the cathode assembly with a Lucite fixture having a shape similar to that of the flow-ramp electrode combination but containing a sliding pitot-static probe.

The velocity profiles shown in Fig. 40 were obtained by traversing the 1/16-in.-diam. probe horizontally along the 50-cm length of the discharge region and vertically across the 2.25-cm gap. The proximity of the probe to a boundary results in an error which decreases from 3% at one probe diameter to 1% at five probe diameters from the boundary.
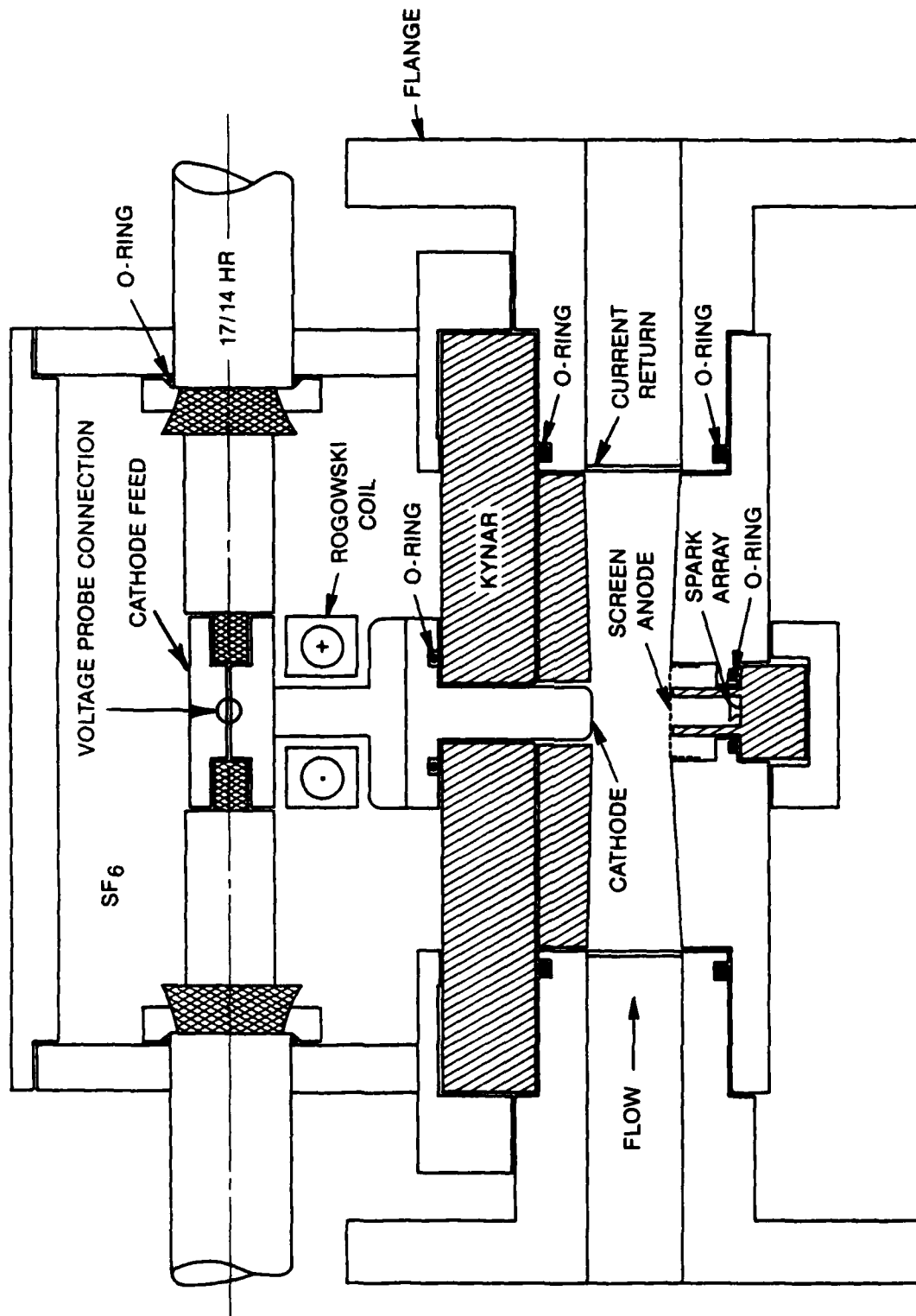
Figure 39. Cross-Sectional View of XeCl-Laser Discharge Section.
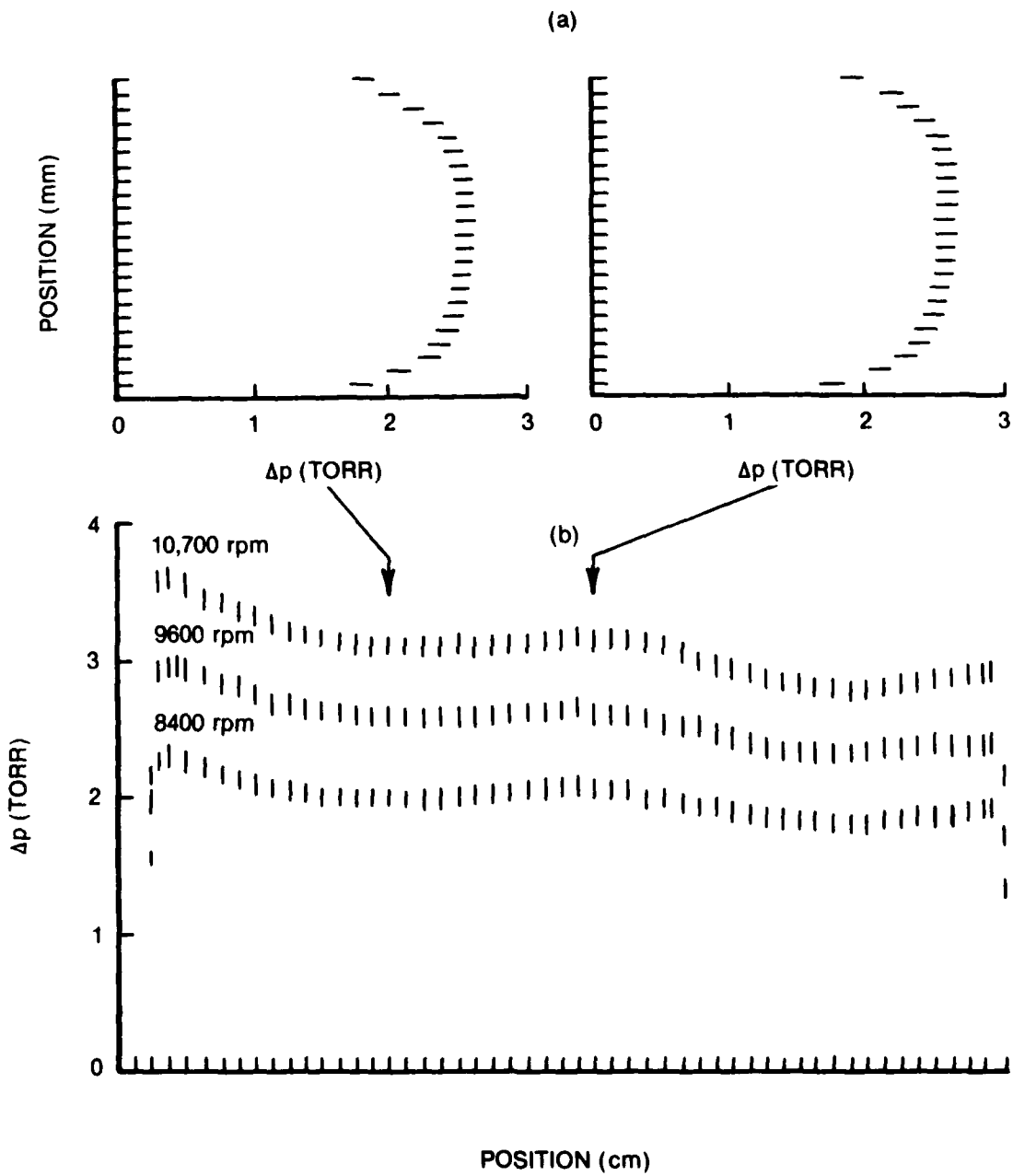
Figure 40. Vertical (a) and Horizontal (b) Velocity Profiles in Discharge
Region of Closed-Cycle XeCl Laser.

The vertical profiles in Fig. 40(a) are reasonably uniform and their shape is characteristic of turbulent flow. The horizontal profiles in Fig. 41(b) appear to have a periodic structure which may be the result of swirl induced by the fan impeller. Even so, the flow uniformity is sufficient for XeCl-laser discharge operation. For example, in the 9600-rpm curve, the difference between the maximum velocity of 87 ft /sec and the minimum velocity of 77.5 ft /sec is 11.6%.

In an attempt to improve the horizontal velocity profile, a flow straightener having 0.375-in. hexagonal cells was installed in the 6-in. cylindrical input to the converging flow transition. The resulting velocity profiles are shown in Fig. 41. Obviously, flow uniformity deteriorated in both the vertical and horizontal directions. For the horizontal profile, the difference between the maximum velocity of 90 ft /sec and the minimum velocity of 67.5 ft /sec is 29%.

It appears from the results of Figs. 40 and 41 that large-scale turbulence at the input to the converging nozzle is beneficial in spreading the flow horizontally. Rather than reduce the turbulence (e.g., with a flow straightener) at the input to the converging nozzle, it would appear to be more effective to condition the flow further upstream or downstream.

Subsequent to these measurements vanes were added ∿ 5 cm from the center of the discharge gap on both the upstream and downstream sides. These vanes, constructed of 0.025-in. stainless steel, are 1 cm long, spaced 1 cm apart, and welded in place. They serve two purposes--as an aid in flow straightening and as an electrical current return for the discharge. The leading edges of the downstream vanes are glass-coated to provide electrical insulation from the discharge.

The materials exposed to the laser-gas mixture were chosen both for high-vacuum compatibility--in order to maintain a very low contamination level--and for compatibility with the halogen donor, HCl. Stainless steel, Kynar, and Viton appeared to satisfy these requirements. The copper gaskets used with the vacuum plumbing are not compatible with HCl, but the surface area is sufficiently small that no adverse effect was observed, other than

88

(a)

POSITION (mm)

Δp (TORR)   Δp (TORR)

(b)

4

3

2

1

0

Δp (TORR)

9600 rpm

POSITION (cm)
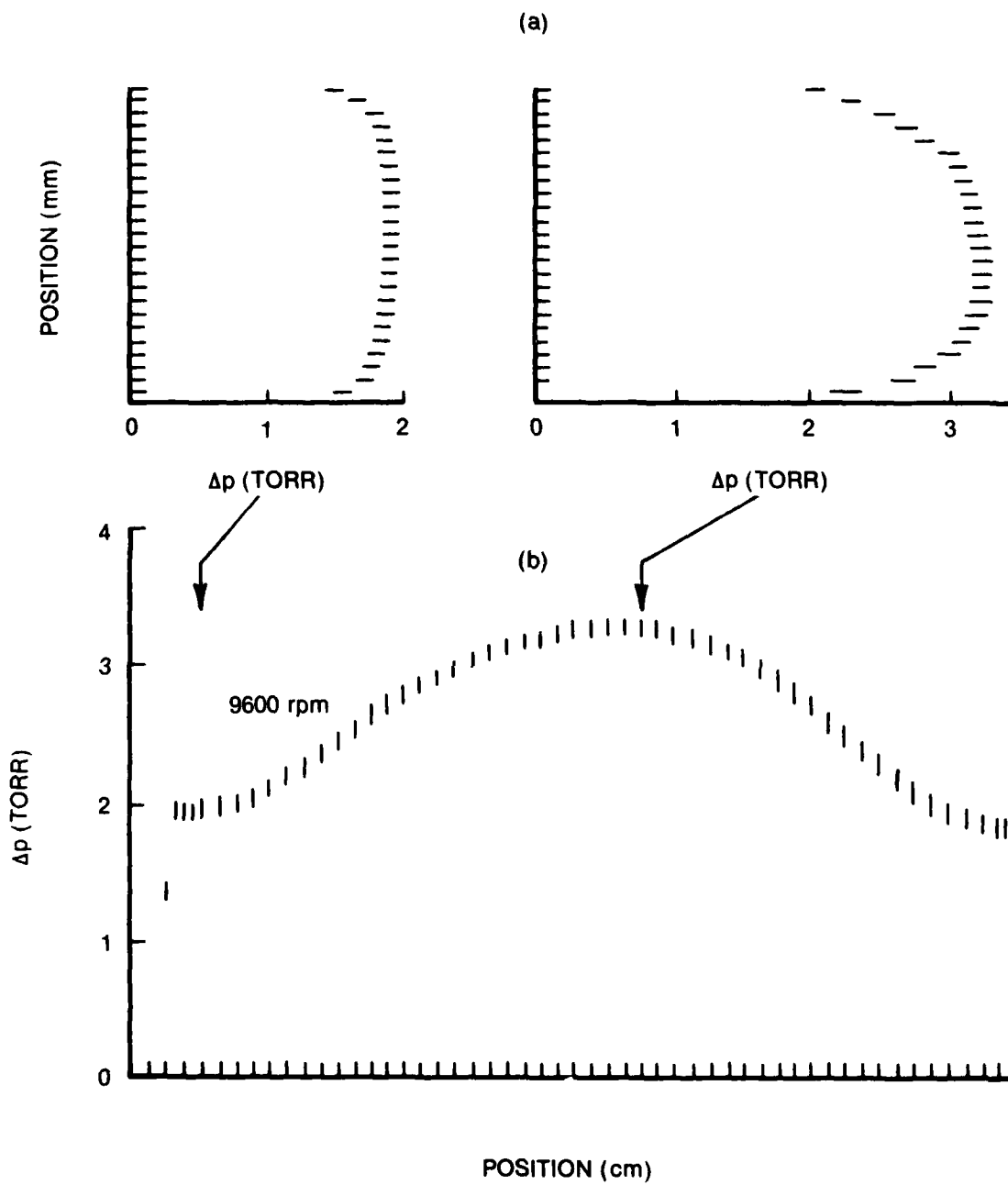
Figure 41.   Effect of Flow Straightener upon Vertical (a) and Horizontal (b)
Velocity Profiles.

discoloration of the gasket; the gas did not appear to be contaminated by CuCl compounds. The Kynar presented a problem only in the vicinity of the high-intensity, UV preionizing spark array. This will be treated in more detail in the discussion on UV preionization. Although Al was the most viable material for the machined anode mounting plate and the recirculating fan impeller, problems had been reported with its use in other rare-gas/HCl gas-discharge lasers.[33-35] Reaction between Al and HCl forms $AlCl_3$ powder on exposed Al surfaces; these difficulties are best avoided by coating or plating the surfaces. For the cast-Al fan impeller which presented the greatest difficulty, a coating of Kynar was considered; a Ni-plating process seemed most appropriate for the machined Al surfaces.

A new fan impeller was purchased with the specifications that there be no stamped markings on the impeller and no epoxy fillers used during the balancing process. There are two significant factors related to the use of Kynar as a protective coating for the impeller. First, the resulting Kynar layers would weigh over 100 g; for this particular impeller, the additional weight is more than 25%, which would undoubtedly necessitate rebalancing. Second, and more restrictive, is the requirement of removing all sharp edges and corners (1/16-in. radius) to ensure an even coating. Although the overall efficiency changes resulting from such modifications are known, the combination of these effects precludes the use of Kynar on this particular application.

Several investigators[36,37] have claimed success with plating the exposed metals of rare-gas halide lasers using either Ni electroplating or the electroless Ni process.[38] Since this success has been achieved in non-critical vacuum environments, uncertainty surrounds their use in more demanding vacuum applications. The Ni-plating processes provide a layer of composition $\sim$ 92%(Ni + Co), 8% P. The vapor pressure of phosphorus is too high for vacuum operation; therefore, there was concern over the possibility of P coming off the plating. The as-plated Ni is an amorphous layer of a supersaturated solid solution of P in Ni. Because of the metastable nature of this coating and the possibility of the release of P, this plating would not be recommended for high-vacuum operation. Heat treatment of Ni plating

90

at 350°C for several hours cause separation into two crystalline phases--Ni_3P and Ni. In this state the plating is more stable and possesses a greater degree of hardness[38] and most of the P is tied up in Ni_3P, which may reduce or eliminate the possibility of P release. The high-vacuum characteristics of plated Ni and heat-treated Ni plating are only speculative since no reports have been found in the literature.

In an attempt to find answers to some of these questions, five 2-g specimens of Al were plated with 0.0005 in. of electroless Ni. Three were baked in air at 200°C for 3 hr. Evolved-gas analyses of the plated samples up to 200°C in vacuum by TG-MS techniques gave no indication of the presence of P or any other inorganic volatiles. Traces of organics--some N_2 and O_2 and, principally, H_2O--were evolved over a 4-hr period. No appreciable difference in the amount of degassing was found among Al, electroless Ni-plated Al, and electroless Ni-plated and baked Al.

Consequently, the Al impeller, anode mounting plate, and two flow ramps were plated with 0.0005 in. of electroless Ni. Consistent with expectations from preliminary tests, the flow ramps were plated successfully with a uniform Ni layer. Limited success was achieved with the impeller made from cast Al. This was expected because of the pits and crevices in the cast-Al surfaces. The entire convex region of the impeller appeared to be plated uniformly, but a small region on the concave surface was not completely coated. One explanation was that the uncoated region was not dry after the cleaning process. The anode mounting plate which was machined from Al tool plate was also plated with limited success. The plating appeared quite uniform; however, the surface had experienced pitting prior to plating (presumably, during the cleaning process).

The thermal behavior of Kynar in vacuum was also analyzed by TG-MS methods. Below 100°C there was no detectable weight loss (i.e., < 10 μg of a 26.4-mg sample). Over the temperature range 140 - 210°C, some solvents and water were observed in the evolved gases. Consistent with the manufacturer's reports, no monomer (vinylidene fluoride) was detected. As a result of this analysis, the maximum temperature for vacuum was limited to 150°C.

91

Figure 39 shows the connection of the capacitor-transfer PFN to the cathode. Two identical, but independent, PFN's are switched simultaneously. The cables, serving the function of a low-inductance capacitor, are clamped in parallel along the cathode assembly. The cable terminations are sealed in an atmosphere of SF_6 in order to prevent corona. Discharge-voltage measurements are obtained with a commercial high-voltage probe connected to this clamping plate; current is monitored with a commercial Rogowski-type dI/dt probe and passive integrating system. This coil extends along the length of only one side of the machined bar connecting the mounting plate to the cathode.

An electrical schematic of the PFN utilized for the discharge studies is shown in Fig. 42. This is essentially a capacitor-transfer-type PFN, with the low-inductance capacitor being made up of the 16 parallel-connected cables. The total capacitance of each cable set is 3.7 nF, and the lumped inductance is 7.5 nH, which is much lower than the $\sim$ 100 nH inductance of the 5-nF/thyratron branch of the PFN. The one-way transit time of the cable set is $\sim$ 5 nsec.; therefore, the cable branch will exhibit some of the characteristics of a constant-impedance PFN for current risetimes of $\leq$ 20 nsec. However, comparison of the circuit waveforms with lumped-element and constant-impedance models showed that the former model sufficiently depicts circuit operation.

All components were chosen to provide a repetition frequency of $\geq$ 1.5 kHz. The charge-control circuitry which feeds the circuit was developed under a previous contract for a 10-KHz rare-gas laser. This circuitry was modified only slightly in order to accommodate a longer fiber-optic cable. Details are contained in the operator's manual.[39] The DC bias circuits were also constructed under the previous effort,[29] as was the pulse-control timing circuitry. The latter circuit was expanded in order to provide adjustable synchronization between the two thyratrons and between the thyratrons and the preionization pulse. Details of this modification are also contained in the operator's manual.

As mentioned in the previous section on the requirements of high-rep-rate PFN's, the thyratron was used as the switching element in order to attain
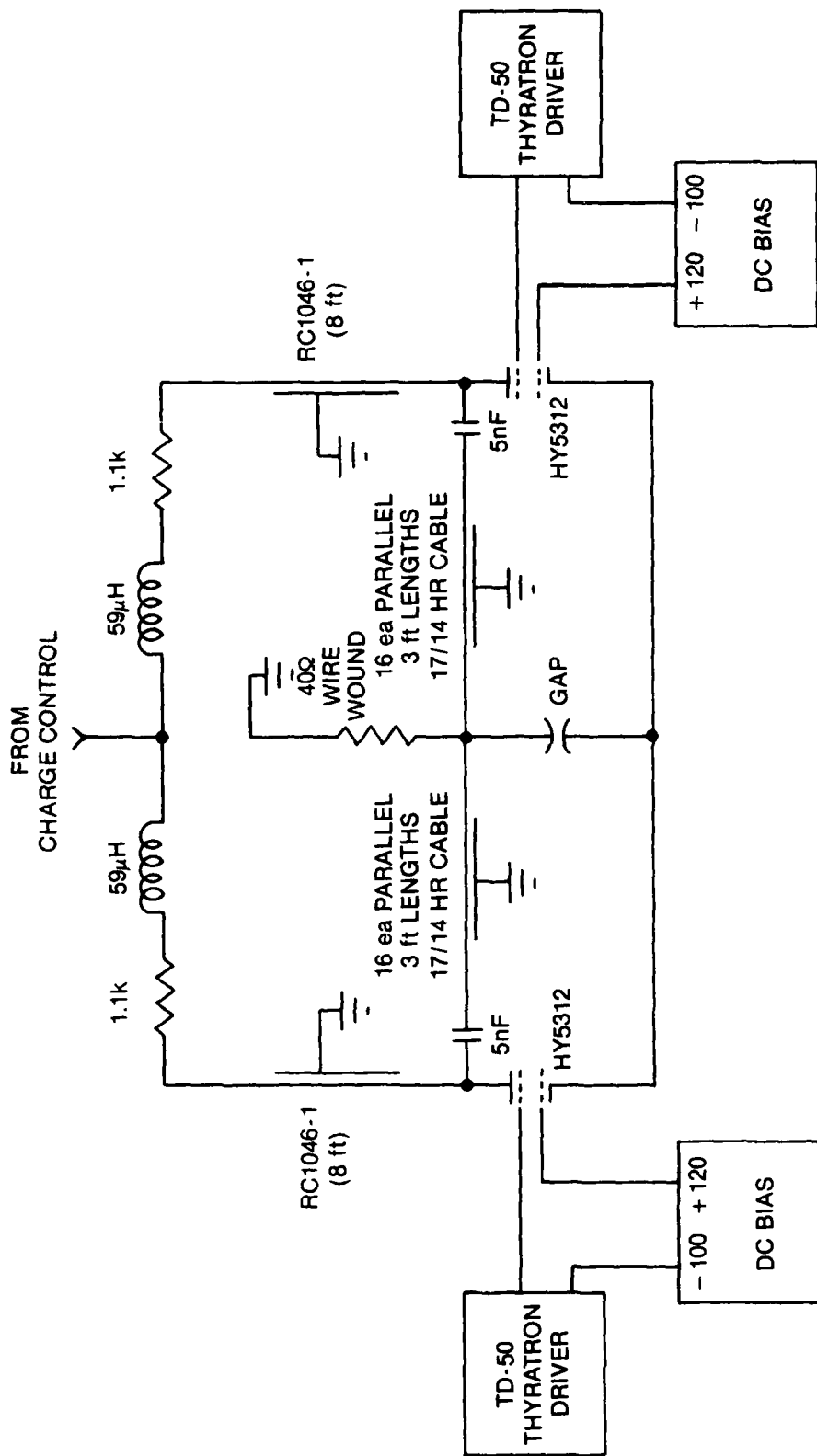
Figure 42. Electrical Schematic of High-Repetition-Rate XeCl-Laser Capacitor-Transfer PFN.

the desired pulse-repetition rate. Some problems were encountered in reliably switching the two thyratrons simultaneously. Installation of Impulse Electronics (New Haven, CT) thyratron drivers alleviated most of the problems, although the addition of line-filtering toroids in various parts of the circuit was found to be necessary for the prevention of circuit overloads.

During operation at high voltage and high rep rate, breakdown of the cable connection at the charging supply was encountered. This situation was resolved by terminating the Rowe RC 1046-1 cable with a high-dielectric-constant tape which, in effect, graded the discontinuity occurring at the terminated shield. The system is now capable of operating with a charge voltage of up to 30 kV and at a repetition rate of up to $\sim$ 1.5 KHz, although satisfactory operation can be achieved for a charge voltage as low as 20-kV. The rep rate is, at this time, limited primarily by the high-voltage sup-plies and timing circuits, not by the discharge operation.

As mentioned earlier, commercial voltage and current monitors were utilized for discharge-circuit waveform recording. The available length of cable on the Tektronix P6015 high-voltage probe, however, was not sufficient for direct connection to the oscilloscope. Consequently, this probe was termi-nated into the 1-MΩ input of a Tektronix P6201 FET voltage probe having an X100 attenuator tip which reproduced the voltage waveform into a 50-Ω coaxial line connected to the oscilloscope. Voltage compensation was adjusted with the aid of a nanosecond pulser; good representation of wave-forms was achieved for a risetime of $\geq$ 10 nsec.

Interpretation of the current monitor data, however, is not so straight-forward. Frequency-dependent amplitude and phase shifts are present in the T&M Research Products (Albuquerque, NM) dI/dt-probe/passive-integrator combination. The equivalent circuit of the current-monitoring system is shown in Fig. 43. Basically, the change in discharge current induces a current in the dI/dt probe through the mutual inductance (M) of the dis-charge line and L_p. The output of the probe is fed through $\sim$ 30 ft of 50-Ω coaxial cable which is terminated into a 50-Ω coaxial load. The voltage at the load is also seen by the passive integrator which is terminated into a
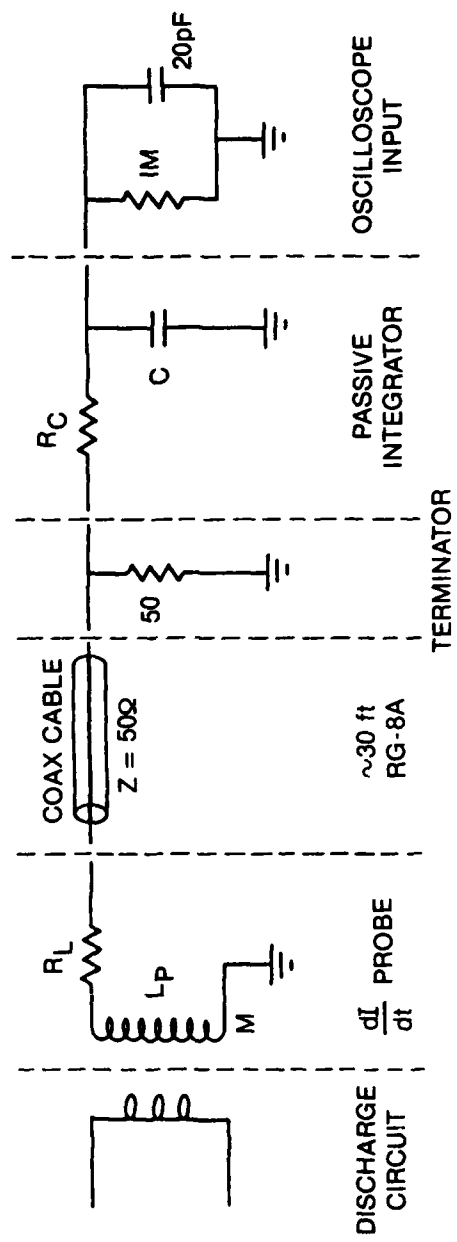
Figure 43. Equivalent Circuit of Discharge-Monitoring dI/dt Probe System.

1-MΩ oscilloscope preamplifier. The manufacturer has provided values of R_L, L_p, RC time constant (τ) of the passive integrator, and scaling factor (S) from which M can be calculated. The values of R_C and C were obtained by measuring R and calculating C. The following are the component values of the present discharge dI/dt probe system:

$S = 2889$ amps $volt^{-1}$ μsec^{-1}

$L_p = 300$ nH

$M = 0.45$ nH

$R_L = 15$ Ω

$\tau = 10.3$ μsec

$R_C = 10.0$ KΩ

$C = 1.03$ nF

$Z = 50$ Ω

Comparison of the values of R_C and C with the oscilloscope input impedance indicates that the scope input has a negligible effect upon the circuit operation for the time range of interest (≤ 250 nsec). Also, the reflections of the integrator signal back into the coaxial cable can be considered insignificant for two reasons. First, the two-way transit time of the ∿ 30-ft length of cable is ∿ 90 nsec which is the extent of the waveform information of interest. Secondly, R_C is ∿ 200 times larger than the cable impedance; therefore, only ∿ 0.5% of the passive-integrator-voltage value will be fed back into the cable. This would present a problem only if one were interested in small currents following a large signal.

Circuit analysis proceeds by treating the cable as a 50-Ω load in the dI/dt probe circuit. The voltage developed across this load then becomes a voltage source at the input of the passive integrator. The series of equations describing the overall circuit can be simplified in such a way that the discharge current (I_d) is related to the integrator output (V_c) by

$$I_d = S\ [\frac{L_p}{R_p}\ \tau\ \frac{dV_c}{dt}\ +\ (\frac{L_p}{R_p}\ +\ \tau)\ V_c\ +\ \int V_c dt] \qquad (49)$$

where R_p is the probe-current-leg effective series resistance ($= R_L + Z$). With the use of numerical techniques, the discharge current can be determined from Eq. (49), given the magnitude and waveshape of the passive-integrator output.

To illustrate the operation of the current-measuring system, assume a sinusoidal current of

$$I_d = A \sin \omega t \tag{50}$$

Also, assume that all currents and voltages are zero at time zero and that ω is greater than 10^7 (period $\leq$ 600 nsec). The output of the passive integrator (V_c) will then be

$$V_c = \frac{1}{S\tau} \frac{K^2}{K^2 + \omega^2} A [\sin \omega t + (\frac{1}{\omega \tau} - \frac{\omega}{K}) \cos \omega t + \frac{\omega}{K} e^{-Kt}] \tag{51}$$

where $K = R_p/L_p$. This can be restated as

$$V_c = \frac{1}{S\tau} \frac{K^2}{K^2 + \omega^2} [I_d + \frac{1}{K}\frac{dI_d}{dt} + \frac{1}{\tau}\int I_d dt + \frac{\omega}{K} e^{-Kt} - \frac{1}{\omega t}] \tag{52}$$

It should be pointed out that Eqs. (51) and (52) have been simplified from a more complicated expression for V_c. The elimination of terms was based upon the component values of the present probe system. If a different probe system should be used (e.g., if τ = 1 μsec), then a re-evaluation of these terms would be required.

The above equations show that the waveform observed on the oscilloscope is not only a function of the scaling factor $S\tau$ but also dependent upon the wave shape. Both a frequency-dependent phase shift and a frequency-dependent amplitude perturbation will be present. Figure 44 illustrates this point for sinusoidal waveform periods of < 200 nsec. For longer periods, both the time shift and amplitude will gradually decrease again.

97
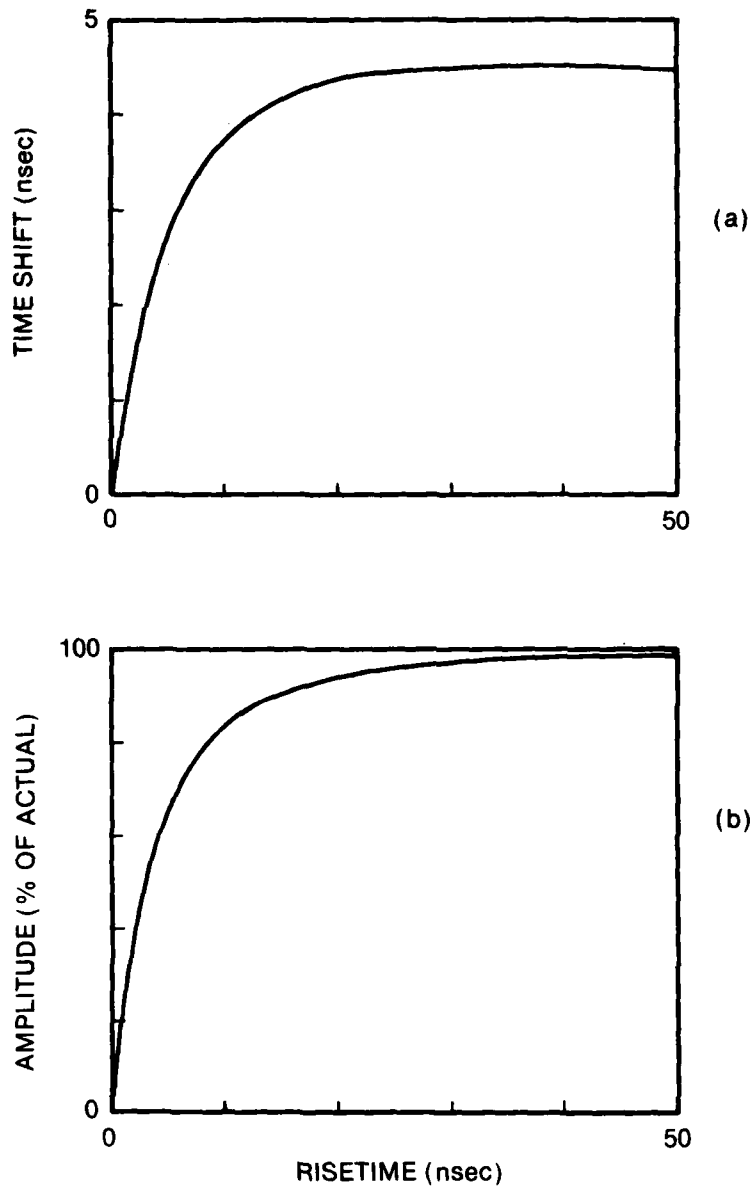
Figure 44. Time Shift (a) and Amplitude (b) of dI/dt Probe Passive-
Integrator Output as Function of Risetime (= One-Fourth
of Total Period) for Sinusoidal Current Waveform.

98

A software routine incorporating Eq. (49) was written for a desk-top calcu-
lator to permit digitization of previously recorded waveforms and cal-
culation of compensating factors. Unfortunately, complete success was never
achieved in comparing the voltage and current waveforms. Some additional
phase shift was generally present, preventing perfect matching of the
zero-crossing points. Unsuccessful attempts were made to explain this
discrepancy with stray capacitance. The most logical explanation results
from the placement of the probe on only one side of the cathode feed. Any
imbalance in the two parallel PFN circuits would result in a net current
flow from one branch to the other, as was clearly visible when the thyratron
firing times were purposely altered. Although perfect representation of the
current waveforms was not achieved, a very close, useful approximation was
obtained.

The optical-cavity components are not shown in the laser-flow-loop diagram
of Fig. 38. The cavity consists of a total reflector (> 99% at 308 nm) and
a partial transmitter installed in moveable mounts. Best laser operation
was obtained with a 65% R/32% T partial transmitter (where R $\equiv$ reflection
and T $\equiv$ transmission), although a 40% R and 87.5% R/9.6% T were also used.
All reflectors are of dielectric construction and mounted internal to the
cavity. The outside surfaces are AR-coated. Cavity alignment is adjustable
via stepper motors and remote controllers.

An estimate of the output power which could be expected from the closed-
cycle XeCl laser was made using Rigrod's[40] approximate solution for a
homogeneously broadened CW laser with uniform distributed loss

$$\frac{I_{out}}{I_s} = \frac{(1 - a - r)}{(1 - r)} \frac{(g_0 - \alpha_0)L + \ln\sqrt{r}}{(1 - \frac{\alpha_0 L}{\ln\sqrt{r}})} \tag{53}$$

where I_s = saturation intensity, a = output mirror loss, r = output mirror
reflectance, g_0 = unsaturated gain coefficient per unit length, α_0 = constant
loss coefficient per unit length, and L = length of active medium. The
applicability of this expression to pulsed lasers will be discussed later.

99

In order to calculate the output power from the above expression, it is necessary to have values for I_s, g_0, and α_0. A survey of the technical literature at the time of the calculation yielded the data presented in Table I. A g_0 value of 6%/cm at 1 GW/ℓ atm pumping was obtained from Taylor's[42] results. This is the expected level of pumping for the closed-cycle XeCl laser utilizing a 10-nF energy-storage capacitance charged to 35 kV, a discharge volume of $0.5 \times 2 \times 50$ cm^3, and a 3-atm. mixture of Xe, HCl, and He or Ne.

Loss data for He/Xe/HCl mixtures were not found, except for Sze's data[46] which are unreasonably high. Therefore, Champagne's value[43] of α_0 = 0.25%/cm for an e-beam-pumped Ne/Xe/HCl mixture was used for the I_{out} calculation. Since this loss was attributed to Ne$_2^*$ absorption, the loss in a He-buffered mixture could be much different.

The saturation intensity is given by

$$I_s = \frac{h\nu}{\sigma\tau} \tag{54}$$

where σ = stimulated-emission cross section,

$$\tau = \frac{1}{\tau_{rad}} + \sum_n Q_n N_n + \sum_{k\ell} Q_k N_k N_\ell \tag{55}$$

τ_{rad} = radiative lifetime, and the $\sum\limits_n$ and $\sum\limits_{k\ell}$ terms are the result of two- and three-body quenching processes. Considering the radiative lifetime only and using the theoretical value[47] of 50 $\mathring{A}^2$nsec for $\sigma\tau_{rad}$ yields a saturation intensity of 1.3×10^5 W/cm^2. Finn, et al.,[48] have measured quenching-rate constants for e-beam-excited mixtures of Ne/Xe/HCl and found two-body quenching by Ne and by HCl to be the major loss processes. Using their rate constants of 1.0×10^{-12} cm^3/sec for Ne and 1.4×10^{-9} cm^3/sec for HCl, along with the radiative lifetime of 11 nsec, yields an I_s value of 5.8×10^5 W/cm^2 for a 3-atm Ne/Xe/HCl mixture containing 0.2% HCl.

The following values were used to calculate the output power from the closed-cycle XeCl laser: g_0 = 6%/cm, α_0 = 0.25%/cm, I_s = 0.58 MW/cm^2, and L = 50 cm.

100

Table I

GAIN AND LOSS DATA FOR XeCl LASERS

Reference	Active Volume	Excitation	Gas Mix	Input Energy	Laser Output	Gain (%/cm)	Loss (%/cm)	I_s (MW/cm²)	Outcoupler
Champagne[41]	380 cm³	e-beam-pumped	Xe 1.08×10^{18} cm^{-3} HCl 7.2×10^{16} Ne 4 atm.	-- --	3 J/ℓ 0.5-μsec pulse eff = 5%	2.6	~ 0.26	0.35	28%R
Taylor, et al.,[42]	14 cm³ amplifier	UV preionized LC driver	HCl/Xe/He 1:10:1400 3 atm	3.6 MW/cm³ 0.144 J/cm³ deposited in discharge	--	7.3	Neglected	0.25	--
Champagne, et al.,[43]	380 cm³	e-beam-pumped 1-μsec pulse	Ne/Xe/HCl 0.988/0.01/0.002 4 atm	7 A/cm²	--	2.6	~ 0.25	--	--
Nighan and Brown[44]	1.5×2×50 150 cm³	e-beam-assisted quasi-avalanche discharge	Ne/Xe/HCl 0.989/0.01/0.001 3 atm	e-beam: 0.5 μsec 1 A/cm² 1.1 J discharge: ~ 0.5 μsec 180 A/cm² 6.4 J 0.05 J/cm³ (Total)	0.16 J eff = 2%	3.1	--	--	--
Watanabe, et al.,[45]	3×2.8×30 252 cm³	UV preionized transmission-line-driver	HCl 0.001 Xe 0.003 Ne 5 atm He 3 atm	90 kV 25 nF 101.25 J 0.4 J/cm³	Ne 1.2 J 60-nsec pulse eff = 1.5% He 0.75 J 40-nsec pulse	14 13 12.5	--	--	Quartz
Sze[46]	0.2×0.4×10 0.8 cm³	Corona wire LC inversion stripline	He 0.918 Ne 0.05 Xe 0.03 HCl 0.002 2000 Torr	10 kV 2 nF at 400 Hz E_{in} ~ 0.38 J 0.475 J/cm³	0.65 mJ 5-nsec pulse P ~ 0.5 W at 667 Hz	65	36	5	40%R

These values were used in Eq. (53) to generate the curves shown in Fig. 45. The top curve is for 100% energy transfer from the energy-storage capacitors to the discharge, and the bottom curve is for 70%. Using the available 40% reflectance mirror, the highest peak power which can be reasonably expected is $\sim$ 0.6 MW for the 1-cm^2 beam. The average power and efficiency will depend upon the laser pulse width achieved. For example, for a 40-nsec pulse width, the average power (at 1 kHz) is 24 W and the efficiency 0.40%; whereas for a 100-nsec pulse, the average power is 60 W and the efficiency 0.99%.

The applicability of Eq. (53) to pulsed lasers may be evaluated by calculating the time required for the laser intensity to saturate. The CW theory should be applicable if the laser intensity saturates before the peak in fluorescence. The time to saturation can be calculated from the length L' of the active medium required for saturation, given by

$$I_s = I_0 \exp (g_0 - \alpha_0)L'$$ (56)

where I_0 is the spontaneous emission intensity given by

$$I_0 = \frac{n^*h\nu(A/L^2)(1/4\pi)L}{\tau_{rad}}$$ (57)

with n* being the density of upper-laser-level molecules and A the laser-beam area. For a g_0 of 4%/cm, L' is 295 cm, which requires six passes of the photon flux through the active medium to achieve saturation. Since the optical cavity is 90 cm, the single-pass time is 3 nsec and the time to reach saturation 18 nsec. These times will be compared to the fluorescence time when measured to determine the applicability of Eq. (53) under the present experimental conditions.

The relatively large photoabsorption present in the rare-gas-halide lasers reduces the laser-power extraction efficiency. This can be a serious problem in the case of e-beam-stabilized discharges where it is necessary to operate under conditions of low gain and low specific power to achieve high discharge efficiency and a large enhancement factor. Brau[47] has shown that

102
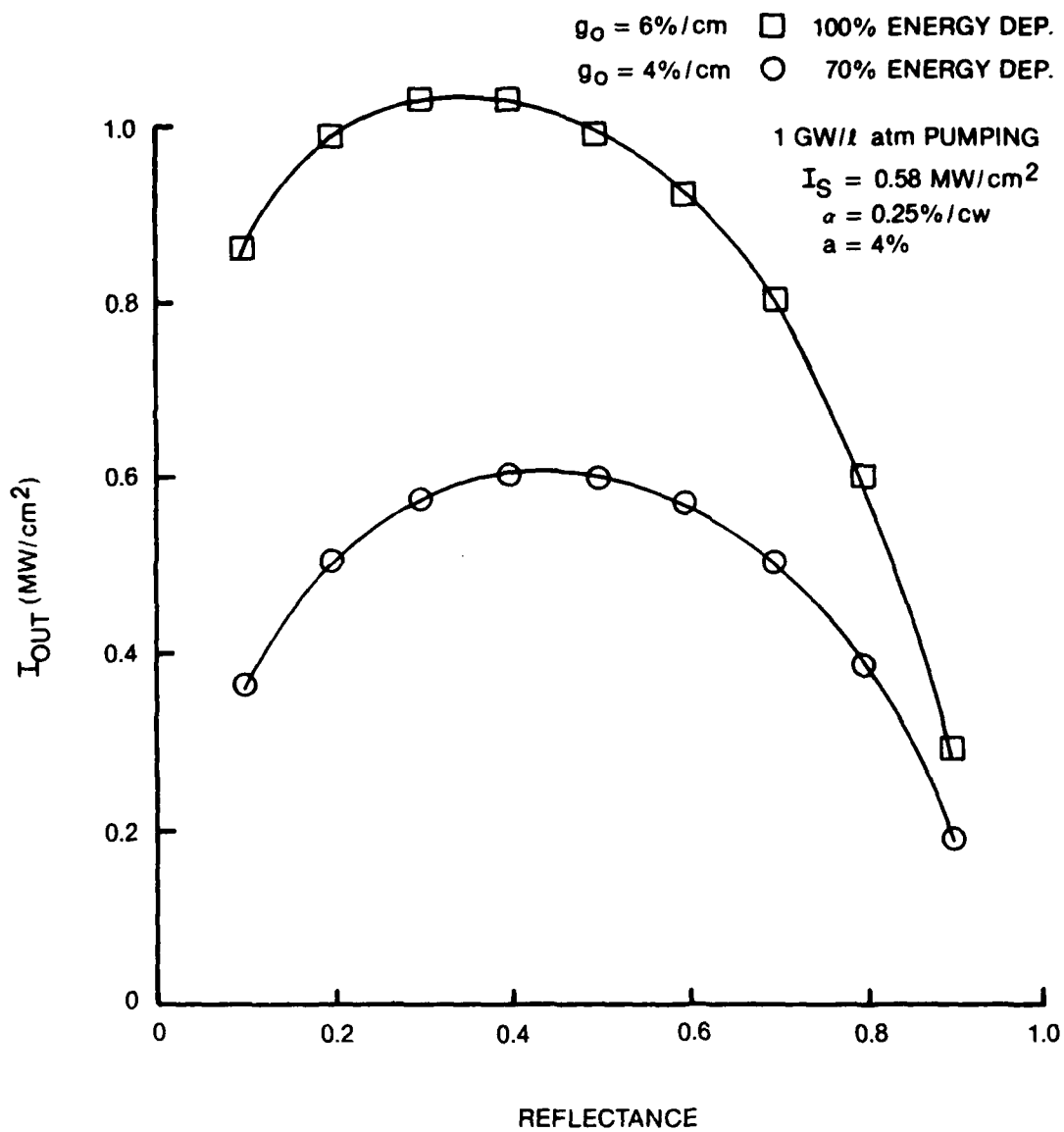
Figure 45. Calculated Dependence of XeCl-Laser-Output Intensity
upon Output-Mirror Reflectance.

the extraction efficiency η_{ex} (defined as the ratio of the photons extracted by the laser flux to the upper-laser-level molecules) is given by

$$\eta_{ex} = \frac{\phi}{\phi_s} \left(\frac{1}{1 + \phi/\phi_s} - \frac{\alpha}{g_0} \right) \tag{58}$$

where ϕ is the laser flux, ϕ_s the saturation flux, and α a parasitic absorption coefficient. Assuming that α is not bleachable (i.e., independent of ϕ), η_{ex} can be maximized with respect to ϕ/ϕ_s to yield

$$\eta_{ex}(max) = 1 - 2\left(\frac{\alpha}{g_0}\right)^{1/2} + \frac{\alpha}{g_0} \tag{59}$$

Figure 46 is a plot of Eq. (59) which shows that g_0/α must be greater than 12 to achieve an extraction efficiency greater than 50%. Further gains in extraction efficiency require increasingly larger values of g_0/α. For the closed-cycle XeCl laser with a gain of 4%/cm, photoabsorption of 0.25%/cm, and a loss of 2%/mirror, the value of g_0/α is 12.1, which results in an extraction efficiency of 51%.

UV-PREIONIZED XeCl-LASER OPERATION

The source of UV preionization was a linear array of small spark discharges located 1 cm behind the screen anode, as depicted in Fig. 47. Basically, 2-56 stainless-steel screws were filed to a point and installed 1 cm apart. A grounded stainless-steel sheet was installed just above the screw points with 1/16-in. holes drilled at each point. Each screw was connected to a 11.5-ft. length of RG58 coaxial cable with the shield grounded. All 49 cables were connected together at the power-source end which was then connected to a thyratron-switched capacitor. In essence, the circuit was a pulsed-charged cable PFN, with each spark source having its own cable.

Other methods such as a sliding spark array were tested; but when He was used as a buffer gas, the preferred arc-path was to the screen anode rather than along the array. The individual-cable method of Fig. 47 produced satisfactory operation in all gas mixtures used.

104
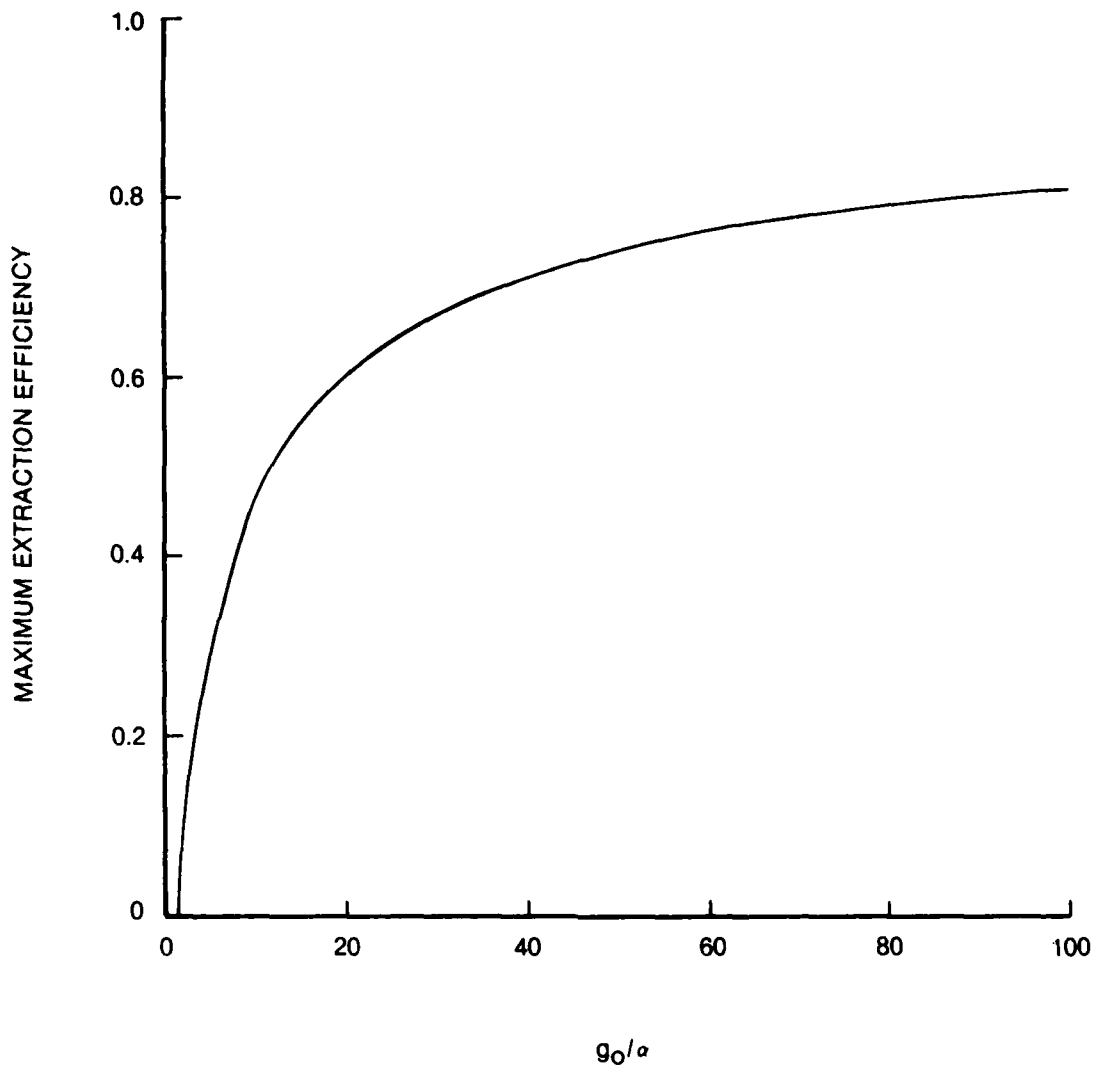
Figure 46. Dependence of Maximum Laser-Extraction Efficiency upon Gain-to-Loss Ratio.
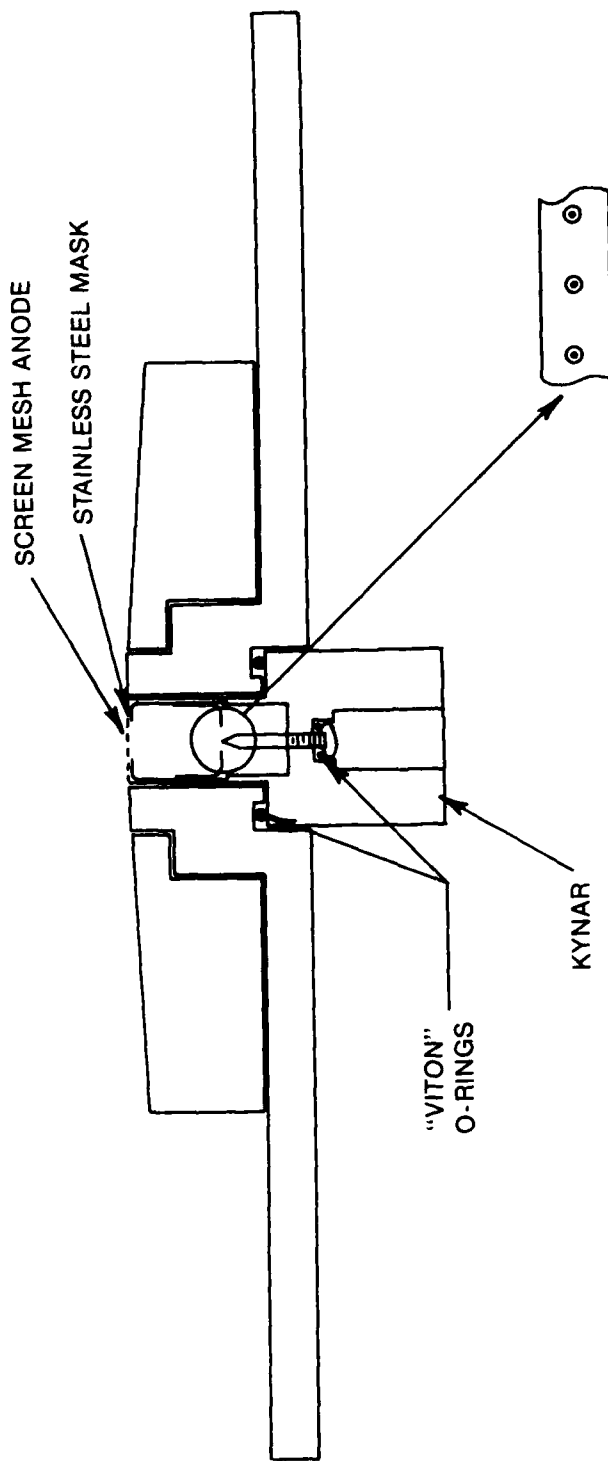
Figure 47. Cross Section of UV Preionization and Screen Anode.

SCREEN MESH ANODE

STAINLESS STEEL MASK

KYNAR

"VITON" O-RINGS

The UV output did not appear to be affected by variations in repetition rate. The actual preionization mechanism was not investigated in detail during this effort although one would expect strong ionizing radiation at the He 58.4-nm resonance line and two-step ionization caused by the H 121.6-nm Lyman-α as well as some contribution of Cl radiation at $\sim$ 101, 107, and 139 nm.

Initial checkout of the system was performed in 1 atm of He. After several hours of discharge operation over a period of about one week, discharge uniformity deteriorated. Also, it appeared that material had been deposited on the system windows. Discharge operation at voltages above 12 kV resulted in sparking at the edges of the cathode and diffuse discharges from these edges to the screen anode. For these reasons, the discharge section of the closed-cycle laser was removed from the system.

Upon disassembly, thin white coatings were observed on regions of the stainless-steel electrodes. Although these coatings were too thin to permit collection of samples, they could be easily removed by slight rubbing. The coatings were partially soluble in water and insoluble in organic solvents (acetone, ethanol, and benzene). Other regions of the stainless-steel return loop appeared to have undergone slight surface changes; this was manifested by an increase in the light dispersion by the surface and also by oxidized regions (after exposure to air) in the vicinity of some of the welds. Samples could neither be scraped off these walls nor removed by solvents, including water. Finally, color changes were noted in the copper gaskets on the regions exposed to the circulating gas. Fogging of the Pyrex windows proved to be a permanent etching of the inner surface, which reduced the light transmittance. Analysis by mass spectrometry of a gas sample obtained from the system several days after discharge operation showed the following species: He, N_2, O_2, H_2O, CO_2, and Ar. The N_2/O_2 ratio and the relative abundance of CO_2 and Ar were consistent with air contamination introduced during sample collection or initial introduction of the gas into the laser. The gas analysis failed to identify a primary cause of the observed changes; however, the absence of any large organic molecules was significant. Etching of the Pyrex presumably occurred by reaction with hydrogen fluoride

$$SiO_2 + 4HF \rightarrow SiF_4 + 2H_2O$$
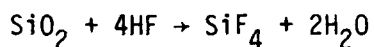
The presence of HF could also explain the cleaning of the copper gaskets and the slight attack of the steel surfaces. In the region of preionization or discharge, free F atoms could produce protective fluoride layers on the electrode. The white coatings on the electrode and screen are probably iron (II) fluoride, FeF_2. When the screen was cleaned with a wet cloth, a green stain appeared on the cloth, most likely arising from the green-blue octahydrate of FeF_2.

Two possible sources of F may contribute to the production of HF within the preionization or discharge regions. These are the perfluorinated ester fluid in the Ferrofluidics feedthrough [perfluoro bis (2-ethylhexyl)azelate] and the insulator used in the preionization mount, Kynar [polyvinylidene fluoride].

Production HF from Kynar must be considered a strong possibility for several reasons. First, H and F are located on α carbons and, thus, HF production is not sterically hindered; second, the predominant volatile product from thermal degradation of Kynar is HF; and, finally, radiation of fluorinated polymers tends to produce HF. The production of HF from Kynar during UV irradiation has not been addressed in Pennwalt literature.

A small chamber was fabricated from Kynar and connected to a mass spectrometer; two sharpened 0.03-in. W rods served as electrodes. Helium gas (99.9999%) was introduced into the chamber, and a 0.03-in. hole permitted the He and discharge products to enter the vacuum system and subsequently be detected by mass spectrometry. The background pressure of the vacuum system was 2×10^{-7} Torr; at He flow rates sufficient to produce a nominal pressure in excess of 3×10^{-5} Torr, a discharge was induced at 2 kV. Operation was maintained at 1 Hz and the electron-impact mass spectrum of evolved gases monitored. HF was the major product observed in this experiment. Individual ions were monitored continuously during the pulsed discharge. A series of ions showed some enhancement; these were m/e 19, 20, 26, 28, and 44. Hydrogen fluoride at m/e 20 showed the most pronounced enhancement. At least one ion, m/e 32, decreased during the discharge. The magnitude of the

intensity changes induced by the discharge varied from day to day and, in general, decreased with continued operation. It could not be determined whether this was due to reduced intensity of the discharge or to alterations in the Kynar surface characteristics. It was beyond the scope of this study to investigate all of these effects; however, it was clear that HF can be produced in a He discharge and that Kynar is the most likely precursor to the observed HF.

Subsequent to the tests, close examination of the Kynar surfaces indicated extensive charring at the electrode-Kynar surface. The He flow through the cell was 0.08 SCC/sec, with a total He pressure of $\sim$ 1 Torr within the cell. It is clear from this He pressure and physical changes in the cell that a discharge rather than the desired spark was generated. The possible location of Kynar within the discharge may account for the degradation which yields HF. The precise mechanism of HF generation (10^{-7}-Torr HF pressure) is not known. Discussions with the manufacturer (Pennwalt) revealed the fact that Kynar is readily degraded by electron bombardment, yielding HF. The manufacturer insists, however, that the amount of HF generated by UV degradation would be below detectable limits.

Figure 48 shows typical waveforms of the discharge gap voltage, E/N, and current as well as on-axis fluorescence and laser output. The fluorescence was obtained after turning the total reflector away from the cavity-alignment position. The current waveform was corrected by the method described earlier, and the E/N is calculated by removing the effect of the 6-nH head inductance. As previously mentioned, the current-probe correction scheme has not yet been fully resolved, and the voltage monitor circuit showed some inaccuracies for risetimes of $\leq$ 10 nsec. Therefore, the small bumps and wiggles are probably artifacts of the monitors. Also, reflections within the long lines can be expected to cause additional errors $\simeq$ 100 nsec after a large pulse, rendering the low-voltage and low-current tails unusable. Obviously, positive current cannot exist at negative E/N, as shown for a portion of the tail.

The fluorescence and laser pulse both appear $\simeq$ 15 nsec after the current peak, under the gas-mixture conditions of Fig. 48. This is generally the
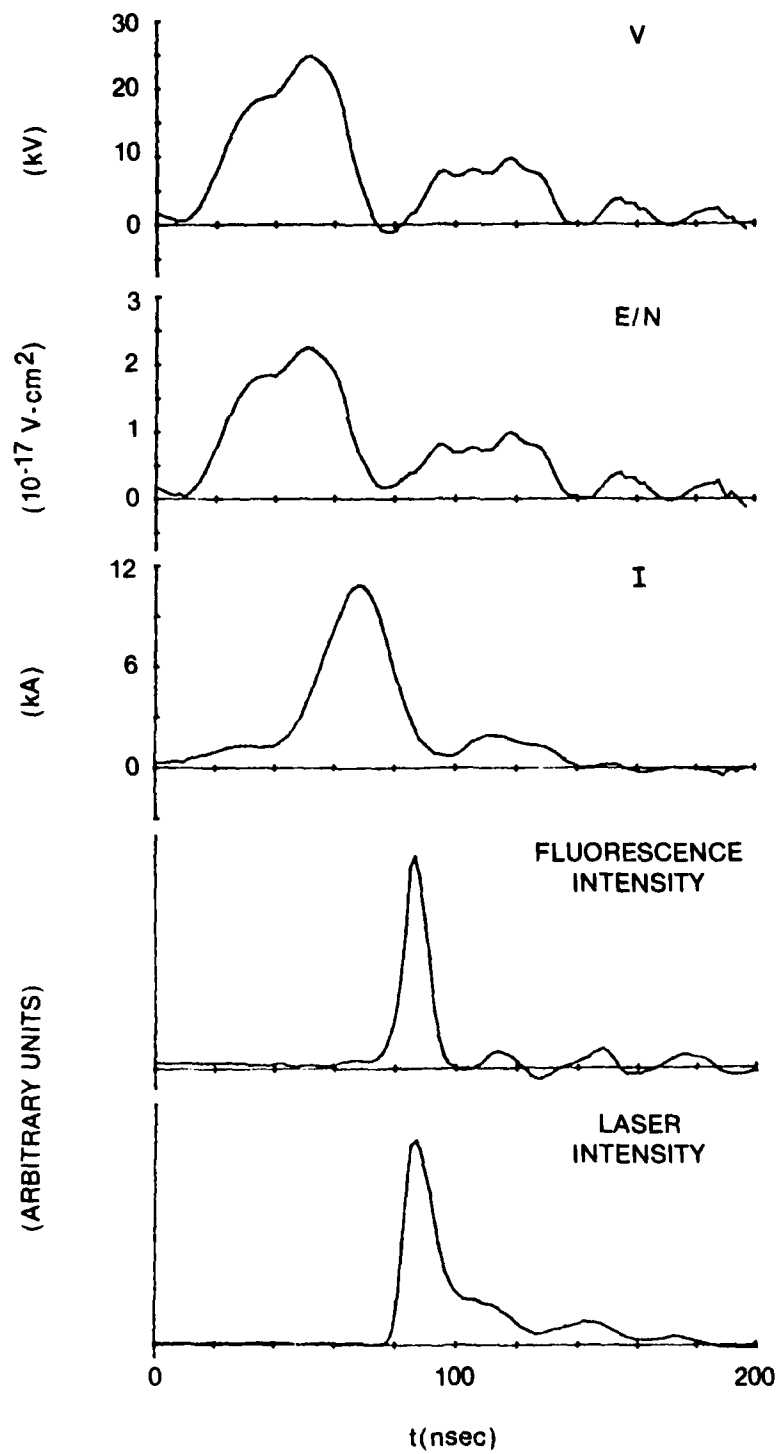
Figure 48. Electrical and Optical Waveforms of UV-Preionized
XeCl Laser for 0.67% Xe/0.13% HCl in He.

case except for mixtures lean in HCl. Figure 49 shows the additional delay in lasing onset when the HCl concentration is reduced to 0.03%, instead of the 0.13% of the total gas mixture of Fig. 48.

On-axis fluorescence spectra of the XeCl discharge were obtained by focusing the end-on fluorescence output of the discharge onto a 200-μ quartz fiber-optic probe which was used to transmit the output to a 0.5-m Jarrell-Ash monochromator in a screen room. With the discharge operating at a rep rate of 5 Hz, spectra were obtained both during the discharge current pulse and during the discharge afterglow by proper positioning of the 20-nsec gate of a PAR Model 160 Boxcar. In Fig. 50 the experimental band intensities are compared with Franck-Condon factors (FCF) calculated[49] for transitions from the zero vibrational level of the $B^2\Sigma_\pi^+$ upper state to several levels of the $X^2\Sigma_\pi^+$ ground state of $Xe^{35}Cl$. The band intensities during the discharge agree fairly well with the FCF data. During the afterglow, there is an enhancement of the 0-1 and 0-2 band intensities above the FCF values--the bands for which lasing was observed at 3079.61 and 3082.10 Å in the present experiment. The enhancement of the bands during the afterglow is due to stimulated emission.

In order to determine the optimum gas mixture for the XeCl laser, the partial pressures of Xe and HCl were varied; and measurements of discharge current and voltage, fluorescence and laser pulse shape, and average laser output power were made. The effect of Xe and HCl partial-pressure changes upon discharge current is shown in Fig. 51. The horizontal bar on the main current pulse indicates the 9-kA current level. The discharge impedance tends to decrease with decreasing HCl concentration and with increasing Xe concentration. The extreme sensitivity of the discharge current pulse to HCl concentration is striking. An increase in HCl concentration from 0.033 to 0.133% reduced the magnitude of the secondary current pulse from 3 kA to 1 kA. Laser pulse width increased slightly with decreasing HCl and with increasing Xe concentration. Average laser output power also increased with decreasing HCl and with increasing Xe concentration.

A decrease in energy/pulse of only $\sim$ 10% was seen as rep rate was increased to 700 Hz. Figure 52 shows this for a non-optimum He/Xe/HCl mixture. The

111
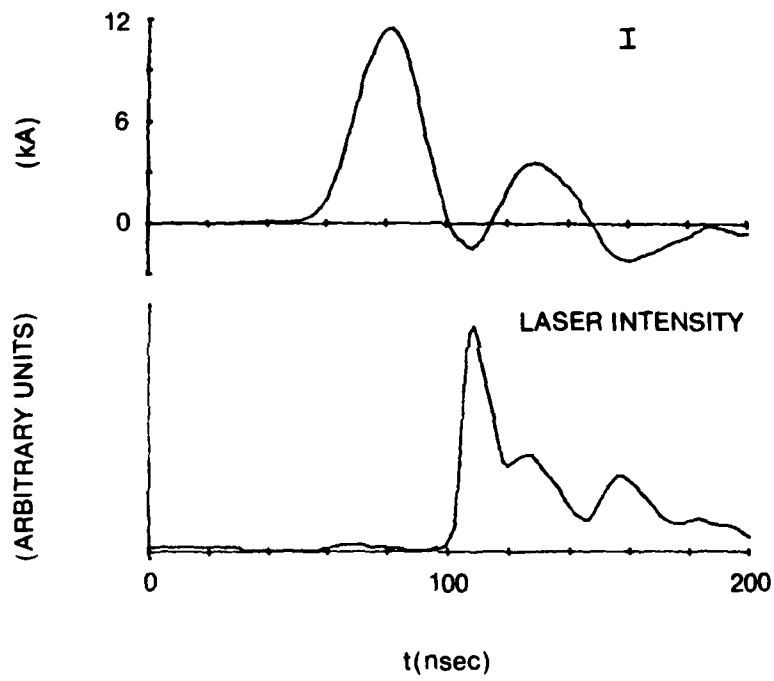
Figure 49. Discharge Current and Laser Waveforms of UV-Preionized
XeCl Laser for 0.67% Xe/0.03% HCl in He.
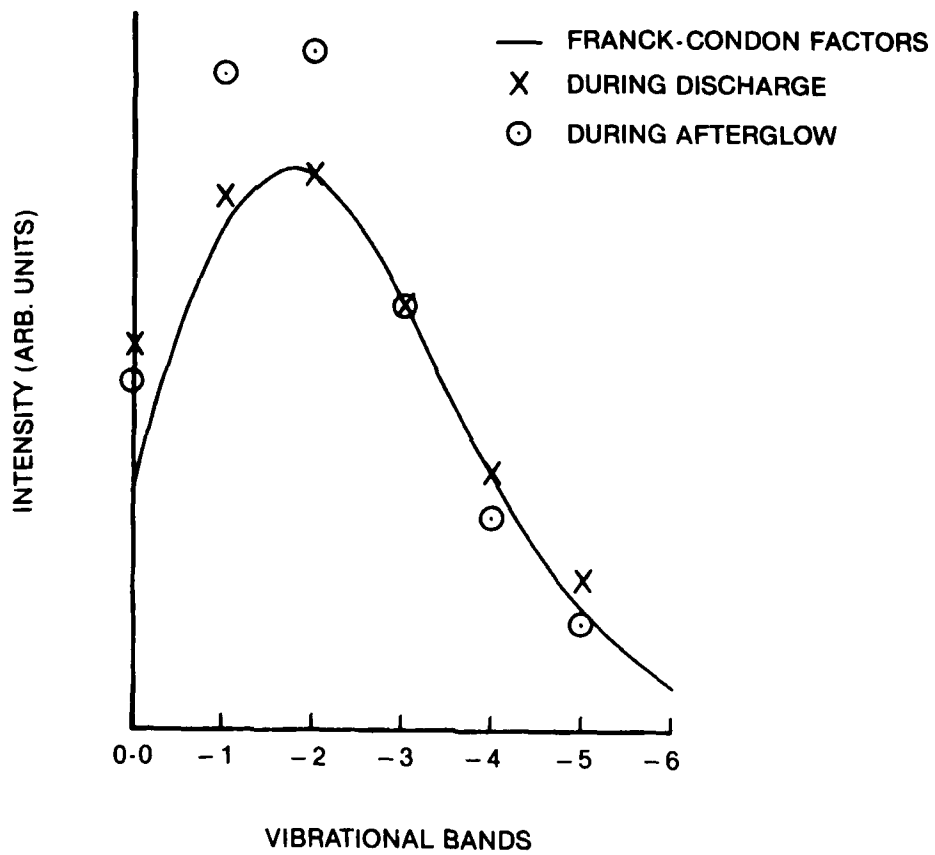
Figure 50. Band Intensities and Franck-Condon Factors for XeCl.

1500 TORR
He/Xe/HCl
10 nF AT 30 kV

TORR HCl

0.5

Xe
5 TORR

1.0

2.0

TORR Xe

10

HCl
1 TORR

5

2

20 nsec
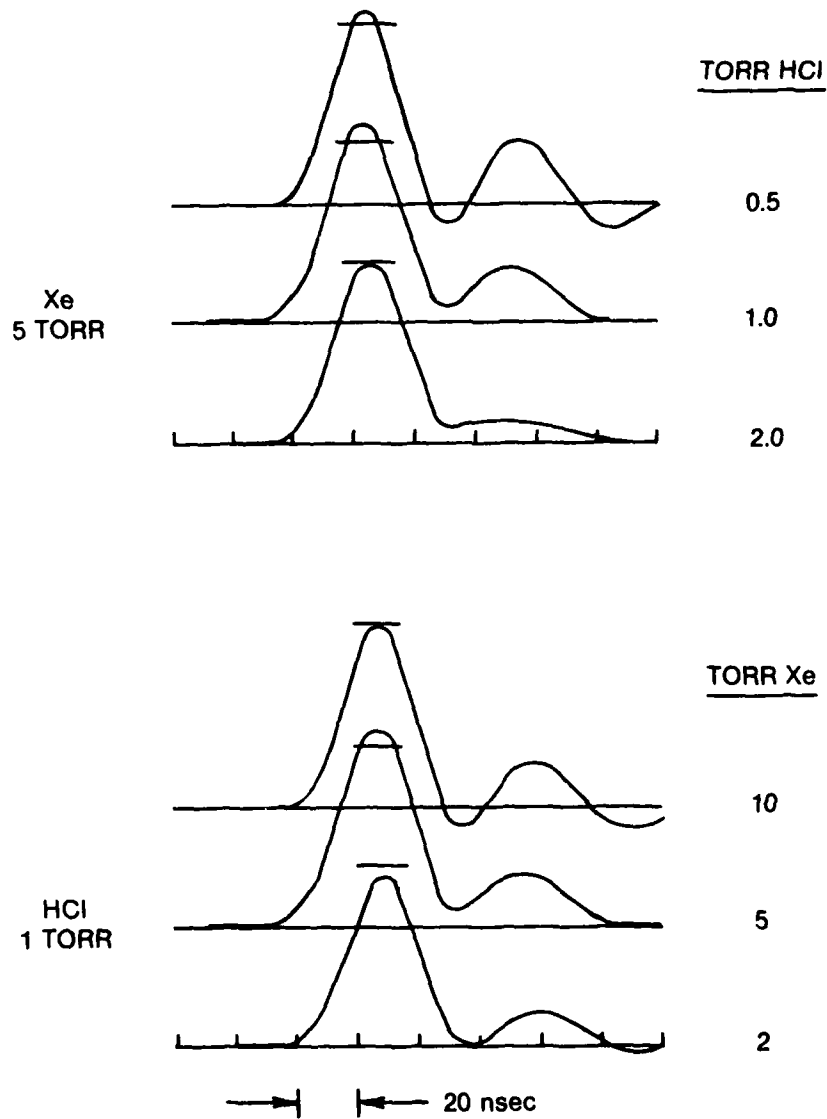
Figure 51. Variation of Discharge-Current Pulse Shape with
HCl and Xe Partial Pressure.

114
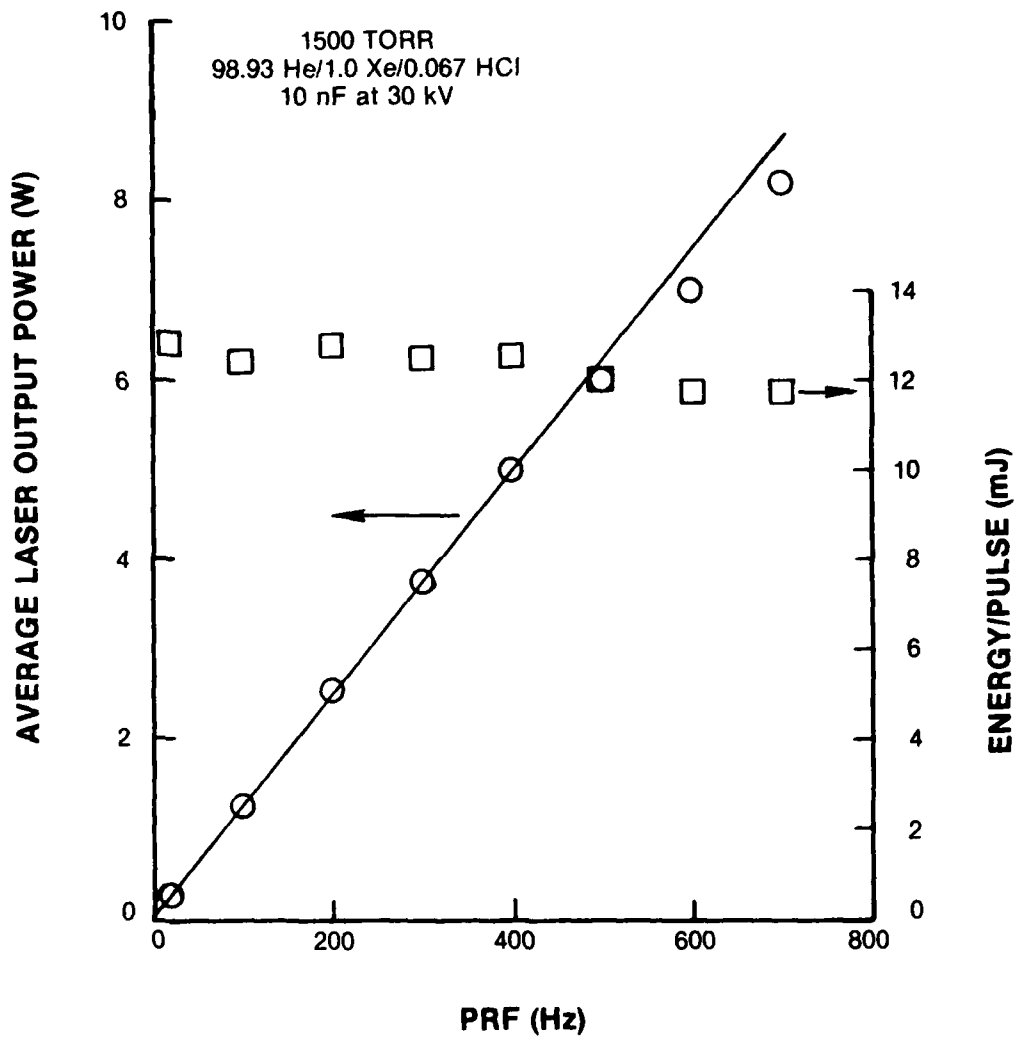
Figure 52. Dependence of XeCl Laser Output Upon Repetition Rate.

115

largest energy/pulse achieved for the UV preionized laser was 24 mJ in a mixture of 10-Torr Xe/1-Torr HCl in He at a total pressure of 1500 Torr. The charging voltage was 30 kV, and a 65% R/32% T partial transmitter was used as an outcoupler. Maximum gas pressure was limited to 2 atm by the Ferrofluidic seal. Inconsistencies were apparent in some of the data obtained. Upon disassembly on several occasions, a coating was found to be present on the cavity mirrors.

After installation of a new total reflector and a clean AR-coated window on the laser, the data of Fig. 53 were obtained in order to determine the optimum gas-mixture ratio. Data were initially taken for gas mixtures containing 1 Torr of HCl. A maximum laser output of 24 mJ was obtained for Xe partial pressures of 10-15 Torr. The increased output was presumed to be a result of cleaning the cavity optics. Nine days after the clean optics were first exposed to laser mixtures, the curves for 0.5 and 2 Torr of HCl were obtained. On the tenth day after the initial gas fill, a laser output of 14 mJ (black circle in Fig. 53) was measured for a mixture containing 12 Torr of Xe and 1 Torr of HCl. This 42% reduction in laser output over a period of 10 days was probably due to coating of the cavity optics. The deterioration of the cavity optics also depressed the level of of the 0.5- and 2-Torr-HCl curves in Fig. 53.

As discussed earlier, the most probable cause of the generated impurities was UV or electron bombardment of the Kynar insulator. Consequently, studies of the UV-preionized laser were terminated in favor of x-ray pre-ionization.

X-RAY-PREIONIZED XeCl-LASER OPERATION

X-rays for preionization were produced by impingement of 50-100 keV electrons from a WIP[50] (Wire-Initiated Plasma) e-beam gun upon 0.0003-in.-thick tantalum foil. The emerging x-rays were attenuated by an adjustable mask of 0.03-in.-thick Ta to produce an x-ray beam 40 cm long by 0.6 cm wide in the discharge region. The effect of this beam was to generate sufficient electron-ion pairs to define the discharge area as the preionization area.

1500 TORR
He/Xe/HCl
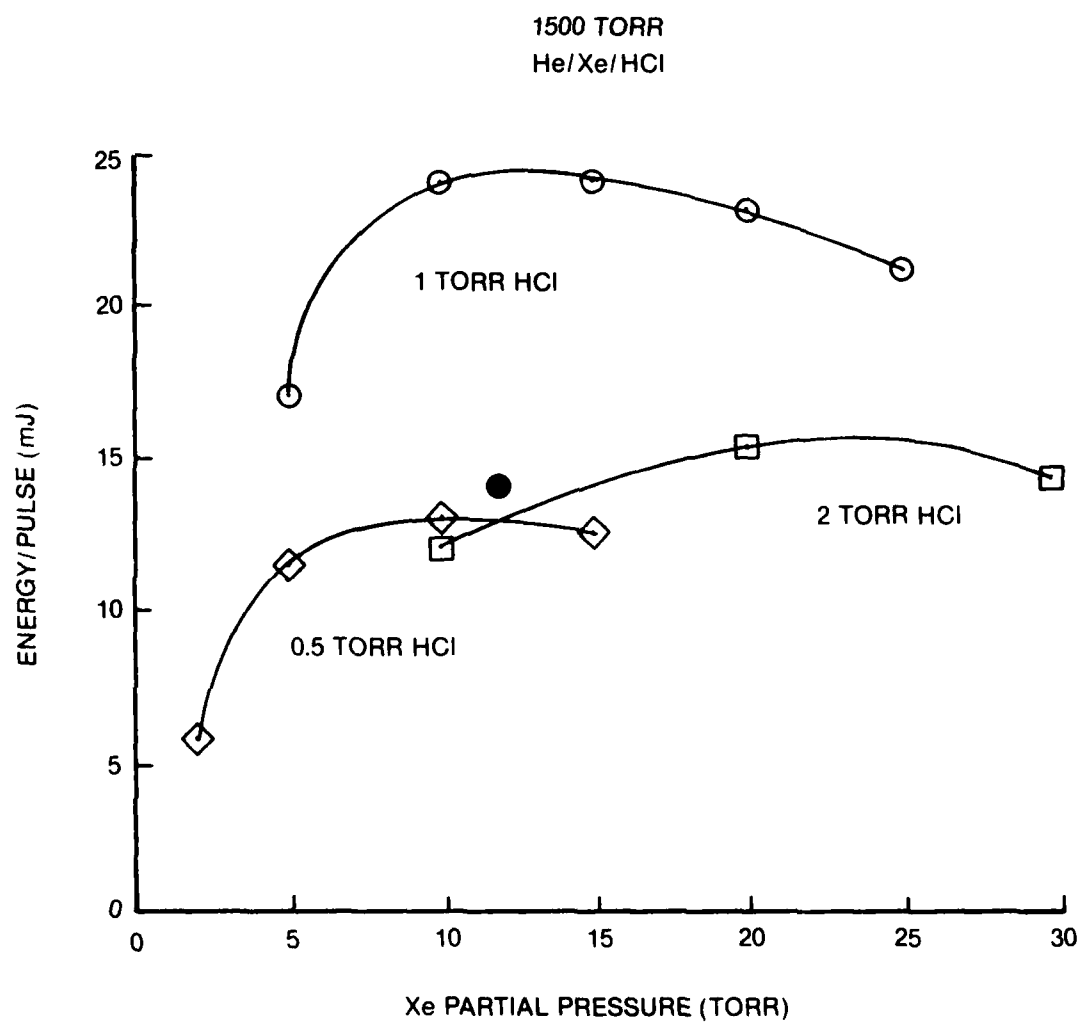
Figure 53. XeCl-Laser-Output Dependence Upon Partial Pressures of Xe and HCl.

117

Figure 54 shows the anode assembly and adapter plate which replaced the UV-preionization anode assembly. The greatest advantage of this method over the UV precursor arrangement is the absence of the Kynar insulator. Also, the stainless-steel screen anode is no longer needed; the anode is now continuous with the flow ramps and connecting flange. The entire anode assembly is constructed of aluminum and coated with $\approx$ 0.0005-in. Ni using an electroless plating process. The only uncoated portion was the underside of the 0.050 in. thick anode; this was done in order to minimize x-ray attenuation in this area. A slow flow of He is maintained between the Ta foil and the anode in order to purge this region of O_2 and other x-ray absorbing species and also to help remove foil heat. The adaptor plate and e-gun assembly are water-cooled.

Nine metals, including one alloy (Ta/W), were compared for best possible application as an e-beam absorber/x-ray source. Several factors such as the minimum thickness required to fully attenuate the e-beam, efficiency of x-ray production, mechanical strength at room and elevated temperature, thermal conductivity, chemical reactivity, cost, availability, and x-ray transmission can be compared for each metal. Although the Ta/2.5% W alloy exhibits the best x-ray production efficiency and excellent high-temperature strength, its extremely high cost and relative unavailability preclude it from serious consideration. Ta (0.0003-in.) was chosen since it satisfied most of the performance criteria. If mechanical properties at elevated temperatures had become a problem, 0.001 Mo would have been the next choice. Although Mo has high scores in almost all the criteria for this application, its major drawback is related to the fact that the x-ray production efficiency is approximately a factor of two lower than that for Ta.

Figure 55 shows preliminary calculations for several combinations of transmission windows and for 1% Xe in He, Ne, and Ar. Due to the very low absorption of x-rays by He and Ne, the curves for 1% Xe in He and Ne have approximately the same shape, determined principally by the presence of Xe. Argon has a much larger absorption coefficient for x-rays, and clearly there is a corresponding increase in the overall usage of the x-rays. For He and Ne mixtures with Xe, neglecting other losses, there is only 0.1 - 0.2% probability for x-ray utilization over a wide energy range. For a 100-kV
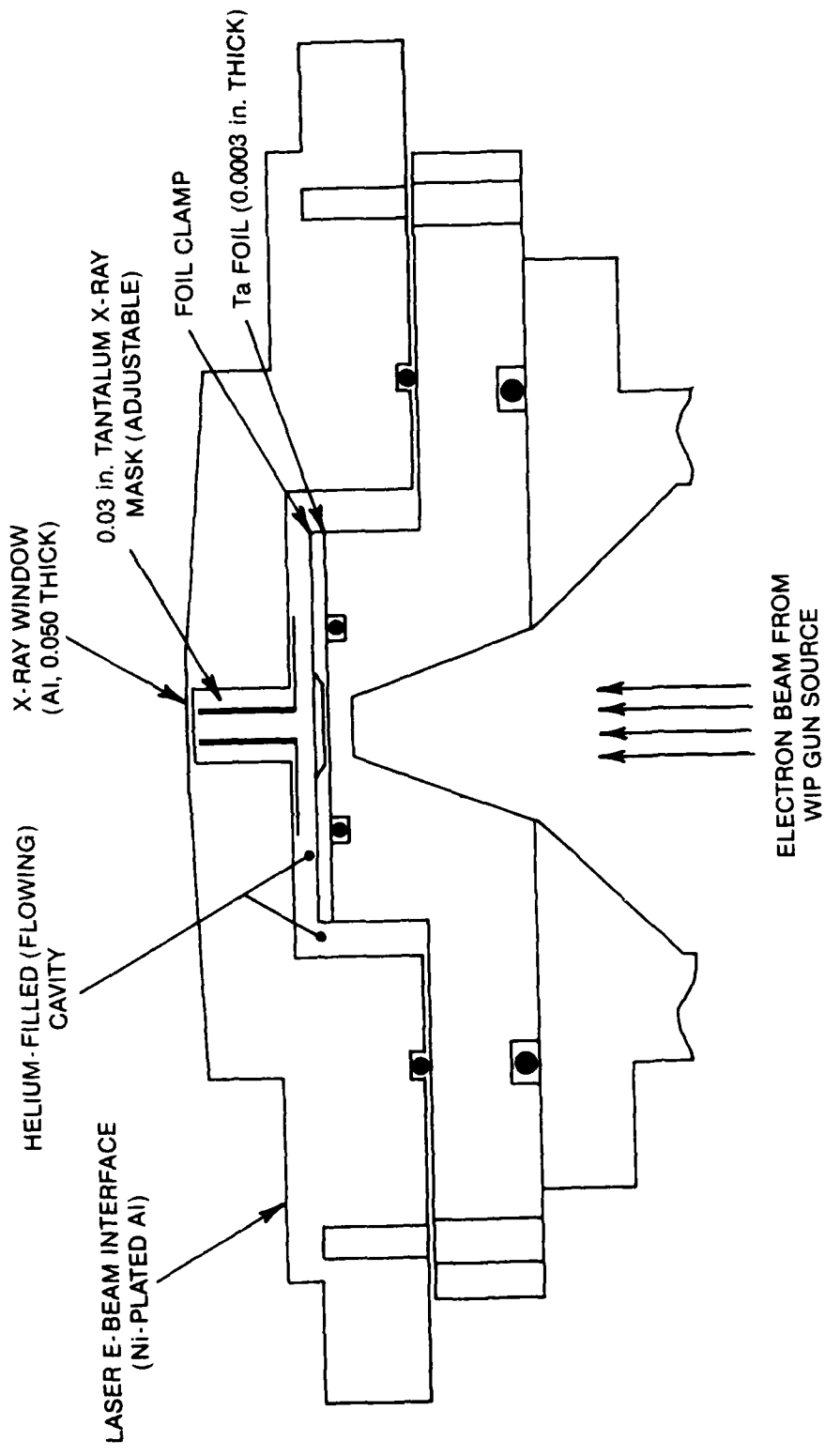
Figure 54. Schematic Diagram of Anode Assembly for X-Ray-Preionized XeCl Laser.

119
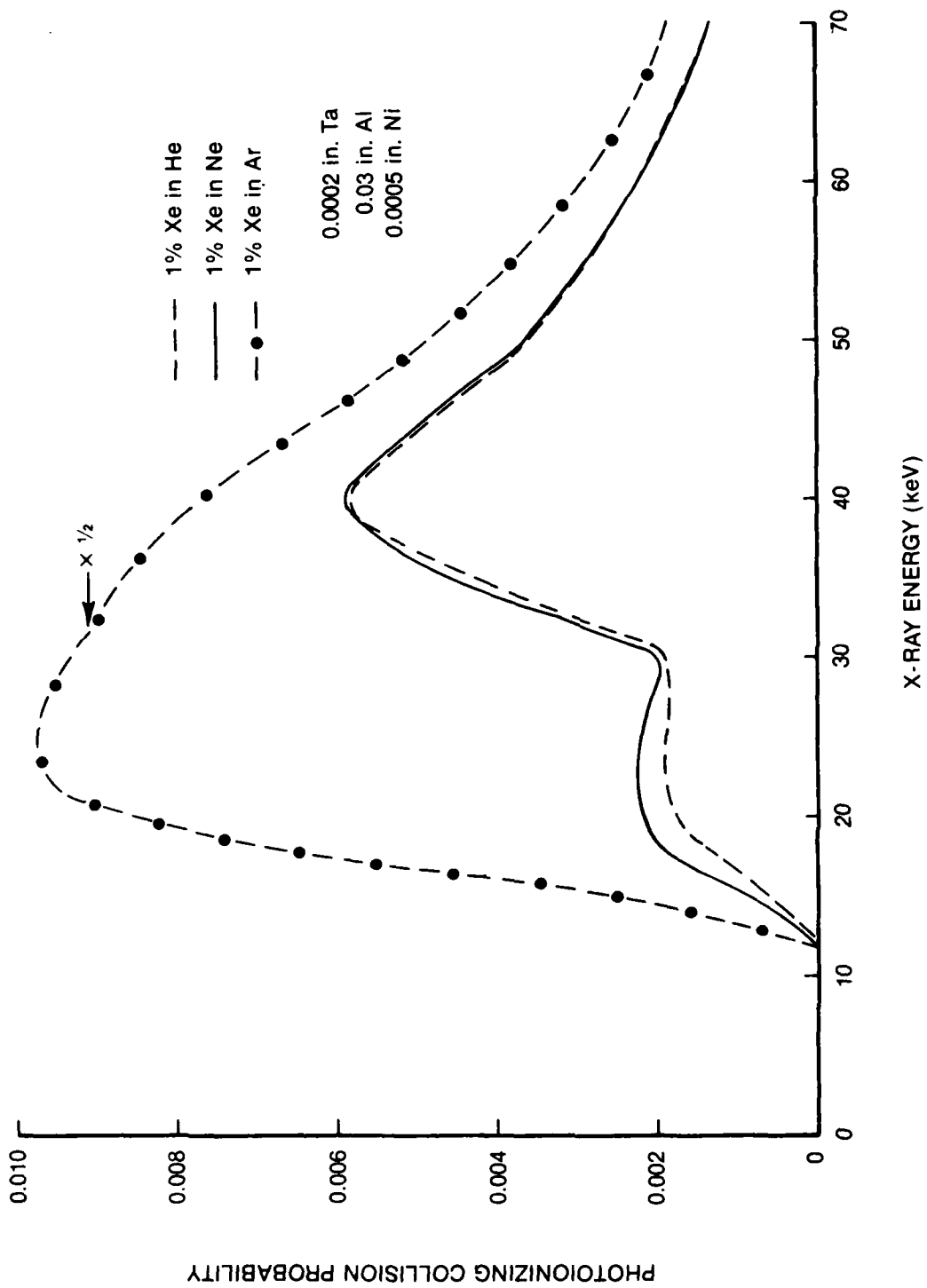
Figure 55.   Probability of X-Rays Penetrating Metal Windows and Undergoing
Absorption by Laser Gas Mixture Plotted as Function of X-Ray Energy.

120

e-beam impact on Ta, the resultant x-rays are essentially a continuum of Bremsstrahlung from 0 to 100 keV, with a maximum in the vicinity of 70 keV.

Based upon data provided by Hughes for the e-beam, the maximum current of electrons at the foil is 5 A-cm^{-2}. Under severe surface conditions, the efficiency of secondary electron generation by the Mo cathode may be reduced. Consider in the following that the overall current is conservatively 1 A-cm^{-2}, i.e., 6×10^{18} electrons sec.$^{-1}$ cm^{-2}. The x-ray production efficiency by Ta for a 100-kV electron is $\sim 1\%$, indicating 6×10^{16} x-ray photons sec.$^{-1}$ generated isotropically in all directions by 1 cm^2 of foil. Considering that only a width of 0.5 cm is accepted at a distance of 2 cm, then the number of x-rays entering the solid angle is $\sim 10^{15}$ cm^{-2} sec^{-1}. Further, consider a pulse width of 500 nsec. In the absence of x-ray absorption, $\sim 5 \times 10^8$ x-ray photons will pass through the 2-cm discharge path length. Estimating from Fig. 55 that the probability of an absorption event over a wide range is ~ 0.0015, then there will be $\sim 7.5 \times 10^5$ absorptions sec.$^{-1}$. Estimating that the most probable x-ray absorbed will be ~ 50 keV, each absorption event will produce 1670 ion pairs (assuming 30 eV per ion pair). Overall, $> 10^9$ ion pairs cm^{-3} sec is estimated. These rough calculations indicate that sufficient pair production can be generated, despite rather inefficient x-ray utilization.

Initially, a Velonex model 350 pulse generator was used to modulate the wire-initiated discharge of the WIP e-gun. However, the e-beam flux proved to be insufficient; therefore, a thyratron-switched, capacitor-transfer circuit was implemented. This is shown in Fig. 56. The 1:1 inverting transformer, consisting of 13 turns of twisted pair wound on a stack of four ferrite cores, provides a positive 4-kV output for ~ 2 μsec (open circuit) before core saturation occurs. The capacitor-charging current is sufficient for core reset. Resistors R_1 and R_2 function as isolating elements between the fast pulser and relatively low impedance coaxial cables. The diodes isolate the bias and pulse circuitry from each other.

It was hoped that this high-speed circuit would effect a high-intensity, short-time-duration x-ray pulse by providing a fast, high-voltage pulse to the e-gun wire. Desired performance was never fully achieved. With up
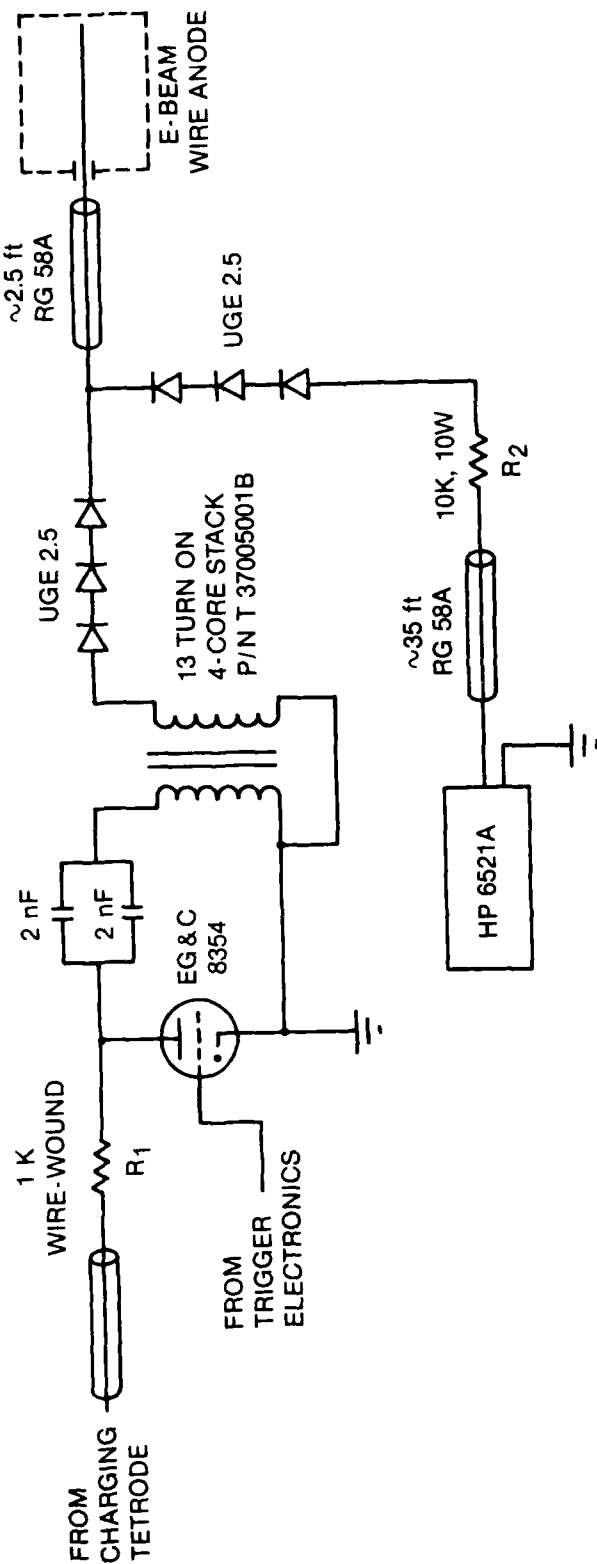
Figure 56. Schematic Diagram of the Thyratron-Switched, WIP-Gun Grid Bias and Pulse Circuit.

122

to 5 kV on the wire, a delay of $\sim$ 800 nsec exists between application of the pulse and wire breakdown. The pulse width is limited by the circuit inductance (primarily transformer) and storage capacitance. For the values shown in Fig. 56, a sinusoidal current pulse (positive half cycle) of $\sim$ 800 nsec at a peak current of $\sim$ 30 amps is obtained. Also, a high-frequency oscillation ($\sim$ 150-nsec period) is present on the wire. This appears to be the interaction of the wire-plasma breakdown characteristics with circuit stray inductance or capacitance. However, it is unlikely that the high frequency affects the main-laser discharge characteristics.

The x-ray-preionized XeCl laser was initially operated with a gas mixture of 0.067 HCl/1 Xe/98.93 He at a pressure of 1500 Torr. The optical cavity (internal mirrors) was comprised of a 5-m total reflector and a 40% R flat partial transmitter. A maximum laser output of 18 mJ was achieved at a charging voltage of 30 kV, a rep rate of 5 Hz, an e-beam voltage of 105 kV, and a WIP-gun modulating voltage of 7 kV. A delay of $\sim$ 200 nsec in discharge breakdown with respect to the peak of the WIP-gun modulating current was found to be optimum. Replacing the 40% R mirror with a 65% R mirror reduced the laser output to 14 mJ. This should be compared with the 24-mJ output obtained using UV preionization.

The dependence of the XeCl laser output upon discharge current, e-beam (or maximum x-ray) energy, and WIP-gun modulating current is shown in Fig. 57 for a 1500-Torr 0.13 HCl/1 Xe/98.87 He gas mixture. Although there is no saturation in laser output with increasing discharge current, there does appear to be a saturation of discharge current with increasing charging voltage.

The reason for the strong dependence of the laser output upon e-beam voltage is not known. This could indicate insufficient x-ray intensity, at low e-beam voltage, for adequate preionization. The bremsstrahlung intensity is given approximately by

$$I = AZiV^2$$

0.13 HCl/ 1 Xe/98.87 He
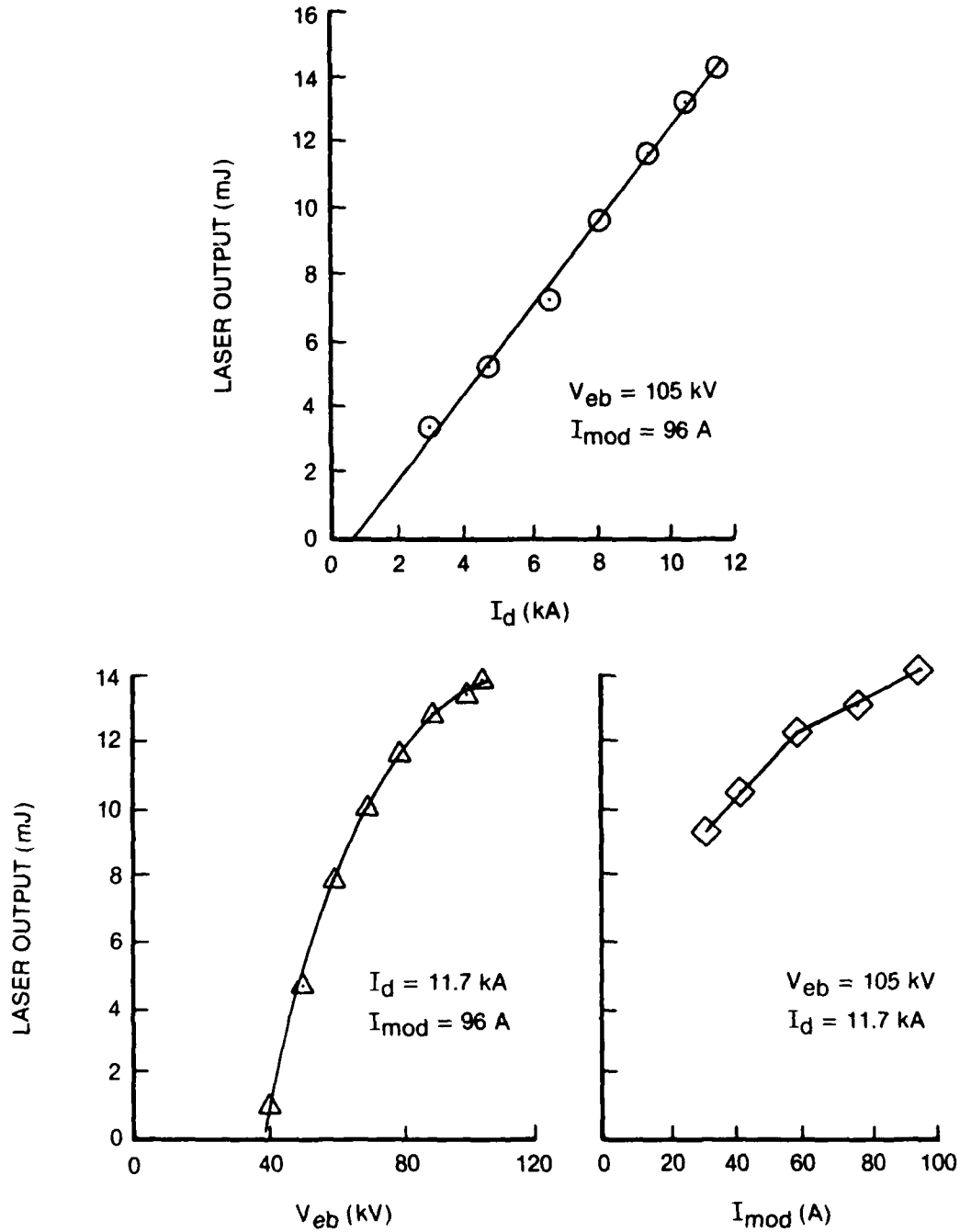
Figure 57. Dependence of XeCl Laser Output Upon Discharge Current (I_d), e-Beam Energy (V_{eb}), and WIP-Gun Modulating Current (I_{mod}).

124

where A is a constant, Z the atomic number of the target, i the e-beam current (which varies as $V^{3/2}$), and V the e-beam voltage. The bremsstrahlung available for preionization is attenuated by the Ni-coated Al window and, therefore, has an intensity which varies as $V^3 e^{-\mu X}$, where μ is the energy-dependent total linear attenuation coefficient and X the window thickness. If this strong dependence of x-ray intensity upon e-beam voltage is the cause of the observed variation of laser output with e-beam voltage, it would indicate that operation of the e-beam at $\sim$ 100 kV is necessary to provide the minimum x-ray flux for effective preionization. Operation at lower voltage would be possible at higher current levels.

The WIP-gun cathode current was measured using a Pearson 110A current monitor which was installed on the coaxial high-voltage line feeding the gun. The dependence of the cathode current on anode-wire current and e-beam voltage is shown in Fig. 58. A maximum cathode current of 3 A was obtained at a helium pressure of 50 μ, e-beam voltage of 120 kV, and modulating current of 130 A. Assuming an output e-beam area of 40 cm^2, the cathode current density was 75 mA/cm^2. This value is more than one order of magnitude less than the 1 A/cm^2 which the gun supposedly generated in initial testing. At that time, a low-inductance pulser (spark-gap-switched) in close proximity to the wire anode was required to generate wire-anode currents of hundreds of amps. However, an extrapolation of the plot in Fig. 58(a) to e-beam current densities of $\sim$ 1 A/cm^2 indicates that anode-wire currents of several thousand amps are required.

The plots in Fig. 58(b) show that operation at higher He pressure results in higher cathode current. Operation above 50 μ was precluded by arc-over in the WIP gun. The data indicated by x's on the 20-μ plot were obtained by H. Gallagher[51] (Hughes Research Laboratory) for a similar WIP gun operating at 15 μ and an anode wire current of 14.5 A. The gun has a 4 × 25 cm window. Gallagher's data (reduced by a factor of 10) display the same dependence of cathode current on wire-anode current as our own. In Gallagher's opinion, the cathode current is mainly determined by the geometry of the ion-extraction grid and is relatively insensitive to cathode conditions and gas used.
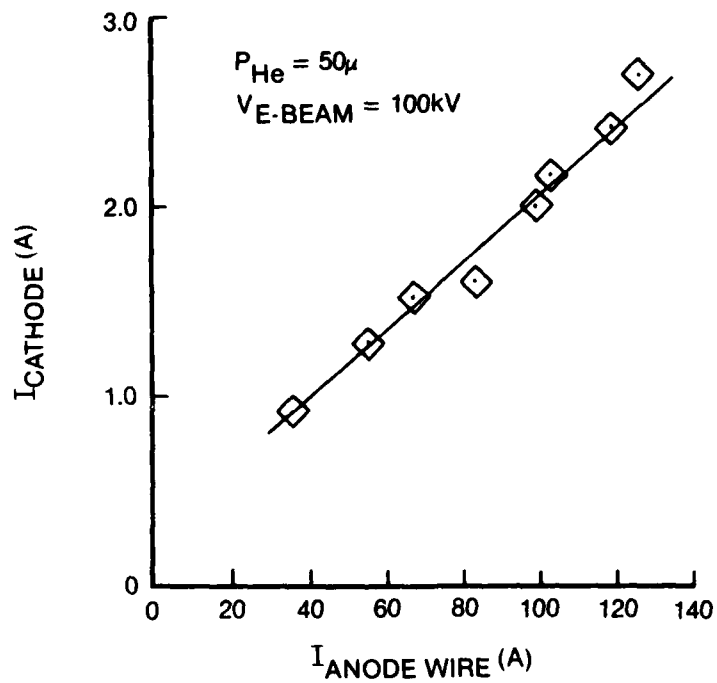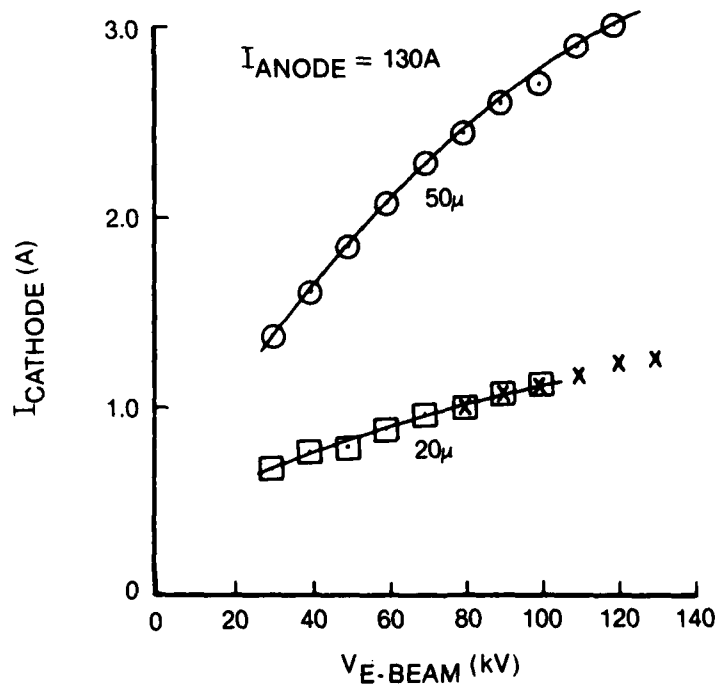
Figure 58. Dependence of WIP-Gun Cathode Current upon a) Anode-Wire Current and b) e-Beam Voltage.

The XeCl laser system has been operated at repetition rates up to 1.5 kHz. Figures 59 and 60 show the laser output as a function of rep rate at two different power levels for a 1500-Torr 0.13 HCl/1.0 Xe/98.87 He mixture. The power roll-off with rep rate is much more pronounced at the higher power level, lending credibility to the argument that acoustic disturbances affect the performance of a high-rep rate XeCl laser. The limiting repetition rate of 1.5 kHz was determined by the charging system, not the discharge behavior. Higher rep rates should be achievable.

The poor laser efficiency ($\sim 0.35\%$) is attributed to the PFN configuration as well as the seemingly limited pre-ionization level. A stripline PFN configuration was constructed and used for a short time, but stray inductance proved to be too large for successful operation.

It is interesting to note that the mixture employed for the data of Figs. 59 and 60, was used for approximately two months, with no degradation being observed. It appears that contamination of the optics--which was encountered when UV pre-ionization was employed--does not seem to exist at a significant level in the x-ray preionized system. A decrease in laser output, however, does seem to correlate with the gas temperature. After operation for ~ 2 min. at rep rates above 1 kHz, the gas pressure increased ~ 20 Torr, corresponding to $\sim 1.6\%$ increase in temperature. The previously obtained output power at 100 Hz could not be achieved ($\sim 10\%$ low) until the gas was allowed to cool to near its original temperature. This effect may merely represent the change in alignment of the cavity mirrors caused by the pressure change and may also be a partial cause for the roll-off in the power shown in Figs. 59 and 60. This issue was never fully resolved.

At high rep rate and high voltage ($\gtrsim 25$ kV), corona appears on the the charging-system high-voltage connectors as well as on the high-voltage probe used for charge-level monitoring. Techniques for correcting this condition were considered but not implemented. The maximum input energy per pulse is presently limited to ~ 2 J.

Laser performance was improved by replacing most of the He buffer gas with Ne. A small amount of He was necessary since the HCl supply was buffered

127
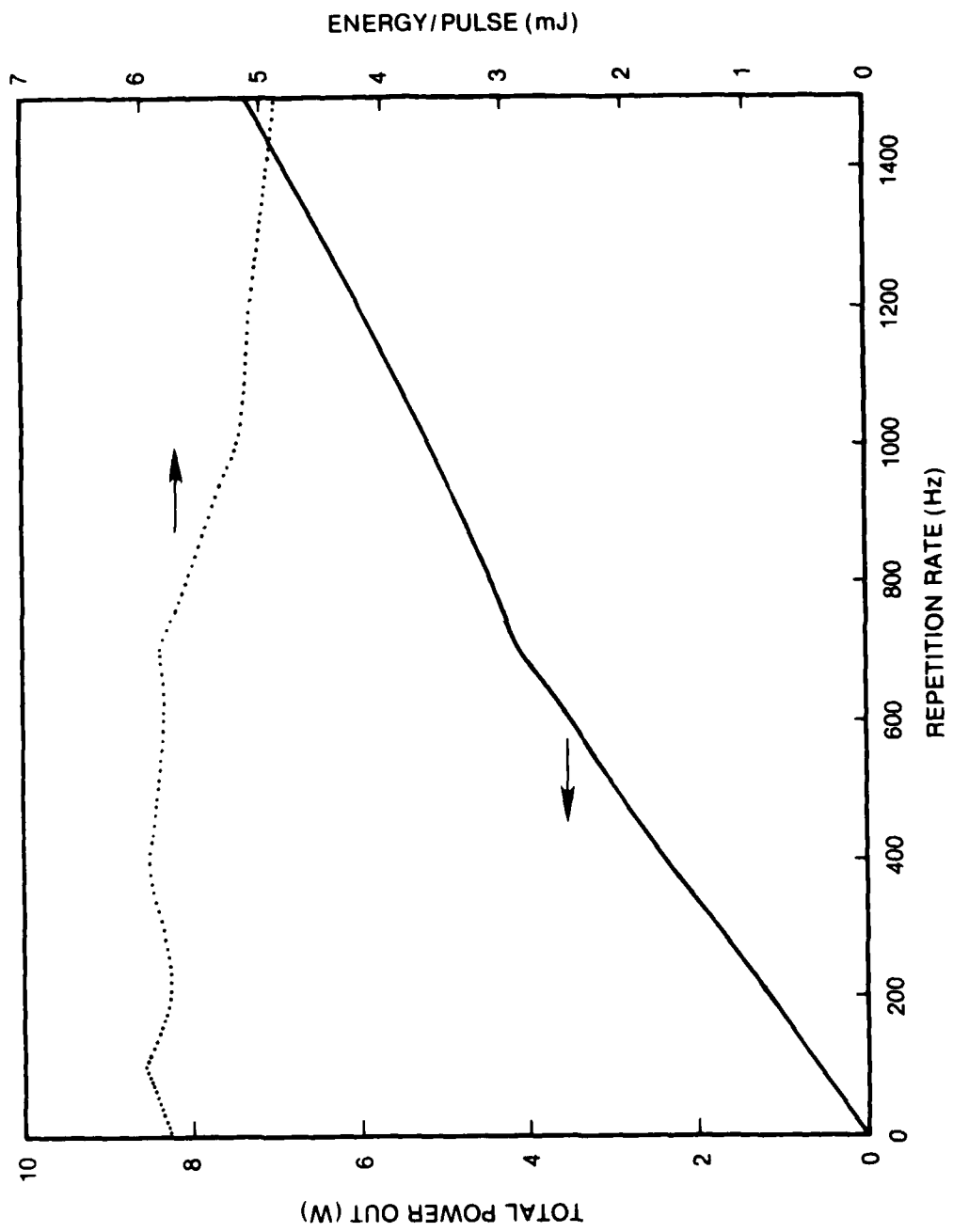
Figure 59. Total Power Out and Energy per Pulse as Function of Repetition Rate for 2-J/Pulse Switched Energy (20 kV).

128
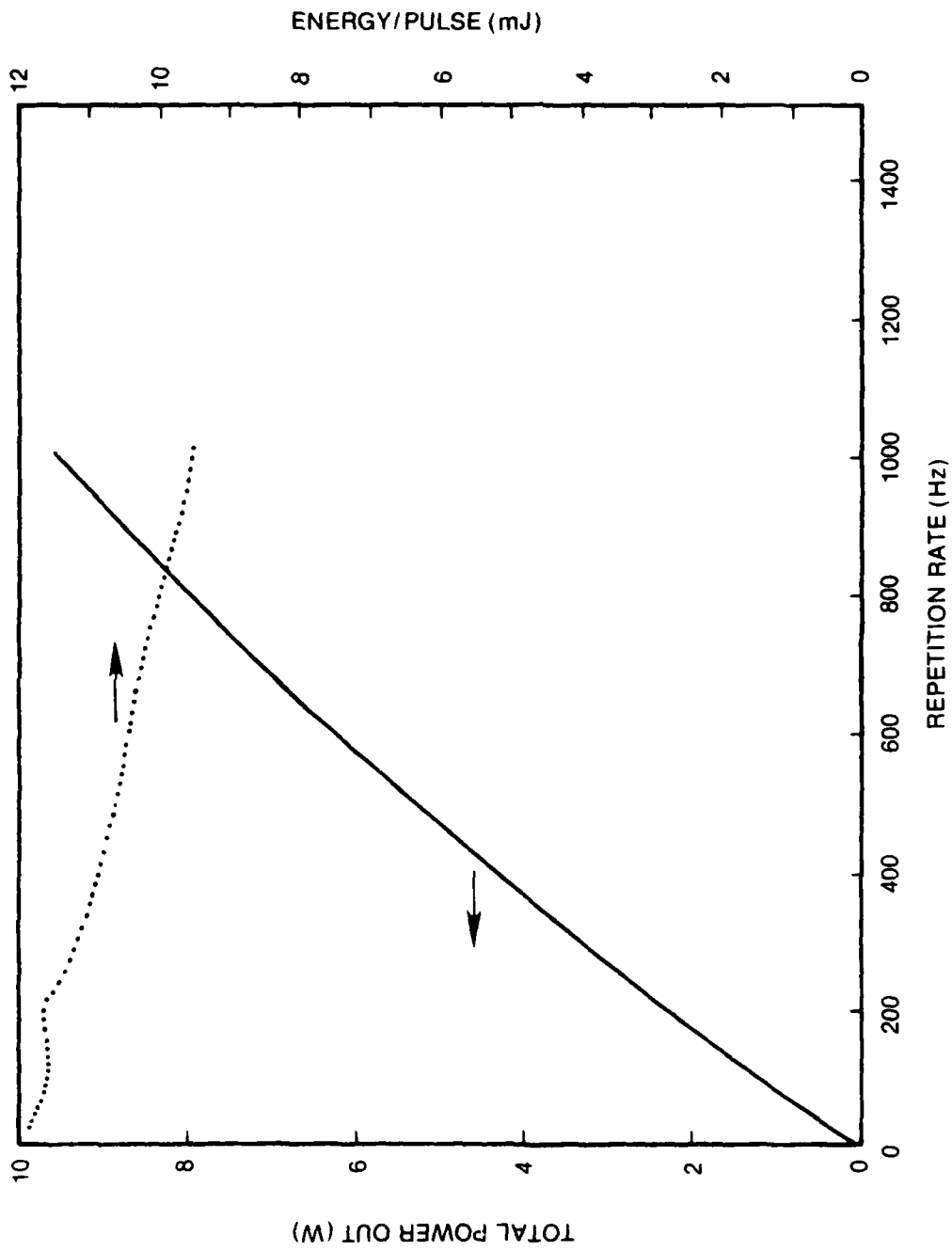
Figure 60. Total Power Out and Energy per Pulse as Function of Repetition Rate for 3.2-J/Pulse Switched Energy (25 kV).

129

Section IV

HIGH-REPETITION-RATE, HIGH-AVERAGE-POWER DYE LASER

The use of the 308-nm XeCl laser output for dye laser pumping has been demonstrated to be relatively efficient.[52,53] Short (12-psec) pulses[54] as well as high energy (1-J) output[55] have been obtained. The systems reported in the literature utilized dye cells in which the pumping and extraction of dye-laser energy was accomplished through the cell walls. The liquid/cell boundary layer, however, presents an impediment to high-rep-rate operation. Therefore, the feasibility of using an unconfined flowing jet stream was investigated.

Figure 61 shows the optical setup. The unpolarized XeCl laser beam was focused onto the dye jet at near-normal incidence, while the dye laser cavity was set at the Brewster angle corresponding to the dye solvent. The dye-cavity length was made as short as possible without the mirror mounts interfering with the pump beam. A trade-off was present here--the larger the deviation of the pump and dye beam, the less the overlap of useful area. However, since the pump beam was essentially unpolarized, maximum coupling of the 308-nm radiation was achieved at near-normal incidence. The dye beam was linearly polarized by the Brewster-angle placement of the jet in the cavity.

The jet-stream dye laser has a major advantage over dye lasers which utilize cells to guide the flowing dye solution, i.e., the absence of cell windows with their contamination and boundary-layer problems. There are, however, difficulties associated with achieving a stable, uniform jet stream having surfaces of good optical quality. A stable jet requires laminar flow, which occurs for Reynold's numbers (Re) less than 1000, where Re is given by[56]

$$Re = \frac{2\ell\bar{v}\rho}{\eta}$$

and ℓ is the nozzle (jet) thickness, $\bar{v}$ the average flow velocity, ρ the fluid density, and η the fluid viscosity. The constraint on Re limits the choice of dye solvent to high viscosity fluids. For example, for a typical

130
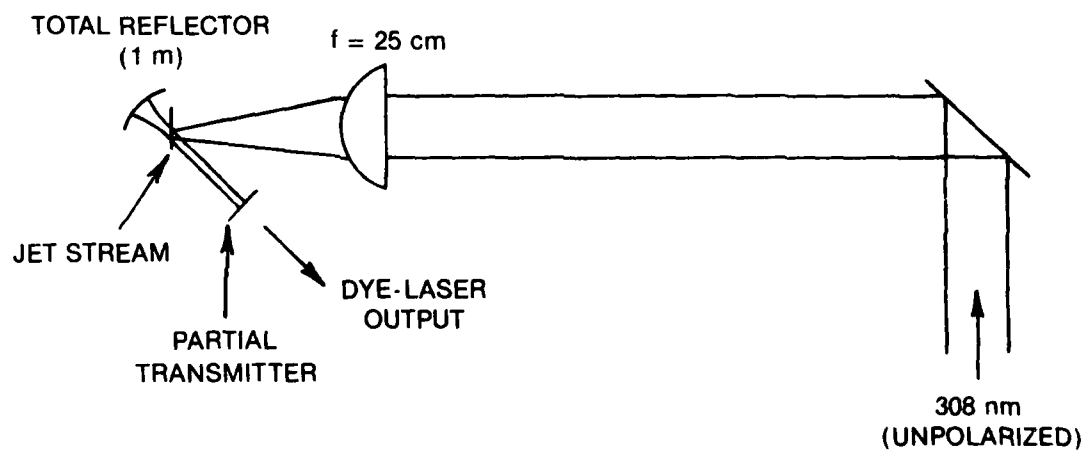
Figure 61. Schematic Diagram of High-Rep-Rate, XeCl-Pumped Flowing-Jet Dye Laser.

flow velocity of 10 m/s, a jet thickness of 0.4 mm, and fluid density of 1 gm/cm^3, the fluid viscosity must be greater than 8 cp to achieve laminar flow. At room temperature, there are few fluids with the required viscosity, ethylene glycol being the most appropriate.

Solvents which have been used in XeCl-laser-pumped dye lasers (cell confined) include ethanol, dioxane, and cyclohexane.[52] Ethanol and cyclohexane have viscosities of 1.2 and 1.02 cp, respectively, which are incompatible with jet stream requirements. Viscosity-raising additives can be used to increase the viscosities to the appropriate level; however these additives begin to absorb strongly below about 400 nm.[57] Ethylene glycol was felt to be the best initial choice as a solvent for the jet-stream dye laser.

The choice of a dye depends upon energy-conversion efficiency, wavelength, lifetime, and cost. Concerning the selection of visible-wavelength-emitting dyes for possible flow-visualization applications, coumarin 120, coumarin 102, rhodamine 6G (Rh 6G), and rhodamine B (Rh B) have exhibited high conversion efficiencies[52] (41.1, 39.8, 27.7, and 27.2%, respectively) when pumped by a XeCl laser. The lifetime of Rh 6G has been shown to be poor and that of Rh B good under 308-nm pumping.[58] Lifetime data on the coumarins were not available. Since Rh B at $24/gm is much cheaper than the coumarins ($56-69/gm), it was the dye of choice.

Lasing was achieved for a 50% output coupler with the total cavity length of ≤ 10 cm. Efficiency increased as the dye-cavity length was decreased. The minimum length was ∿ 1 cm total-reflector-to-dye and ∿ 2 cm dye-to-output-coupler. For a pump energy of 2.17 mJ/pulse, a dye laser energy of 135 μJ/pulse was obtained under operation at 100 Hz. This corresponds to a conversion efficiency of ∿ 6%. No attempt at tunable or narrow-band operation was made.

Efficiencies of ∿ 25% have been reported for a cell-confined dye laser of Rh B pumped by XeCl laser radiation.[52] The poor results obtained in the flowing-jet arrangement can be attributed to two factors: (1) small ratio of gain length to total cavity length and (2) lack of a sufficiently large optically flat area on the jet stream. The optical cavity can be shortened

132

by modifying the mirror mounts and using a smaller-diameter mirror adjacent to the pump beam. The use of a 0.5-in.-diam output coupler in the setup of Fig. 61, along with some minor modifications in the physical mounting arrangement of the cavity components, would allow for a total cavity length of $\sim$ 1 cm. Also, a 1-m output coupler--rather than the flat--would be more appropriate since the jet would be in the approximate center.

Improvement of the quality of the jet, however, is difficult. Several commercial as well as some in-house-manufactured nozzles were tested. The best results were obtained with two certified nozzles furnished by Spectra-Physics, manufactured for use in a commercial CW dye laser, although good results were obtained using an unrefined in-house procedure. Maximum uniform spot size appeared to be limited to $\sim$ 2 mm^2.

Lack of time prohibited further study of the high-rep-rate, XeCl-pumped dye laser. It appears that the major limiting factor is the jet quality. As the pump power increases, thermal lensing will become a problem unless the active dye area can be increased.

Section V

MAGNETIC SWITCHING

The term "magnetic switching," when applied to gas-discharge PFN's, refers to the use of magnetic-material saturation properties to effect a fast change in electrical impedance.[59] The main advantages of this switching technique over the commonly used hydrogen thyratrons are: (1) lower-switching power dissipation and (2) seemingly higher reliability and longer life. The majority of the power consumption of a switch occurs during the fall of the voltage across the switch as the current rises.[60] The voltage drop (and resulting current rise) of a thyratron is exponential in time, while a saturating inductor exhibits a nearly linear characteristic. This results in a lower value of peak power and a shorter transition period (assuming careful design) for a magnetic switch. The longer lifetime and improved reliability of saturating magnetics is inherent in the solid-state characteristic, whereas the thyratron relies on the transport of high-temperature, charged particles which effect electrode erosion and other damaging processes.

The main disadvantages of the magnetic switch are: (1) inability to remain in the open (blocking) state for any appreciable length of time, and (2) switching speed limitation in the 10 - 100 nsec. regime. The "switch" presents an impedance to a changing current only. Although the relative permeability of some ferromagnetic materials may reach $\sim$ 100,000 (e.g., Supermaloy), the effective change in permeability for a practical low-inductance switch is generally $\sim$ 100 - 500. This means that a device with a saturated inductance of 10 nH will have an "open" state (unsaturated core) inductance of 1 - 5 μH. Therefore, the circuit components from which the electrical energy is being held off (the load) must present a relatively low AC impedance. This could be a large capacitance or a small inductance. Obviously, an unshunted discharge gap cannot be the load since its AC impedance (pre-breakdown state) is very large. Consequently, the applications of magnetic switching techniques to gas discharges are generally limited to pulse compression or pulse sharpening.

134

The switching speed of a magnetic switch is limited to the speed at which core saturation occurs.[60] The rapid change of permeability of a magnetic material causes a rapid change of magnetic field within the material. This induces eddy currents which, for the 10 - 100 nsec switching regime, are confined to the skin of the material in a direction which opposes the changing magnetic field. Therefore, for rapid switching, the material must be no thicker than approximately one skin depth. For the 10 - 100 nsec regime, this requirement is difficult to fulfill. The recent advances of metallic glasses[61] (e.g., Metaglass) offer promises of thin (< 0.001 in.) resistive magnetic materials. However, the high-permeability Ni:Fe-based materials are still the most economical for thicknesses as low as 0.0005 in.

The practicality of using a magnetic switch in a rare-gas-halide laser system, then, is seemingly dependent upon the applicability of magnetic-pulse compression. In general, compression can be applied to the entire pulse, as in a multi-stage resonant-transfer circuit, or to an edge of the pulse only, as in a peaking arrangement. For the XeCl laser system of current interest, the resonant-transfer PFN is applicable for only short pulses. This is due to the relatively constant E/N during the discharge glow phase and is determined by the gas discharge kinetics. As the desired pulse length is increased, the electrical pumping efficiency decreases. As described in Section II, the maximum efficiency of a capacitor-driven PFN for pulse lengths greater than $\sim$ 50 nsec is less than 60%. Therefore, a resonant compression scheme is not applicable to a high-efficiency, long-pulse XeCl laser system.

The pulse-sharpening ability of a saturating-magnetic device seems more appropriate for a long pulse system. If the slowly rising edge of a thyratron-switched transmission line can be delayed until a sufficient voltage appears at the line output, a rapid breakdown followed by a rela-tively constant, long-time-duration pulse may be achievable. If the line-charge source is another transmission line, however, inefficiencies exist due to the energy reflected during the high-impedance state of the switch. In theory, a saturating-magnetic "switch" could be used to delay the appli-cation of voltage to a gap as a transmission line is resonantly charged by a thyratron-switched capacitor. Placing this concept into practice, however,

135

presents difficulties in circuit timing and in selection of a proper gap-shunting component as well as in design of the magnetic switch if high-rep-rate operation is required.

One of the major drawbacks of switching with saturating-magnetic components is the dependence of magnetic properties on rep rate. As rep rate is increased, the magnetic core will generally heat up, resulting in changes in the magnetic properties. An even more difficult problem is caused by the requirement of resetting the core to the same starting point before each pulse. Not only is it generally difficult to reset the core in a short time but also large amounts of energy may be required for an active reset when rep rates approach 1 kHz. A passive reset (using reflected PFN energy) may be more efficient but restricts the available range of frequencies, since conditions--especially reset time--will vary as rep rate is changed.

None of the applications discussed thus far are applicable to high-efficiency, high-rep-rate operation of the XeCl laser. The pulse-compression and pulse-sharpening schemes must provide a high overvoltage to the discharge gap in order to effect proper breakdown. The discussion of pulse-forming networks in Section II showed that power matching of PFN to the discharge required a voltage matching of PFN charge to gap glow voltage. An auxiliary circuit providing an overvolted prepulse (poker pulse) was discussed as a method of resolving this dilemma.

Since saturating magnetics exhibits some of the characteristics of a diode, one possible application is as a blocking component for isolation of a poker pulse from a low-impedance line, as shown in Fig. 62. Operation is as follows. The main energy-storage line is pulse charged to $\sim 2\ V_G$. It is imperative that the gas mixture be adjusted such that self-breakdown does not occur during this time. The saturable inductor is held at, or near, saturation--by a bias winding (not shown)--for current in the same direction as the eventual flow from line to gap. If the switch (R_p) of Fig. 62 is a thyratron, the line will be charged to a negative potential and the L_S core will be held near saturation for positive current flow through L_S from the gap in the line. As the thyratron is switched on, an overvoltage negative potential, determined by the charge on C_p, is placed on the gap. This poker

136
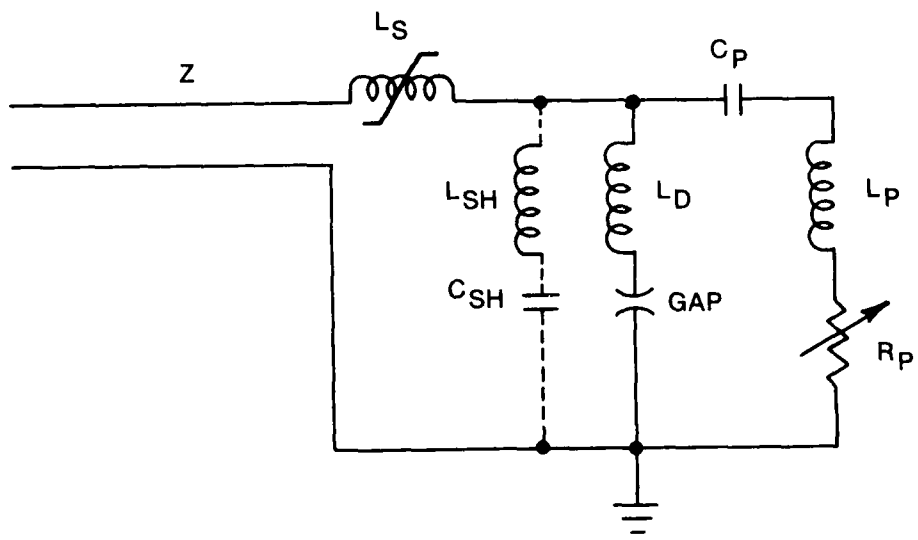
Figure 62.   Schematic Diagram of Poker-Assisted Transmission-
Line PFN Utilizing a Saturable-Core Blocking-Inductor.

pulse forces the core of L_S away from saturation in such a way that the inductor presents a high impedance to current flow through the low-impedance line. Upon gap breakdown, current flow again reverses; and, as saturation of L_S is achieved, the line energy is transferred to the gap.

The major advantage of this scheme is that the fast switch (thyratron) need only switch a small portion of the total PFN energy. Capacitor C_p may be small; its only purpose is to supply the initial overvoltage and the breakdown energy. Also, the reset point of the magnetic "diode" core is not critical. The closer the core is to the saturation point at initiation of the poker pulse, the shorter the time delay between gap breakdown and magnetic saturation, leading to conduction of the matched-line energy to the gap.

This time delay is the amount of time required for the core to recover from the unsaturated state to a saturated, low-impedance state. In simple terms, the volt-seconds in each direction must be equal. For example, if a poker pulse of V_p is present for a time of t_1, then a flux change of $(V_p - V_0)t_1$ has occurred in the core (V_0 is the charge voltage on the PFN main line). A flux change of $(V_0 - V_p)t_1$ must then occur before saturation is achieved. Since the line is ideally charged to 2 V_G and the poker pulse may be 4 V_G, the saturating time delay may be twice the time period of the overvoltage pulse. That is, $V_p - V_0 = 2 V_G$ and $\sim V_G$ is seen across the switch when the gap breaks down.

The largest disadvantage of this technique is the delay time just discussed. For example, if an overvoltage exists for 30 nsec before breakdown occurs, a delay of $\sim$ 60 nsec will be seen. The present model does not include stability criteria, and the required hardware was not available for testing on the present apparatus. Therefore, no conclusion has been reached on the detrimental effects of this delay.

Another configuration capable of combining saturable magnetic switching with a poker pulse was shown in Fig. 36; the theory of operation of this circuit was discussed in Section II. The poker pulse is magnetically coupled via the saturable-core transformer. An advantage of this technique is that the

voltage level switched in the poker circuit need be only $\sim$ 50% of that required by the parallel poker circuit of Fig. 62. This is due to the fact that the voltage developed across the transformer secondary (main current-carrying circuit) adds to the charge on the transmission line. Therefore, only 2 V_G need be switched (assuming good transformer coupling) in order to attain an overvoltage of 4 V_G, assuming that the line is already charged to 2 V_G. In the case of a pulse traveling down the line, the poker pulse could be timed to arrive coincident with the leading edge, effectively enhancing both the voltage risetime and the overvoltage level.

The major advantages of this circuit, however, are the decreased "dead" time required for core saturation and the decreased switching time. In the previous case, the poker circuit was in parallel with the discharge and, therefore, had little effect on the core after gap breakdown. In the transformer coupled circuit, however, forward discharge current will be maintained as the potential on the poker capacitor reverses. As this current decreases, the flux change in the core reverses direction, heading toward the desired saturation condition. When current in the poker circuit reaches zero, the potential seen on the primary of the transformer will cause a flux change in the desired direction; that is, both the transmission line and the poker circuit will contribute to flux buildup. In other words, after capacitor reversal, the effective voltage on the transformer is 2 V_G due to the charged transmission line and 2 V_G due to the charged capacitor (assuming full reversal). In the parallel poker scheme, twice the overvoltage period was needed to return the core to saturation; the transformer case requires only one-half the overvoltage period if the poker reverses quickly.

Figure 63 shows results of a representative transformer-coupled poker-circuit model. Simulation of the saturating core consisted of a simplified table of variable permeability values, where the reference value was $\int V \, dt$. No hysteresis was used in this model. A maximum transformer coupling of 50% was used in this case, considering the difficulty of constructing an efficient stripline transformer.

139
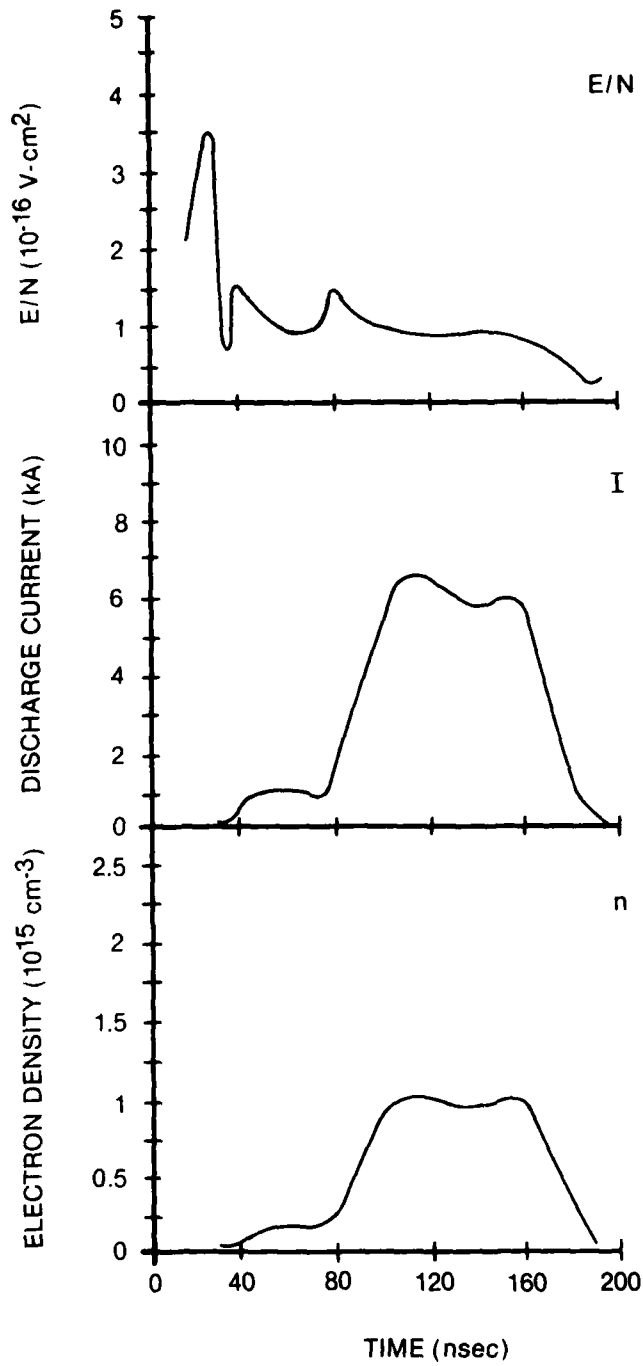
Figure 63.   Calculated Discharge Waveforms of Constant-
Impedance PFN with Transformer-Coupled Poker
Pulse.

Several points can be made concerning Fig. 63. First, a short, fast glitch is evident in the E/N plot near the beginning of breakdown, denoting the beginning of core saturation. This spike is seen to have little detrimental effect on the circuit. If saturation had occurred much earlier, however, excessive ringing would hamper circuit operation. Careful design of the transformer core should eliminate this. Secondly, the poker circuit will ring after core saturation occurs. This has little effect on the discharge gap since the voltage levels are not sufficiently large to bring the core out of saturation; consequently, the transformer coupling is very small. This ringing may prove damaging to the thyratron, however. A small damping resistance should decrease this ringing without appreciably altering overall circuit operation. Since reverse conduction of the thyratron cannot be avoided, it is essential that the reverse current be small compared to the thyratron ratings.

Note that the direction of current after breakdown is positive and relatively constant. The time required for core saturation, however, appears long compared to the overvoltage time. This period is almost entirely due to the reverse charging on the poker capacitor and can be minimized by using a small value of capacitance for C_p as well as providing good coupling within the transformer.

A final point which should be made regarding Fig. 63 is that the efficiency of transfer of energy from the main energy-storage transmission line to the discharge gap was $\sim$ 93% for this modeled case. The poker energy represented only $\sim$ 3% of the line energy for an overall efficiency of $\sim$ 90%. Core losses were not calculated. However, due to time and equipment constraints, this effort was terminated before optimization could be performed. No experimental verification could be accomplished except for a rough setup with an air gap and a tape-wound iron-alloy C-core. Preliminary results were promising. The concept is, therefore, worthy of a more thorough study.

141

Section VI

HIGH-EFFICIENCY, COMPACT POWER SUPPLY

Interfacing of a power-conditioning system to a high-efficiency, compact power supply was investigated. An existing supply, built by Power Electronics Associates,[62] is a double-sided resonant inverter which delivers current pulses at a 10-KHz rate. The charge in each pulse is delivered as a half-sine wave output of the inverter and is constant from pulse to pulse. The voltage level is regulated by a feedback network which monitors the voltage on the output filter capacitor and regulates the number of current pulses. This operating method results in a power-supply capability of $\sim$ 250 mA average at the operating voltage selected. That is, it will deliver a power rating of 5 kW at 20 kV and 2.5 kW at 10 kV.

The "current-pulse" method appears ideal for supplying charge to a laser pulse- forming network, but the construction of the Electronics Associates supply presented some problems. First of all, the charge delivered in each pulse is $\sim 2.5 \times 10^{-5}$ Coul., but the charge required to reach 15 kV on a 5-nF capacitor is 7.5×10^{-5} Coul. The repetition rate, then, is limited to one-third of the operating frequency, or $\sim$ 3.3 kHz, unless a smaller energy-storage capacitor is used. Secondly, there was no provision for synchronizing the power-supply pulses to an external source. Assuming that the feedback network could be connected to the laser energy-storage capacitor, there would still be a charge uncertainty of one output pulse. For the 5-nF capacitor, this would result in a charge voltage of $15 \, ^{+3}_{-0}$ kV. The output ripple is, therefore, unacceptable.

The output ripple can be reduced to an insignificant value by use of a large output-filter capacitor, but some switching means must then be added. Presently, a bulky and inefficient tetrode constant-current system is employed. For high efficiency, a resonant charging method would be much more suitable. The switch could be eliminated by use of a saturable-core inductor as the charging choke, but rep-rate adjustability would then be lost.

The limitation on repetition rate is fundamental to the operation of the Electronics Associates high-efficiency power supply. The application for a compact power-supply/power-conditioning system is the closed-cycle annular-flow- return laser[30] operating at high rep rate (1 - 10 kHz). Therefore, it was necessary to build a new power-supply system.

Various alternative methods were evaluated: 1) thyratron-switched resonant charging, 2) saturable-core-choke resonant charging, and 3) transformer-coupled resonant charging.

Conventional resonant charging has two drawbacks: 1) charging begins immediately after the laser discharge and 2) the charging time is fixed. The first problem imposes a limitation on the rep rate since the main thyratron must be given time to deionize; the second problem limits the laser operating rep-rate range, depending upon the speed with which the energy-storage capacitor bleeds off its charge. The use of a saturable inductor creates a delay in the charging cycle, allowing for high-rep-rate operation; but the rep-rate range is still limited, and an inaccuracy is introduced into the charge cycle. That is, the uncertainty of resetting the permeability of the core material to the same value on each charge cycle causes an uncertainty of the level of capacitor charge, resulting in laser-amplitude fluctuations. This is evident in one published report[63] on the operation of a saturable-core choke-charging circuit.

The use of a thyratron switch in a resonant charging circuit adds the capability of controlling the turn-on time of the charging current but also introduces additional complications in the circuit. The thyratron, being a gas switch, must be given time to deionize before voltage is reapplied to it. Therefore, assuming that the main thyratron has a deionization time of 40 μsec and the charging thyratron deionizes in 20 μsec only 40 μsec remains for charging during operation at 10 KHz. A more severe complication is introduced by the fact that the charging-thyratron cathode is at the same potential as the energy-storage capacitor, which is switched by the main thyratron. This results in potentially damaging corona in the isolation transformer which furnishes cathode- and reservoir-heater power to the charging thyratron.

143

The above problems, for the most part, can be alleviated by switching at low voltage with a solid-state SCR in a step-up transformer-coupled resonant circuit. Figure 64 shows such a circuit. During the positive half-cycle, the current (I_1) in the low-voltage winding is

$$I_1 \Big|_{0 \leq t < t_c} = \frac{V}{L_p} t + \frac{K^2 V}{\omega_1 L_p (1-K^2)} \sin \omega_1 t \qquad (60)$$

where t_c is the time at which the SCR is commutated off, V is the power-supply voltage, L_p is the self-inductance of the transformer primary winding, K is the transformer coupling coefficient, and

$$\omega_1 = \frac{1}{a^2 C L_p (1-K^2)} \qquad (61)$$

with a being the transformer turns ratio and C the value of the storage capacitor. In this circuit the transformer leakage inductance, equal to $L_p(1-K^2)$, is utilized as the charging choke. The current (I_2) in the secondary winding is

$$I_2 \Big|_{0 \leq t < t_c} = - \frac{KV}{\omega_1 a L_p (1-K^2)} \sin \omega_1 t \qquad (62)$$

For simplicity, the charging resistor has been omitted. In reality, Eqs. (60) and (62) would include a damping term and Eq. (61) would be modified with an $R^2/4L$ term; but these are insignificant for typical times and component values of interest.

The voltage (V_c) on the energy-storage capacitor (assuming V_c = 0 at t = 0) is

$$V_c \Big|_{0 \leq t < t_c} = VKa(\cos \omega_1 t - 1) \qquad (63)$$

A peak voltage of 2 VKa will be obtained when $\omega_1 t = \pi$. At this time Eq. (60) gives the current in the primary circuit as ($V/L_p t$). In order to stop

144
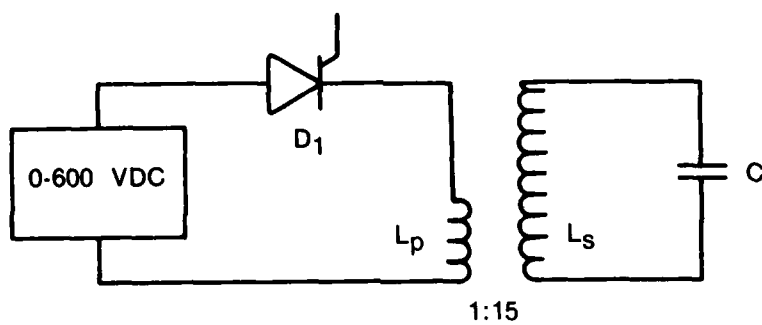
Figure 64.   Simplified Schematic of Transformer-Coupled
Resonant Charging Circuit.

the primary-current flow, the circuit must ring back sufficiently to commutate the SCR. Once this occurs, the capacitor decay will be dependent upon the secondary circuit only. That is,

$$I_2\bigg|_{t>t_c} = \frac{V_c'}{\omega_2 L_s}\ \sin \omega_2 t + I_0 \cos \omega_2 t \tag{64}$$

where

$$\omega_2 = \frac{1}{L_s C} \tag{65}$$

and the capacitor voltage is

$$V_c\bigg|_{t>t_c} = V_c \cos \omega_2 t - I_0\ \frac{L_s}{C} \sin \omega_2 t \tag{66}$$

Here V_c and I_0 are the capacitor voltage and secondary winding current existing immediately after commutation of the SCR. With a transformer secondary winding having 10-H self-inductance, V_c is within 93% of the peak charging voltage after the 15 μsec required for SCR turnoff. At this time, ∿ 2.5 mJ is stored in the transformer secondary. With the proper choice of an RC snubber circuit across the SCR, the voltage on the storage capacitor can be held constant for ∿ 10 μsec. after the SCR commutation, allowing for low pulse-to-pulse amplitude variation even if some frequency jitter exists in the operation of the SCR.

The circuit schematic for the high-efficiency, pulse-charging system installed on the annular-flow-return laser is shown in Fig. 65. The controllable source of DC power is two series-connected 0 - 300 V power supplies. These are SCR-type supplies with a 440 VAC-3φ input. The charge level of the 5-nF energy-storage capacitor is controlled through adjustment of the DC output level of these supplies. The step-up transformer was custom-made; a voltage multiplication of ∿ 25 is achieved.

Synchronization of the charging circuit with the laser discharge is accomplished by triggering the SCR $\sim$ 50 μsec before the thyratron. A sense circuit is included in the trigger circuitry in order to inhibit the SCR trigger whenever charge is present on the energy-storage capacitor. Without this safeguard, it is possible for the voltage on the transformer secondary to reach damaging levels.

This circuit provides a very simple, but rugged, method of effecting a resonant charge of a PFN. It differs from other transformer-coupled resonant charging schemes in that the use of a series diode in the high-voltage line is eliminated. Because of the fast risetime of a thyratron circuit and the fast ringing of a PFN, diodes normally are either subjected to severe stresses or protected by lossy high-voltage snubber circuits. In principle, the method of Fig. 65 requires only the simple low-voltage-snubbing RC leg shown.

The major problem encountered was saturation of the transformer core which occurred during blocking of the reverse current of the charged capacitor. The 1200-V-rated SCR required $\sim$ 10 μsec for complete turnoff which means that the full charge voltage of the energy-storage capacitor is seen on the transformer secondary with the primary essentially open-circuited. The resulting magnetization of the core (Supermalloy) will result in eventual core saturation unless a reset is effected between charge cycles. At low repetition rates, this is relatively easy to accomplish since a transformer DC bias current is present. At higher rep rates, however, the period between pulses is insufficient for adequate reset by the bias winding alone. However, the inefficiencies of the PFN/discharge arrangement cause a negative ring-back. This reverse potential is maintained on the transformer secondary--since the primary is an open circuit--for as long as possible. Firing of the shunting SCR/resistor branch in the primary just prior to the beginning of the next charge cycle results in sufficient reset for operation at $\sim$ 5 kHz.

The maximum repetition rate for the circuit installed on the annular-return laser is not known at this time, although the design goal was 5 KHz. An unfortunate interaction of the laser recirculating-fan control circuit with

147

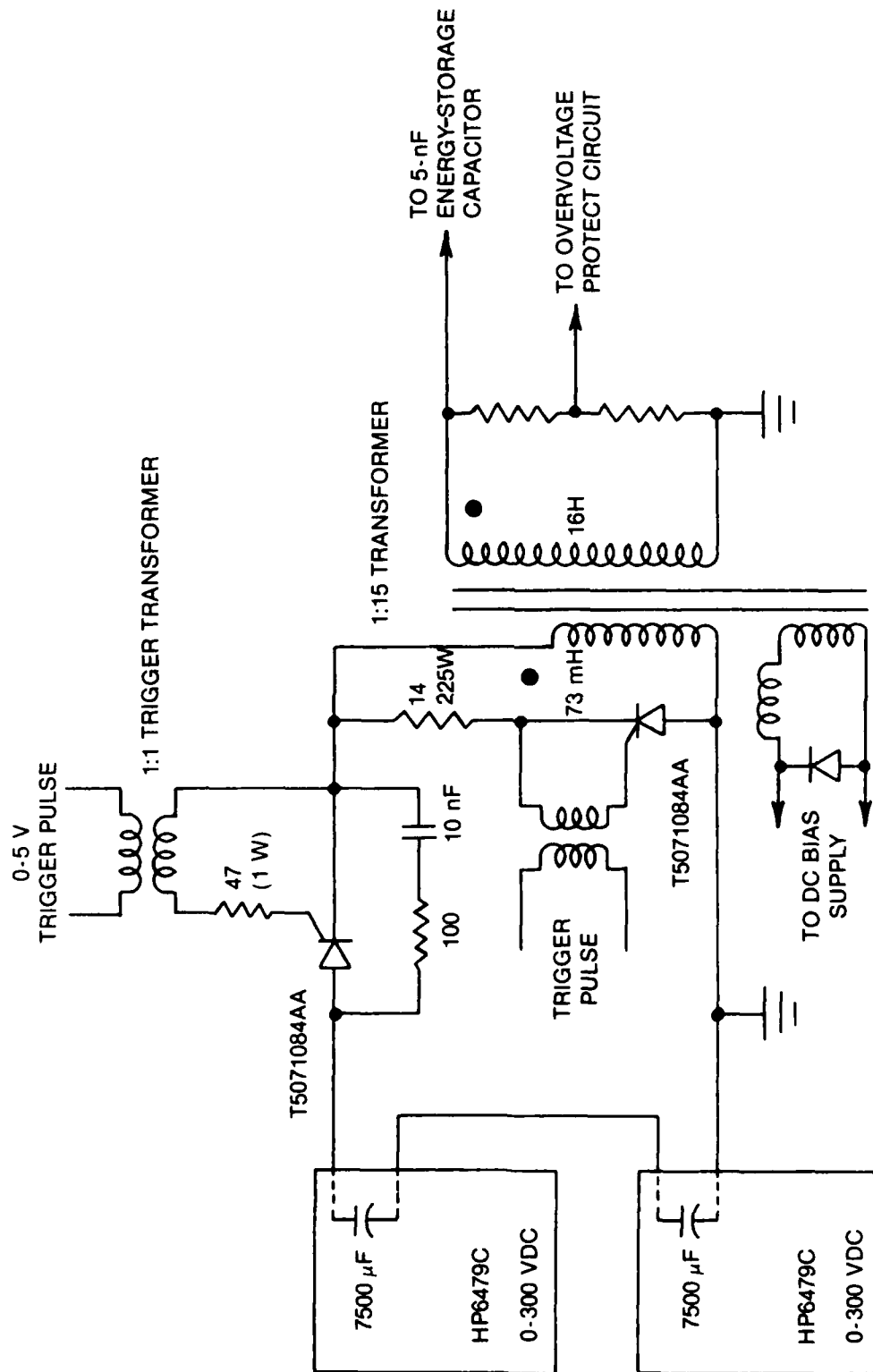Figure 65. Electrical Schematic of High-Efficiency, Pulse-Charging Circuit.

discharge RFI prevented operation above 4 kHz. If this interaction can be corrected, the maximum rep rate can be increased beyond 5 kHz by redesign of the transformer core and reset circuit. The ultimate limit will be governed by the charging time of the energy-storage capacitor plus the turn-off time of the main switching SCR.

Section VII

CONCLUSION

Computer modeling of a He/Xe/HCl gas mixture has shown that ionization and attachment are predominantly two-step processes. The overall ionization rate is a strong function of E/N, while the overall attachment rate is weakly dependent upon E/N. The interaction of the gas discharge with the external circuit, therefore, results in a relatively constant E/N appearing on the discharge during the glow phase. This characteristic allows for some simplification in modeling a discharge circuit by simulation of the gap as a constant voltage for much of the time period during which the discharge is in operation.

For high-rep-rate operation, the switching element must be a thyratron or similar gas-discharge device. The inherent stray inductance resulting from this requirement posed the most severe challenge in the design of a power-conditioning network. Various circuit configurations were studied. Optimum performance for a lumped-element network was achieved with a peaking-capacitor arrangement, although long pulses were not practical and high efficiency could not be attained. A constant-impedance PFN was shown to be required for long-pulse, high-efficiency operation, but auxiliary ionization was required for optimal operation; line matching to the discharge can be achieved only with an initial line charge voltage which is twice the discharge glow voltage. A transformer-coupled "poker" pulse arrangement was proposed as the source of an overvoltage prepulse.

A high-rep-rate ($\sim$ 1.5 kHz), closed-cycle XeCl laser was constructed. Initially, UV preionization was used, but a rapid buildup of contaminants was observed. This was attributed to the UV- or discharge-initiated break-down of the insulating material in the vicinity of the UV source. An x-ray preionizer was then installed; no contaminants or deterioration of gas was observed in this configuration. Repetition rates of 1.5 kHz were obtained.

The XeCl laser was used for optical pumping of a flowing-jet dye stream. Multi-wavelength lasing was achieved at high rep rates. With improvements

150

in the optical quality of the jet nozzle, high average power should be attainable with a tunable dye laser.

The application of magnetic-switching techniques to high-rep-rate XeCl laser operation was considered. Although the standard pulse-compression schemes are useful for short-pulse systems, these arrangements are not advantageous for long pulse duration.

A 5-kHz high-efficiency transformer-coupled power source was constructed for use with high-rep-rate gas-discharge lasers. This source was unique in that no high-voltage blocking element was required.

REFERENCES

1. See *Excimer Lasers*, C. K. Rhodes, ed. (Springer-Verlag, Berlin, 1979).

2. Unpublished cross sections of W. F. Bailey. Range of 0.008-6 eV based upon values of R. W. Crompton, M. T. Elford, and A. G. Robertson, Australian J. Phys., 23, 667 (1970), as compiled by L. J. Kieffer, Report JILA ICR 13 (National Bureau of Standards, Boulder, CO, 30 September 1973), NTIS No. COM-74-11661.

3. Due to rapid formation of 2^3S from the 2^1S state, the electron-collision cross sections of both states have been combined. Range of 19.5-23.54: G. J. Shulty and R. E. Fox, Phys. Rev. 106, 1179 (1957) and G. J. Shultz and J. W. Philbrick, Phys. Rev. Lett. 13, 477 (1964), as compiled by L. J. Kieffer, Report JILA ICR 13 (National Bureau of Standards, Boulder, CO, 30 September 1973), NTIS No. COM-74-11661. Range from 23.5 to 100 eV set constant at cross section corresponding to 23.54 eV. Values compiled by G. L. Duke (AFWAL/POOC-3, 1980, unpublished).

4. J. D. Jobe, R. M. St. John, Phys. Rev. 164, 117 (1967), as compiled by L. J. Kieffer, Report JILA ICR 13 (National Bureau of Standards, Boulder, CO, 30 September 1973), NTIS No. COM-74-11661.

5. J. W. McConkey, F. G. Donaldson, and M. A. Hender, Phys. Rev. Lett. 26, 1413 (1971), as compiled by L. J. Kieffer, Report JILA ICR 13 (National Bureau of Standards, Boulder, CO, 30 September 1973), NTIS No. COM-74-11661.

6. D. Rapp and P. Englander-Golden, J. Chem. Phys. 43, 1464 (1965), as compiled by L. J. Kieffer, Report JILA ICR 13 (National Bureau of Standards, Boulder, CO, 30 September 1973), NTIS No. COM-74-11661.

7. Unpublished cross sections of G. L. Duke (AFWAL/POOC-3, 1980); Range of 0-20 eV based upon values of L. S. Frost and A. V. Phelps, Phys. Rev. 136, A1538 (1964), as compiled by L. J. Kieffer, Report JILA ICR 13 (National Bureau of Standards, Boulder, CO, 30 September 1973), NTIS No. COM-74-11661.

8. M. R. Flannery, *Calculation of Electron Impact Cross Sections From Metastable States*, Technical Report AFAPL-TR-78-58 (Air Force Aero Propulsion Laboratory, Wright-Patterson AFB, OH, August 1978), as compiled by G. L. Duke (AFWAL/POOC-3, 1980, unpublished).

9. Unpublished cross sections of G. L. Duke (AFWAL/POOC-3, 1980). Sum of individual cross sections based upon measured values of M. Schaper and H. Scheibner, Beit. Plasma Phys. 9, 45 (1969).

10. J. A. Shirley, R. J. Hall, and B. R. Bronfin, *E-Beam HCl Laser*, Final Report on ONR Contract No. N00014-72-C-0450 (United Aircraft Corporation, East Hartford, CN, 3 August 1974), AD No. 784,500, as compiled by G. L. Duke (AFWAL/POOC-3, 1980, unpublished).

11. K. Rohr and F. Linder, "Vibrational Excitation in e-HCl Collisions at Low Energies," J. Phys. B: Atom. Mol. Phys. $\underline{8}$, L200 (1975), and K. Rohr and F. Linder, "Vibrational Excitation of Polar Molecules by Electron Impact I. Threshold Resonances in HF and HCL," J. Phys. B: Atom. Mol. Phys. $\underline{9}$, 2521 (1976), as compiled by G. L. Duke (AFWAL/POOC-3, 1980, unpublished).

12. R. Azria, L. Roussier, R. Paineau, and M. Franc, "Attachment Electronique Dissociatif Sur HCl et DCl," Revue De Physique Appliquee $\underline{9}$, 469 (March 1974).

13. Cross sections estimated by multiplying the values of Ref. 12 by 40 and shifting on the energy axis by the threshold energy (0.358 eV).

14. Cross sections estimated by multiplying the values of Ref. 12 by 800 and shifting on the energy axis by the threshold energy (0.702 eV).

15. Original Boltzmann Transport Code developed by W. Bailey. The version used here is described by J. Happ, III, P. Benedict, Jr., and W. P. Bailey in Boltz: A Code to Solve the Boltzmann Electron Transport Equation, TR-78-001 (Sandia Corp., Albuquerque, NM, 1978).

16. C. B. Moore and P. F. Zittel, "State Selected Kinetics from Laser Excited Fluorescence," Science $\underline{182}$, 541 (9 November 1973); also estimates of J. H. Kiefer, "Effect of VV Transfer on the Rate of Diatomic Dissociation," J. Chem. Phys. $\underline{57}$, 1938 (1 September 1972), from data of W. D. Breshears and P. F. Bird, "Densitometric Measurements of the Vibrational Relaxation of HCl and DCl in Shock Waves," J. Chem. Phys. $\underline{50}$, 333 (1 January 1969).

17. M. A. Biondi, "Recombination," in Principles of Laser Plasmas, G. Bekefi, ed. (John Wiley and Sons, NY, 1976).

18. Y. Shiu, M. A. Biondi, and D. P. Sipler, "Dissociative Recombination in Xenon: Variation of the Total Rate Coefficient and Excited-State Production with Electron Temperatures," Phys. Rev. A15, 494 (1977), as quoted by S. Lawton and T. A. De Temple in Near Infrared Gas Lasers, University of Illinois contract final report, AFAPL-TR-78-107 (Air Force Aero Propulsion Laboratory, Wright-Patterson Air Force Base, OH, December 1978).

19. Mixture weighted (95/5/0.2) in rate using data compiled by C. A. Brau, "Rare Gas Halogen Excimers," in Topics in Applied Physics, Vol. 30 (Excimer Lasers, Chapter 4, p. 104), C. K. Rhodes, ed. (Springer-Verlag, NY, 1979).

20. Optimal electron density is inferred from data of discharge current measured by other authors. See, for example, (a) R. S. Taylor, P. B. Corkum, S. Watanabe, K. E. Leopold, and A. J. Alcock, "Time-Dependent Gain and Absorption in a 5 J UV Preionized XeCl Laser," IEEE J. Quant. Electron. QE-19, 416 (1983) and (b) R. C. Sze, "Improved Lasing Performance of XeCl Using Ar and Ne Diluents," J. Appl. Phys. $\underline{50}$, 4596 (1979).

21. J. C. Bowers and S. R. Sedore, <u>SCEPTRE: A Computer Program for Circuit and Systems Analysis</u>, F. F. Kuo, ed. (Prentice Hall, Englewood Cliffs, NJ, 1971).

22. A. Garscadden, private communication.

23. W. H. Long, Jr., "Pulse Forming Networks for High Pressure Discharges," Paper EB-5, 33rd Annual Gaseous Electronics Conference, Norman, OK, 1980.

24. J. I. Lavatter and S. C. Lin, "Necessary Conditions for the Homogeneous Formation of Pulsed Avalanche Discharges at High Gas Pressures," J. Appl. Phys. $\underline{51}$, 210 (1980).

25. A. E. Hill, "Continuous Uniform Excitation of Medium-Pressure CO_2 Laser Plasmas by Means of Controlled Avalanche Ionization," Appl. Phys. Lett. $\underline{22}$, 670 (1973).

26. W. H. Long, M. J. Plummer, and E. A. Steppaerts, "Efficient Discharge Pumping of an XeCl Laser Using a High-Voltage Prepulse," Appl. Phys. Lett. $\underline{43}$, 735 (1983).

27. I. D. Smith, "A Novel Voltage Multiplication Scheme Using Transmission Lines," in <u>IEEE Conference Record of Fifteenth Power Modulator Symposium</u>, 1982, p. 223.

28. G. N. Glasoe and J. V. Labacqz, <u>Pulse Generators</u> (McGraw Hill, NY, 1948).

29. R. A. Olson and D. F. Grosjean, <u>Advanced Concepts in Closed-Cycle Lasers</u>, Technical Report AFWAL-TR-80-2026 (Air Force Wright Aeronautical Laboratories, Wright-Patterson Air Force Base, OH, 1980).

30. R. A. Olson, D. F. Grosjean, B. Sarka, A. Garscadden, and P. Bletzinger, "High-Repetition-Rate Closed-Cycle Rare Gas Electrical Discharge Laser," Rev. Sci. Instrum. $\underline{47}$, 677 (1976).

31. Ferrofluidic is a registered trademark of Ferrofluidics, Inc., 40 Simon St., Nashua, NH 03061.

32. Kynar is a vinylidene flouride registered trademark of Pennwalt Corp., Philadelphia, PA.

33. Z. Burlamacchi, P. Burlamacchi, and R. Salimbeni, "Long-Life Operation of an XeCl Excimer Laser," Appl. Phys. Lett. $\underline{34}$, 33 (1979).

34. J. L. Miller, J. Dickie, J. Davin, J. Swingle, and T. Kan, "Operating Characteristics of a Closed Cycle Flow Rare Gas Halide Laser," Appl. Phys. Lett. $\underline{35}$, 912 (1979).

35. M. C. Gower, A. J. Kearsby, and E. E. Webb, "Gas Composition and Lifetime Studies of Discharge Excited Rare Gas Halide Lasers," IEEE J. Quant. Electron. $\underline{QE-16}$, 231 (1980).

36. A. E. Axworthy, Rocketdyne Division Rockwell International Semiannual Report RI/RD80-235 under Contract DAAH01-80-C-0781 covering the period 2 June - 15 November 1980 (Rockwell International, Canoga Park, CA, November 1980).

37. R. Tennant, Technical Report LA-UR-81-559 (Los Alamos Scientific Laboratory, Los Alamos, NM, 1981).

38. Catalytic Deposition of Ni-P Alloys by Chemical Reduction in Aqueous Solution (Symposium on Electroless Nickel Plating), ASTM Special Technical Publication No. 265 (American Society for Testing and Materials, Philadelphia, PA, 1959).

39. D. F. Grosjean and B. Sarka, Operators Manual for High-Repetition-Rate, Closed-Cycle XeCl Laser Facility, delivered to AFWAL/POOC-3 under separate cover.

40. W. W. Rigrod, "Homogeneously Broadened CW Lasers with Uniform Distributed Loss," IEEE J. Quant. Electron. QE-14, 377 (May 1978).

41. L. F. Champagne, "Efficient Operation of the Electron-Beam-Pumped XeCl Laser," Appl. Phys. Lett. 33, 523 (15 September 1978).

42. R. S. Taylor, A. J. Alcock, and K. E. Leopold, "Electrical and Gain Characteristics of a Simple Compact XeCl Laser," Opt. Commun. 31, 197 (November 1979).

43. L. F. Champagne, L. J. Palumbo, and T. G. Finn, "Absorption Processes in the XeCl Laser," Appl. Phys. Lett. 34, 315 (1 March 1979).

44. W. L. Nighan and R. T. Brown, "Efficient XeCl (B) Formation in an Electron-Beam Assisted Xe/HCl Laser Discharge," Appl. Phys. Lett. 36, 498 (1 April 1980).

45. S. Watanable, A. J. Alcock, K. E. Leopold, and R. S. Taylor, "Spatially Resolved Gain Measurements in UV Preionized Homogeneous Discharge XeCl and KrF Lasers," Appl. Phys. Lett. 38, 3 (1 January 1981).

46. R. C. Sze and E. Seegmiller, "Operating Characteristics of a High Repetition Rate Miniature Rare-Gas-Halide Laser," IEEE J. Quant. Electron. QE-17, 81 (January 1981).

47. C. A. Brau, "Rare Gas Halogen Excimers," in Excimer Lasers, C. K. Rhodes, ed. (Springer-Verlag, Berlin, 1979).

48. T. G. Finn, R. S. F. Chang, L. J. Palumbo, and L. F. Champagne, "Kinetics of the XeCl (B X) Laser," Appl. Phys. Lett. 36, 789 (15 May 1980).

49. J. Tellinghuisen, J. M. Hoffman, G. C. Tisone, and A. K. Hays, "Spectroscopic Studies of Diatomic Noble Gas Halides: Analysis of Spontaneous and Stimulated Emission from XeCl," J. Chem. Phys. 64, 2484 (15 March 1976).

50. W. M. Clark and J. A. Palmer, Ion Plasma Electron Gun Research, Final Report, Contract No. N00014-77-C-0484 (Hughes Research Laboratories, Malibu, CA, 1977).

51. H. Gallagher, private communication.

52. O. Uchino, T. Mizunomi, M. Maeda, and Y. Miyazoe, "Efficient Dye Lasers Pumped by a XeCl Excimer Laser," Appl. Phys. 19, 35 (1979).

53. H. Telle, W. Hiiffer, and D. Basting, "The XeCl Excimer Laser: A Powerful and Efficient UV Pumping Source for Tunable Dye Lasers," Opt. Commun. 38, 402 (1981).

54. S. Szatmari and F. P. Schafer, "Excimer-Laser-Pumped ps-Dye Laser," Appl. Phys. B. 33, 95 (1984).

55. R. S. Taylor and P. B. Corkum, "A One Joule, XeCl Pumped Dye Laser," Appl. Phys. B. 26, 31 (1981).

56. H.-P. Hari, S. Leutwyler, and E. Schumacher, "Nozzle Design Yielding Interferometrically Flat Fluid Jets for Use in Single-Mode Dye Lasers," Rev. Sci. Instrum. 53, 1855 (1982).

57. S. Leutwyler, E. Schumacher, and L. Woste, "Extending the Solvent Palette for CW Jet Stream Dye Lasers," Opt. Commun. 19, 197 (1976).

58. P. B. Corkum and R. S. Taylor, "Picosecond Amplification and Kinetic Studies of XeCl," IEEE J. Quant. Electron. QE-18, 1962 (1982).

59. A number of excellent discussions and applications can be found in IEEE Conference Record of 1982 Fifteenth Power Modulator Symposium (June 14-16, 1982) (The Institute of Electrical and Electronics Engineers, Inc., NY, 1982).

60. W. C. Nunnally, Magnetic Switches and Circuits, Report LA-8862-MS (Los Alamos National Laboratory, Los Alamos, NM, 1981).

61. D. Nathasingh and C. H. SMith, "A High-Flux, Low-Loss Magnetic Material for High Frequency Applications," Proceedings of Powercon 7, San Diego, CA, March 25-27, 1980.

62. Developed by F. C. Schwarz (Power Electronics Associates, Inc., Lincoln, MA) under Contract No. F33615-77-C-2059 with the Air Force Aero Propulsion Laboratory, Wright-Patterson Air Force Base, OH.

63. Z. Karny, A. Rotstien, D. Chuchem, and I. S. Milanski, "70 KW High Repetition Rate Laser Exciter," Rev. Sci. Instrum. 51(10), 1426 (October 1980).

END

FILMED

4-85

DTIC